

THE UNIVERSITY OF MICHIGAN
INDUSTRY PROGRAM OF THE COLLEGE OF ENGINEERING

TEMPERATURE AND RATE DEPENDENT FRACTURE
BEHAVIOR OF GLASSY POLYMERS

Chul Soo Lee

A dissertation submitted in partial fulfillment
of the requirements for the degree of
Doctor of Philosophy in the
University of Michigan
Department of Mechanical Engineering
1974

April, 1974

IP-856

ABSTRACT

TEMPERATURE AND RATE DEPENDENT FRACTURE BEHAVIOR OF GLASSY POLYMERS

by

Chul Soo Lee

Co-chairmen: R.M.Caddell and A.G.Atkins

Fracture behavior of two glassy polymers, namely, Polymethylmethacrylate (PMMA) and Polycarbonate (PC), has been investigated as a function of temperature and rate of loading.

K_{IC} values were obtained using compact tension specimens of identical geometry so as to avoid any geometrical effects. The variation of K_{IC} was obtained in the temperature range of 193 °K to 353 °K using crosshead speeds ranging from 0.833 $\mu\text{m/s}$ to 8.33 mm/s.

Fracture toughness, R , was obtained graphically from load-displacement curves and information related to change in crack length was obtained by using silver paint technique. Stable crack growth of PMMA was found to be impossible at temperatures below 243 °K, whereas PC exhibited stable crack propagation at temperatures down to 213 °K.

Experimental results of PMMA fracture toughness, R , versus crack speed in the temperature range between 283 °K to 353 °K were shown to follow the Ree-Eyring type activated

flow model with the stress term replaced by fracture toughness, R . Activation energy obtained in this temperature range came close to that of the β process in PMMA associated with crazing processes. However, fracture toughness results below 283°K did not follow the predicted curves.

K_{IC} results for PMMA at each crosshead speed showed a steady increase as the temperature decreased until they reached a plateau or a maxima; this takes place at lower temperatures for slower crosshead speeds. Activation energy for such a transition also suggests involvement of a β process above these transition temperatures. Deviation of experimental PMMA fracture toughness results from the predicted curves below 283°K suggests a mechanism other than the β process is operating below this temperature.

Fracture toughness, R , of PC was influenced by the size of the 'plastic enclave' around the crack tip. Effects of crack speed were less pronounced as compared to the effect of temperature. A sharp drop in both K_{IC} and R data occurred around 273°K .

Fracture surfaces of PMMA were shown to be related to fracture toughness, crack speed and temperature, and the formation of various (microscopic and macroscopic) markings on the fracture surfaces have been explained. Formation of different textures of fracture surfaces was attributed to different rates involved in void formation and coalescence in the crazed material at the crack tip.

ACKNOWLEDGEMENTS

The author wishes to express his gratitude to Professor R. M. Caddell, Co-chairman, for his meticulous advice and financial assistance throughout the program. The author is equally indebted to Professor A. G. Atkins, Co-chairman, for introducing me to the subject of fracture and for his stimulating suggestions throughout the present study. The author feels privileged to have both Professors as Co-chairmen in the full sense of Co-chairmanship.

The author also wishes to express his thanks to Professors D. K. Felbeck, W. F. Hosford, K. C. Ludema and G. S. Y. Yeh for their valuable suggestions while serving as doctoral committee members. Particular thanks are due to Professor K. C. Ludema and Professor G. S. Y. Yeh for generating my interest into the behavior of the polymeric materials. Financial support by Professor Frederick connected with high speed photography used in crack speed measurements is also acknowledged.

Financial assistance from the following organizations in the University of Michigan is gratefully acknowledged: Department of Mechanical Engineering, Rackham School of Graduate studies, Work Study Program and Industry Program.

Author also wishes to express his thanks to Mr. Lynn Buege of the Mechanical Engineering Department for his technical help in instrumentation and for building a three channel amplifier, Messrs. C. Johnson and C. Shoehals for the

preparation of specimens and Messrs. W. Durrant and W. Koebnick for their help in parts of the experimentation.

I would like to send my deepest appreciation to my mother for her constant encouragement despite her personal sacrifices.

Finally, I thank my wife for her patience and understanding.

TABLE OF CONTENTS

	<u>Page</u>
DEDICATION	ii
ACKNOWLEDGEMENTS	iii
LIST OF FIGURES	viii
LIST OF TABLES	xiii
LIST OF SYMBOLS	xiv
CHAPTER I. INTRODUCTION	1
I.1 General	1
I.2 Literature Survey	2
I.2.1 Mechanics of Polymer Fracture	2
I.2.2 Microscopic and Molecular Aspects	5
I.2.2.1 Crazeing	5
I.2.2.2 Molecular Relaxation	8
I.2.3 Time-Temperature Dependent Fracture of Polymer	10
I.3 Scope of the Present Study	12
CHAPTER II. THEORETICAL BACKGROUND IN FRACTURE MECHANICS	14
II.1 Fracture Surface Energy	14
II.2 Fracture Toughness, R	18
II.3 Applications of Linear Elastic Fracture Mechanics	22
CHAPTER III. PRELIMINARY INVESTIGATIONS AND THE DESIGN OF THE SPECIMEN	28
III.1 Analysis of Crack Path	28
III.1.1 Linear Stress Analysis	29
III.1.2 Modified Stress Analysis	33
III.2 Experimental Measurement of Stress Distribution along the Crack Path	40
III.3 Crack Speed Analysis	47
III.3.1 Crack Speed Analysis for the Compact Tension Specimen	50

	<u>Page</u>
III.3.2 Crack Speed Analysis for Semi-infinite Cleavage Specimen with Side Grooves	59
CHAPTER IV. TIME-TEMPERATURE DEPENDENT FRACTURE TOUGHNESS OF GLASSY POLYMERS	68
IV.1 Background	68
IV.2 Experimental Procedure	70
IV.2.1 Fracture Specimen Preparation	70
IV.2.2 Temperature Control	77
IV.2.3 General Test Procedure	77
IV.2.4 K calibration	82
IV.3 Experimental Results	91
IV.3.1 PMMA	91
IV.3.1.1 K_{IC} Results	91
IV.3.1.2 Experimental Results of R	98
IV.3.2 PC	113
IV.3.2.1 K_{IC} Results	113
IV.3.2.2 R Results	117
IV.4 Discussion of Results	119
IV.4.1 PMMA: Proposed Theory on Stable Crack Growth rate in PMMA	119
IV.4.2 PC: Effect of Plastic Enclave Size	131
IV.4.3 Equivalent Strain Rate and Equivalent Young's Modulus of a Fracture Specimen	134
IV.4.3.1 Analysis of the Equivalent Strain rate involved with Fracture Testing	135
IV.4.3.2 Experimental Determination of the Equivalent Young's Modulus for a Stationary Crack and a Moving Crack	138
IV.4.3.2.1 Stationary Crack	138

	<u>Page</u>
IV.4.3.2.2 Moving Crack	141
IV.4.3.3 Comparison of Equivalent Young's Modulus for a Stationary Crack and a Moving Crack	146
CHAPTER V. FRACTURE SURFACES OF PMMA AND PC	150
V.1 PMMA	150
V.1.1 Fracture Surfaces in the Unstable Crack Propagation Region	159
V.1.2 Fracture Surfaces in the Stable Crack Propagation Region	175
V.2 PC	180
CHAPTER VI. CONCLUSIONS AND RECOMMENDATIONS FOR FUTURE STUDY	183
VI.1 Conclusions	183
VI.2 Recommendations for Future Study	186
APPENDIX I. TEMPERATURE AND STRAIN RATE DEPENDENT TENSILE PROPERTIES OF PMMA	187
APPENDIX II. DERIVATION OF THE STRAIN RATE EXPRESSION GIVEN IN EQUATION (4.11)	189
APPENDIX III. FORMATION OF CONIC MARKINGS	191
LIST OF REFERENCES	197

LIST OF FIGURES

<u>Figure</u>	<u>Title</u>	<u>Page</u>
1	Profile of a Crack Tip with its Associated Craze and Craze Layer on the Fracture Surface.	9
2	Schematic Representation of a Flat Plate with a Crack.	19
3	Graphical Representation of Gurney's Method of Measuring the Fracture Toughness, R, during the Quasi-static Crack Propagation.	21
4	Three Modes of Fracture.	24
5	Coordinate System Associated with Equation (2.17).	24
6	Nominal Stress Levels in a Cleavage Fracture Specimen (Following References 2).	30
7	Comparison of Stress in x-direction and stress in y-direction in a Specimen shown in Figure 6 (following References 2).	32
8	Stress State along the expected Crack Path.	39
9	Strain Gage Calibration Curve.	42
10	Sequential location of strain gages on the four fracture specimen.	43
11	Load, Crack Length and Stress as a function of Time. Numbers in stress-time Plot indicate Strain Gage Number in Figure 10.	44
12	Comparison of Various Analyses with Experimental Results.	46
13	Comparison of Experimental Crack Speed with the Predicted Values Based on the Present Analysis.	58
14	Calculated Crack Speed of Cleavage Specimen; $W/H \geq (a/H)+2$	63
15	Comparison of Calculated Crack Speed with the Experimental Crack Speed Reported by Broutman(1965) for PMMA.	66

<u>Figure</u>	<u>Title</u>	<u>Page</u>
16	Fracture Specimen used in the Present Experiment.	72
17	Eccentric Loadings Caused by Tapered Pin Holes.	73
18	Comparison of Normal Crack Tip Shape and Abnormal Crack Tip Shape for PMMA.	75
19	A Fracture Specimen Mounted on an Instron Machine equipped with an Environmental Chamber.	78
20	Schematic Diagram of Fracture Test Set-up.	79
21	Pictures of Experimental Set-up.	80
22	Loading Yokes, Loading Pins and Sliding Pin.	81
23	Experimental Compliance Data and the least-squares best fit Curve.	85
24	Comparison of K-Calibration Results by various Workers.	88
25	Typical Load-Displacement Curve from PMMA and PC Fracture Tests from Instron chart.	92
26	K _{IC} Results of PMMA as a Function of Temperature and Crosshead Speed.	93
27	A Typical Visicorder Record showing X, u and 'a' as function of Time.	99
28	X-u Plot Reconstructed from the Data in Figure 27. Each Sector Area Corresponds to Crack Extension of 6.35 mm.	100
29	Fracture Toughness, R, as a Function of Crack Speed, at 243°K.	101
30	Fracture Toughness, R, as a Function of Crack Speed, at 253°K.	102
31	Fracture Toughness, R, as a Function of Crack Speed, at 263°K.	103
32	Fracture Toughness, R, as a Function of Crack Speed, at 273°K.	104

<u>Figure</u>	<u>Title</u>	<u>Page</u>
33	Fracture Toughness, R, as a Function of Crack Speed, at 283°K.	105
34	Fracture Toughness, R, as a Function of Crack Speed, at 296°K.	106
35	Fracture Toughness, R, as a Function of Crack Speed, at 318°K.	107
36	Fracture Toughness, R, as a Function of Crack Speed, at 333°K.	108
37	Fracture Toughness, R, as a Function of Crack Speed, at 353°K.	109
38	Picture of the Oscilloscope Trace during Unstable Crack Propagation.	111
39	K_{IC} as a Function of Temperature and Crosshead Speed.	116
40	Load-displacement Curves of PC Fracture Tests.	118
41	Fracture Toughness, R, of PC as a Function of Crack Speed at Temperatures of 273°K, 253°K, 233°K and 213°K.	120
42	Fitting Curves for Fracture Toughness against Crack Speed at Temperatures, 283°K through 353°K.	126
43	Fracture Toughness Results against Crack Speed for Temperatures, 243°K, 253°K and 273°K.	127
44	$\log_{10} \dot{u}$ vs. $1/T$ Plot corresponding to $K_{IC}=1.5 \text{ MN/m}^{3/2}$ as shown in Figure 45.	128
45	Data Points for the Plot in Figure 44 are picked at $K_{IC}=1.5 \text{ MN/m}^{3/2}$.	129
46	Fracture Toughness of PC as a Function of Temperature.	133
47	Example of Calculating Equivalent Young's Modulus for a Stationary and a Moving Crack.	142

<u>Figure</u>	<u>Title</u>	<u>Page</u>
48	Equivalent Young's Modulus for the Stationary Crack.	143
49	Equivalent Young's Modulus for the Moving Crack.	145
50	Comparison of Equivalent Young's moduli from present experiments vs. predicted values by Williams (1972).	148
51	Fracture Surfaces of PMMA tested at the Crosshead speed of 8.33 $\mu\text{m/s}$.	151
52	Fracture Surfaces of PMMA tested at the Crosshead speed of 83.3 $\mu\text{m/s}$.	152
53	Fracture Surfaces of PMMA tested at the Crosshead speed of 833 $\mu\text{m/s}$.	153
54	Fracture Surfaces of PMMA tested at the Crosshead speed of 8.33 mm/s .	154
55	Approximate Demarcation between unstable and Stable Crack Growth as a function of Temperature, Crosshead Speed and Crack Length.	156
56	Crack Speed vs. Crack Length for various Crosshead speeds used.	157
57	Difference in microscopic features of slow stable fracture and fast unstable fracture at 273 $^{\circ}\text{K}$ and 296 $^{\circ}\text{K}$ for PMMA.	160
58	Schematic Diagram showing the Primary Crack front and the Secondary Crack Front.	161
59	Microscopic view (70X) of an Unstable Fracture Surface of PMMA at various Locations.	164
60	Variation of Conic marking density and the associated K_{IC} values for PMMA.	166
61	Fracture Surface of PMMA at 193 $^{\circ}\text{K}$.	168
62	Formation of a Wallner Line and estimated Crack Speed from the Wallner Lines.	170
63	Qualitative Explanation for a Fan-shaped Smooth Region and Rough Surface outside the Fan-shaped Region, in Figure 61a.	173

<u>Figure</u>	<u>Title</u>	<u>Page</u>
64	Rough Region in Figure 61a viewed under SEM.	174
65	Fracture Surfaces from Stable Cracking at 296 °K for PMMA.	176
66	Abrupt change in PMMA Fracture Surface associated with the sudden change in Fracture Toughness at a) 243 °K and b) 353 °K.	177
67	Fracture Surfaces of PC obtained from Stable Cracking at various temperatures.	181
68	Stable Cracking (a) and Unstable Cracking (b) of PC at 296 °K.	182

LIST OF TABLES

<u>Table</u>	<u>Title</u>	<u>Page</u>
1.	Experimental Crack Speed Data.	54
2.	Experimental Crack Speed Data from a Side Grooved Cleavage Specimen.	64
3.	K-Calibration Results for Compact Tension Specimen by Several Workers.	87
4.	Experimental Results of K_{IC} of PMMA.	94
5.	Experimental Results of K_{IC} of PC.	114
6.	Curve Fitting Equations and Constants Obtained from the Experimental Fracture Toughness Data of PMMA.	124

LIST OF SYMBOLS

A	Crack area.
A_0, A_1	Constants.
a	Crack length.
b	(W-a).
B	Thickness of a fracture specimen.
B_N	Thickness of the net cross section of a groove cleavage specimen.
C_0	Integration constant: $\frac{EB}{2} \left(\frac{u}{x} \right)_{a=0}$.
C_1, C_2	Constants.
c, \vec{c}	Scalar or vector quantity of elastic transverse wave velocity in a material.
E	Young's modulus.
e_y	Total strain corresponding to 0.3% offset yield stress.
\dot{e}	Strain rate.
G	Strain energy release rate.
H	Height of one arm in cleavage or compact tension fracture specimen.
k	Stiffness.
\bar{k}	Boltzmann's constant.
K	Stress intensity factor.
K_{IC}	Mode I plane strain crack toughness parameter.
K_m	Minimum level of K_0 for a craze to grow.
K_n	A level of K_0 below which craze growth rate decreases until it stops growing and above which craze accelerated to a final rupture.
K_0	Initial stress intensity factor before crack extends in constant load experiment.
$^{\circ}K$	Degrees Kelvin.

r	Distance measured from the crack tip.
n	Ratio of secondary crack speed v , to primary crack speed, V .
p_x	non-dimensional stress in x-direction $\frac{\sigma_x}{(X/BW)}$.
p_y	Non-dimensional stress in y-direction.
R	Fracture toughness.
\bar{R}	Average fracture toughness value in the crack speed range considered.
ΔS	Change in surface energy.
t_f	Time measured from load application to fracture.
T	Temperature $^{\circ}K$.
ΔU	Change in strain energy.
\bar{U}	Activation energy, kcal/mol $^{\circ}K$.
u	Deflection of a cleavage specimen, or the displacement of loading pins during a fracture test.
u_c	Critical loading pin displacement at which crack starts to extend.
\dot{u}	Crosshead speed.
V, \vec{V}	Scalar or vector quantity of primary crack speed.
ΔW	Net change in the energy of the system.
W	Width of a fracture specimen.
X	Load.
x_o	Distance between the primary crack front and secondary crack nucleus.
γ	Fracture surface energy.
γ_g	Theoretical surface energy.
γ_p	Component of fracture surface energy accounting for the energy dissipation due to plastic flow at the crack tip.

ν	Poissons ratio.
λ	Constant.
ϕ	Constant.
σ_f	Stress at fracture.
σ_x	Stress in x-direction.
σ_y	Stress in y-direction.
τ_{xy}	Shear stress in the plane of the plate around crack tip.
v	Secondary crack speed.

CHAPTER I

INTRODUCTION

I.1 General

As a greater number of polymers are being introduced in engineering design applications, their complex mechanical behavior presents certain problems to the design engineer. One of these important aspects, which needs further understanding, is their fracture behavior. A knowledge of a material's resistance against crack growth and its capacity to absorb the energy of the running crack is vital to an engineer if he is to design against this catastrophic mode of failure.

Since the introduction of the brittle strength theory of elastic solids by Griffith (1921, 1924), the incremental energy balance between the stored elastic energy around flaws and the energy needed to create new surface has, with some modifications, been a major criterion for the fracture of many materials (Orowan 1950, Irwin 1957). But polymers are not classical elastic bodies and they have a pronounced time-temperature dependent behavior in regard to their mechanical properties, which include fracture behavior. As a consequence, the Griffith theory has a very limited range of application in the polymer fracture area.

Glassy polymers are well suited for studying the fracture process in polymers because of their wide range of

fracture toughness. Their toughness varies significantly, not only from one material to another, but also from one service condition to another, i.e., temperature and the rate of loading.

Until recently, the dependency of fracture toughness of the glassy polymers on time and temperature has been discussed rarely. In many of the previous studies, fracture toughness, or surface energy was considered as a constant material property. Some workers introduced only one of the two variables, leaving the other (i.e., time or temperature) free of control. This caused large discrepancies among the published fracture toughness data for given polymers. This apparent scatter can be attributed partly to different test conditions which were not fully controlled by the authors.

Due to the scarcity of experimental data, the contribution of the two variables, i.e., time and temperature, in the fracture process of glassy polymers is yet to be established.

The purpose of the present study is to explore the variation of fracture toughness of glassy polymers at different temperatures and loading rates and to analyze the results so as to understand the mechanism of the time-temperature dependent fracture behavior of glassy polymers.

I.2 Literature Survey

I.2.1 Mechanics of Polymer Fracture

Since Griffith (1921, 1924) introduced the surface

energy of a material as an important parameter in determining the fracture strength of solids, measurements of surface energy have been pursued extensively for many materials. When it was realized that surface energy alone could not account for the large dissipation of energy during the fracture process, the term 'fracture surface energy' was introduced. In this more general form, it was meant to represent all of the energy dissipated in creating a unit area of fracture surface (Orowan 1950).

Measurements of fracture surface energy for polymers were first attempted by Berry (1961). He made a series of tensile tests of polymethylmethacrylate (PMMA) with artificial flaws. By introducing artificial flaws of different sizes, he found that the stress at fracture for these polymers was dependent on the size of the flaws in a similar fashion as Griffith had observed in his original experiment with inorganic glass; this stress was inversely proportional to the square root of the flaw size. Unfortunately this relationship ceased to hold when the flaw size was reduced down to the level where most practical flaw sizes lie.

Cleavage specimens have also been used to measure the fracture surface energy. Initially, this method involved a long rectangular beam with a crack running along the horizontal median plane starting from one side where the splitting force is being applied. In order to keep the crack path straight along the median plane, compressive stress was superimposed along the length direction of the

beam (Benbow and Roesler 1957, Svensson 1961, Benbow 1961). Later modifications of cleavage techniques involved side grooving of the specimen along the intended crack path (Berry 1963, Broutman and McGarry 1965), and/or using a tapered specimen (Ripling et al 1967).

The elastic stress field around a crack tip has been analyzed by Westergaard (1939) and the stress field can essentially be described in terms of one parameter, K . Irwin (1957) modified this solution and introduced the rather simple fracture criterion that whenever the stress environment expressed in terms of K reaches the critical value, K_c for the material, fracture will occur. He proposed that the "critical stress intensity factor", K_c be used as the parameter which describes a material's resistance against crack propagation in metals. He also introduced the term "elastic energy release rate" G and critical energy release rate G_c ; these can be converted into K or K_c by a simple functional relationship. This concept has been further developed and forms the basis for linear elastic fracture mechanics. Linear elastic fracture mechanics was first applied in the polymer fracture area by van den Boogart and Turner (1963), since then it has been applied by others (Key et al 1968, Radon 1971, Marshall and Williams 1973).

Gurney and Hunt (1967) made an independent study of quasi-static fracture. He used the term "fracture toughness" which represents the irreversible work and delayed reversible work per unit area of crack surface as referred to one side

of the crack surface during the crack propagation. "Fracture Toughness", R , can be measured graphically from the load-displacement curves obtained during a fracture test.

Various parameters representing toughness are related as; $R=G_c=2\gamma$ and $K= \sqrt{EG}$ (plane stress), $K= \sqrt{\frac{EG}{1-\nu^2}}$ (plane strain), where E is Young's modulus. Two parameters will be used in this thesis to express the two types of toughness. One is the critical stress intensity factor K_{IC} , to be used as a measure of resistance of material against initial crack extension and the other is the fracture toughness, R , to be used as a measure of resistance of a material against the running crack. The term "fracture toughness", R , will be used in this thesis following the definition of Gurney and Hunt (1967).

I.2.2 Microscopic and Molecular Aspects

I.2.2.1 Crazeing

A unique feature of glassy polymers is the appearance of "crazes" ("silver cracks" by Soviet workers) which may be considered as widely distributed tiny crack-like defects on the surface of a specimen under tensile stress. They look like a group of cracks because of the bright reflections from these spots in the otherwise transparent specimen. However, they are actually not true cracks but localized regions of the plastically deformed material interspersed with voids of varying proportions (Kambour 1972). This characteristic phenomenon was first observed in polystyrene (PS) by Sauer et al (1949) and the structure of craze was revealed by

Kuvshinskii and Lebedev (1962) and Supurr and Niegisch (1962) with light microscopy studies. The microstructure of crazes has been successfully viewed through the transmission electron microscope by Kambour and Holik (1969a and b) and Kambour (1971). They observed that the microstructure of a craze in Polyphenyleneoxide (PPO) resembled that of sponge and when stressed it appeared as a set of oriented microfibrils elongated in the maximum tensile stress direction. The fibril diameter was estimated roughly at 200 Å, irrespective of the stress state. Beahan et al (1971) have studied the microstructure of crazes in both microtomed and bulk samples of PS. The fibrillar morphology was found in both cases, with the diameter of fibrils 200 Å to 400 Å.

The explanations for the mechanics of craze initiation has been studied by several workers. Since Maxwell and Rahm (1949) suggested a critical strain criterion, Sternstein and Ongchin (1969) emphasized the role of the dilatational component of the stress state to account for the formation of voids involved with a craze. Gent (1970) explained the formation of crazes in glassy polymers in two stages: A local transformation from a glassy to rubbery phase induced by the dilatational stress followed by cavitation of the rubbery phase under the same dilatational component of stress. The current thinking tends to favor the role of "triaxial tension" in opening the "holes" in the matrix of the glassy materials (Kambour 1970).

Most of the studies on the kinetics of craze growth

have been done within very limited ranges of sizes and the proposed expressions for craze growth rate derived from the observations of the growth of crazes on the microscopic scale (Sauer and Hsiao 1953, Regel 1956, Higuchi 1966, Sato 1966). Since the crazes that were studied ceased to grow within the microscopic range, their results do not help in understanding the role of craze growth in the gross fracture process of glassy polymers. Marshall, Culver and Williams (1970) made a meaningful study of craze growth kinetics in terms of a fracture mechanics approach. Single edge notched fracture specimens of PMMA were immersed in methanol. As a tensile load was applied to the specimen a single craze started from the sharp edge notch. The growth rate of the craze was recorded as a constant load was applied to the specimen. For convenience, they used the initial stress intensity factor, K_0 as the loading parameter in their study and found three different types of craze growth depending on the magnitude of K_0 . First, the craze did not grow at all when K_0 was less than a minimum value, K_m . Second, when K_0 was bigger than K_m and yet smaller than the upper limit value K_n , their growth occurred at a decelerating rate to a final size of 0.254 to 2.54 mm. Third, when K_0 was bigger than the upper limit value K_n , craze growth rate decreased but reached a constant speed until final rupture. This study was a direct assertion that the crack growth in glassy polymers is merely an extension of a single craze growth under favorable conditions.

The involvement of craze in the fracture process of glassy polymers can be visualized from the observation of a profile of crack tip presented by Kambour (1966) as shown in Figure 1. Extensive reviews on the role of crazing in the fracture process of glassy polymers have been done by Kambour (1972) and Rabinowitz and Beardmore (1972).

I.2.2.2 Molecular Relaxation

Most of the fracture energy is dissipated during the formation of crazes and the subsequent viscous flow of molecules within the crazes (Berry 1961). The interference colour from the fracture surface of PMMA was explained by Berry (1961) to be a thin layer of oriented molecules caused by the microscopic flow at the crack tip. This microscopic "cold flow", occurring below the glass transition temperature (T_g), has been explained in terms of the secondary relaxations which provide the necessary mobility for cold flow (Boyer 1968). Boyer reviewed the role of secondary relaxation processes in crazing and on the impact strength of various polymers. He found some evidence of close association between crazing and the secondary relaxation process in PMMA and PS. But he cautioned against the generalization that the secondary relaxation peak is either a necessary or sufficient condition for high toughness. Boyer (1968) examined some of the unpublished data on rate of crack growth as function of temperature for PMMA and found that the activation energy obtained from the crack growth data was

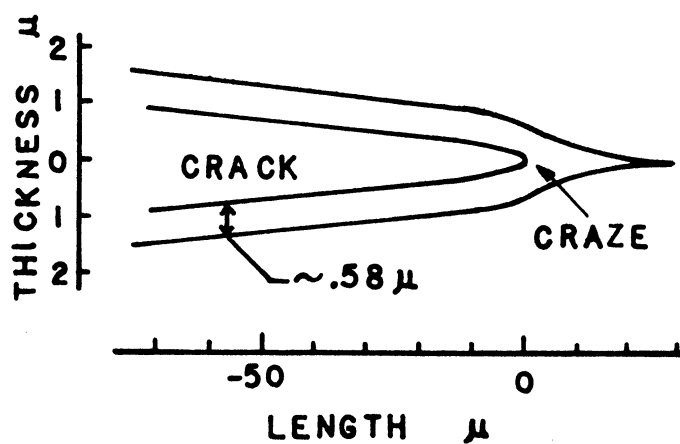


Figure 1. Profile of a crack tip with its associated craze and craze layer on the fracture surface (Kambour 1972)

very close to the value for β process, the secondary relaxation process. Broutman and Kobayashi (1971) obtained similar results from their fracture toughness data of PMMA and PS. Heijboer (1968) investigated whether the impact strength and damping properties are related, using eight polymers having different damping behaviors. Based on his experimental results he concluded that the secondary dynamic mechanical damping peaks have no major effect on the impact strength of these polymers. Rather, he attributed any major change in impact strength to the movement within the main chain. However, Johnson and Radon (1972) claimed that the toughness of PMMA expressed in terms of K_{IC} , showed peak values at the temperatures at which the secondary relaxation peaks (β and γ) of respective materials occur at the frequency equivalent to that of loading rate used in the fracture test. Thus, even though the involvement of the secondary molecular relaxation mechanism in the fracture process of glassy polymers is generally accepted on a qualitative basis, the explanation as to how it affects the fracture behavior is still at controversial stage.

I.2.3 Time-Temperature dependent fracture of polymers

Temperature dependence of fracture surface energy of glassy polymers was first reported by Berry (1963a) from his tensile tests with PMMA. He found a fivefold increase in the fracture surface energy of PMMA as the temperature was reduced from room temperature to 73 °K. Other studies using

PMMA and the cleavage technique (Svensson 1961, Benbow 1961, Broutman and McGarry 1965) showed similar trends, however there is considerable scatter among the data because different loading rates were used.

Key et al (1968) applied the fracture mechanics approach and reported the temperature dependence of the toughness of PC and PMMA, in terms of the plane strain crack toughness parameter K . Similar experiments were performed on Polyvinylchloride (PVC) by Radon (1972).

The time dependence of the fracture toughness of glassy polymers has been studied independently by several workers. Due to the complex situation in the strain history, several approximate methods were attempted to analyze the strain rates of material elements surrounding a crack (Irwin 1963, Williams 1972). Most studies have used the crack speed as a unique parameter (independent of specimen geometry and size) to represent the strain rate of the material elements surrounding a moving crack (Williams et al 1968, Cotterell 1968, Marshall and Williams 1973, Vincent and Gotham 1966). Most of the crack speed dependent behavior of fracture toughness has been performed at room temperature. Few systematic studies using both variables of temperature and crack speed are available, yet. Conventional methods of obtaining the toughness of a material in terms of the strain energy release rate, G , involve some difficulties in studying the fracture behavior of a rate dependent material because the modulus is a variable. This causes the compliance calibration at one

rate to be different from one at another rate. Gurney and Hunt (1967) introduced a method of measuring fracture toughness directly from the load-displacement curve of a stable crack propagation. This method was successfully used in the present study in obtaining temperature and crack speed dependent fracture toughness data.

I.3 Scope of the present study

Present study aims at investigating the variation of toughness of polymers as function of both temperature and loading rates.

Materials used in the present study were polymethylmethacrylate (to be abbreviated as PMMA hereafter) and polycarbonate (to be abbreviated as PC hereafter). These two glassy polymers were chosen on the ground that the former (PMMA) represents a brittle polymer and the latter (PC) represents a tough polymer.

Both factors, K , and Gurney's fracture toughness parameter, R , will be used to represent toughness. Because the fracture toughness parameter, R , is measured from the stable crack propagation, techniques will be developed to achieve stable crack propagations along the straight crack path.

When the temperature and rate dependent toughness, both in terms of K_{IC} and R , are obtained, they will be analyzed for an empirical relationship between toughness, temperature and loading rate.

Finally, fracture surfaces will be studied to characterize various features in terms of temperature and crack speed.

CHAPTER II

THEORETICAL BACKGROUND OF FRACTURE MECHANICS

II.1 Fracture surface energy

Solid materials usually fracture at a stress level which is substantially lower than the theoretical strength calculated from their molecular constitution and structure. The discrepancy between the theoretical and observed fracture strength of glass was attributed by Griffith (1921, 1924) to the presence of flaws. The problem, as he stated it, involved a two dimensional infinite plane containing a through-thickness line crack of length $2a$, loaded under uniform tensile stress, σ , at the infinite boundary. The stress field equations had been solved by Inglis (1913) for elliptical shaped flaws. Griffith considered the line crack as the degenerate case of an elliptical cavity and applied the Inglis solution to calculate the change in the strain energy of the system due to the presence of the crack. The change in strain energy ΔU , was expressed in terms of crack length, 'a', as;

$$\Delta U = - \frac{\pi a^2 \sigma^2}{E} \begin{cases} (1 - \nu^2) & \text{plane strain} \\ 1 & \text{plane stress} \end{cases} \quad (2.1)$$

where E is Young's modulus and ν is Poisson's ratio. The contribution of the crack formation to the surface energy of the system ΔS is;

$$\Delta S = 4\gamma_g a \quad (2.2)$$

where γ_g is the surface energy of the material. The net change in energy of the system, ΔW is;

$$\begin{aligned} \Delta W &= \Delta S + \Delta U \\ &= 4\gamma_g a - \frac{\pi a^2 \sigma^2}{E} \begin{cases} (1 - \nu^2) & \text{plane strain} \\ 1 & \text{plane stress} \end{cases} \quad (2.3) \end{aligned}$$

The system becomes unstable and the crack will increase in size if the incremental change in energy is equal to or less than zero at increasing crack length.

$$\frac{\partial(\Delta W)}{\partial a} \leq 0 \quad (2.4)$$

From equations (2.3) and (2.4),

$$\sigma = \sigma_f = \begin{cases} \sqrt{\frac{2E\gamma_g}{(1-\nu^2)\pi a}} & \text{plane strain} \\ \sqrt{\frac{2E\gamma_g}{\pi a}} & \text{plane stress} \end{cases} \quad (2.5)$$

where σ_f is the stress at fracture. This relationship was shown to be in good agreement with the experiments on glass

by Griffith.

When the surface energy of other materials were estimated from this theory, they were substantially higher than the theoretical surface energies (Orowan 1950). These large discrepancies were attributed mainly to additional energy dissipated during plastic flow at the crack tip. Orowan (1950) justified the application of the Griffith theory to general fracture, so long as the plastic flow is localized at the crack tip, thus the dissipated energy is still proportional to the fracture surface produced. The modified Griffith criterion becomes,

$$\sigma_f = \begin{cases} \sqrt{\frac{2E(\gamma_g + \gamma_p)}{\pi(1-\nu^2)a}} & \text{plane strain} \\ \sqrt{\frac{2E(\gamma_g + \gamma_p)}{\pi a}} & \text{plane stress} \end{cases} \quad (2.6)$$

where γ_g represents the theoretical surface energy and γ_p is the energy dissipation due to plastic deformation at the crack tip. The sum of the two quantities γ_g and γ_p is called the fracture energy, γ , and it is used to represent all the energy dissipated during the formation of a unit area of crack surface.

The Griffith fracture criterion has been applied to the fracture of polymers, and the fracture surface energy has been measured using a variety of specimen shapes. A common technique involves the use of cleavage specimen of

either parallel or tapered shape. First, the relationship between crack length, a , deflection, u , and load, X , is established either from simple beam equation or from empirical relationships from experiment. Then,

$$X = f(u, a) \quad (2.7)$$

and the strain energy within the system is,

$$\Delta U = \frac{1}{2} X \cdot u = \frac{1}{2} f(u, a) \cdot u \quad (2.8)$$

The surface energy in the system is,

$$\Delta S = 2\gamma \cdot a \cdot B \quad (2.9)$$

where B is the thickness of the cleavage specimen.

The total energy, ΔW , within the system is,

$$\Delta W = \Delta S + \Delta U = 2\gamma \cdot a \cdot B + \frac{1}{2} f(u, a) \cdot u \quad (2.10)$$

Applying the Griffith criterion for fracture,

$$\left. \frac{\partial(\Delta W)}{\partial a} \right|_u = 2\gamma B + \frac{1}{2} \cdot u \cdot \left. \frac{\partial f}{\partial a} \right|_u \stackrel{?}{<} 0 \quad (2.11)$$

From this,

$$\gamma = -\frac{u}{4B} \left(\frac{\partial f}{\partial a} \right)_u \quad (2.12)$$

The important feature in the above analysis is that

the fracture surface energy is measured at constant deflection (i.e. $u=\text{constant}$). In practice, this means that a sufficiently large deflection is imposed upon the system before the crack starts, then deflection is maintained constant until the propagation comes to a halt at the equilibrium crack length for the given deflection. This practice is very time consuming and needs delicate testing procedures.

In some cases the fracture surface energy of cleavage specimens has been erroneously measured due to the misunderstanding of the assumptions in the analysis leading to equation (2.12). For example, Broutman and McGarry (1965) measured the fracture surface energy of PMMA and PS with cleavage specimens. They measured the force, deflection and crack length while the crosshead moved at constant speed. These data were erroneously fed into the Griffith criterion, which, as stated, applied for the fixed deflection case only. As a consequence, their results come out significantly lower than the values found in this present work. Broutman later acknowledged his mistake (1973) and the corrected value came close to the data in this dissertation. The difficulty involved with fixed deflection cleavage test can be avoided with a more generalized cracking theory due to Gurney and Hunt (1967). This will be discussed in the next section.

II.2 Fracture Toughness, R.

Gurney and Hunt (1967) made a general analysis of quasi-static crack propagation where he assumed that the energy in the

system maintains equilibrium throughout the process.

Consider a general case of crack propagation shown in Figure 2.

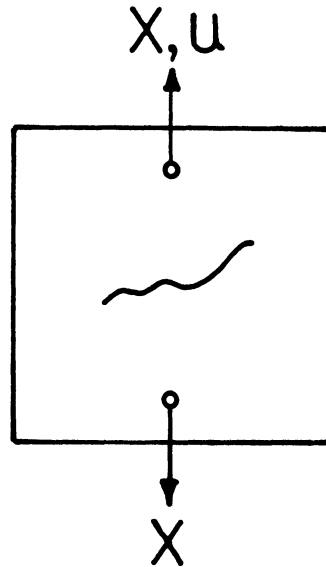


Figure 2. Schematic representation of a flat plate with a crack

For an increment of displacement du , let the corresponding increment of crack surface area be dA during the equilibrium crack propagation. For static equilibrium of the system, the work done by all the forces, internal and external, during a quasi-static displacement should be zero,

$$Xdu - d(\text{strain energy}) - RdA = 0 \quad (2.13)$$

For a linear elastic system,

$$Xdu = RdA + \frac{1}{2}d(u \cdot X) \quad (2.14)$$

The Xdu term represents the external work input by the dis-

placement of the loading pin, $1/2d(u \cdot X)$ represents the change in the elastic strain energy stored in the system and finally, RdA represents the irreversible and delayed reversible work in forming the fracture surface area dA . dA refers to only one side of the cleaved surface instead of two sides usually adopted by previous workers in measuring fracture surface energy. R will be called "fracture toughness" in this study.

Equation (2.14) can be represented graphically as shown in Figure 3. The sector area OAB represents the energy dissipated during the crack propagation ΔA . With the knowledge of this sector area, $R\Delta A$, and the corresponding increment of fracture area, ΔA , R can be calculated by,

$$R \cdot (\Delta A) = OAB$$
$$R = \frac{OAB}{\Delta A} \quad (2.15)$$

This method provides a very convenient means of measuring the fracture toughness, R , of any material for a wide range of specimen geometry as long as stable crack propagation can be achieved. For a highly rate dependent material, like glassy polymers the fracture toughness value, R , may vary during a single test because the crack speed changes as the crack length increases. This difficulty can be accommodated with Gurney's method because the R value can be measured directly from the load displacement curve, and the crack length and crack speed can be monitored either visually or by a simple instrumentation.

FROM EQUATION (2.14)

$$\begin{aligned}
 R_{AA} &= X \Delta u - \frac{1}{2} \Delta(uX) \\
 &= ABCD - (OBC - OAD) \\
 &= ABCD - (BCDP - APO) \\
 &= (ABCD - BCDP) + APO \\
 &= ABP + APO \\
 &= OAB
 \end{aligned}$$

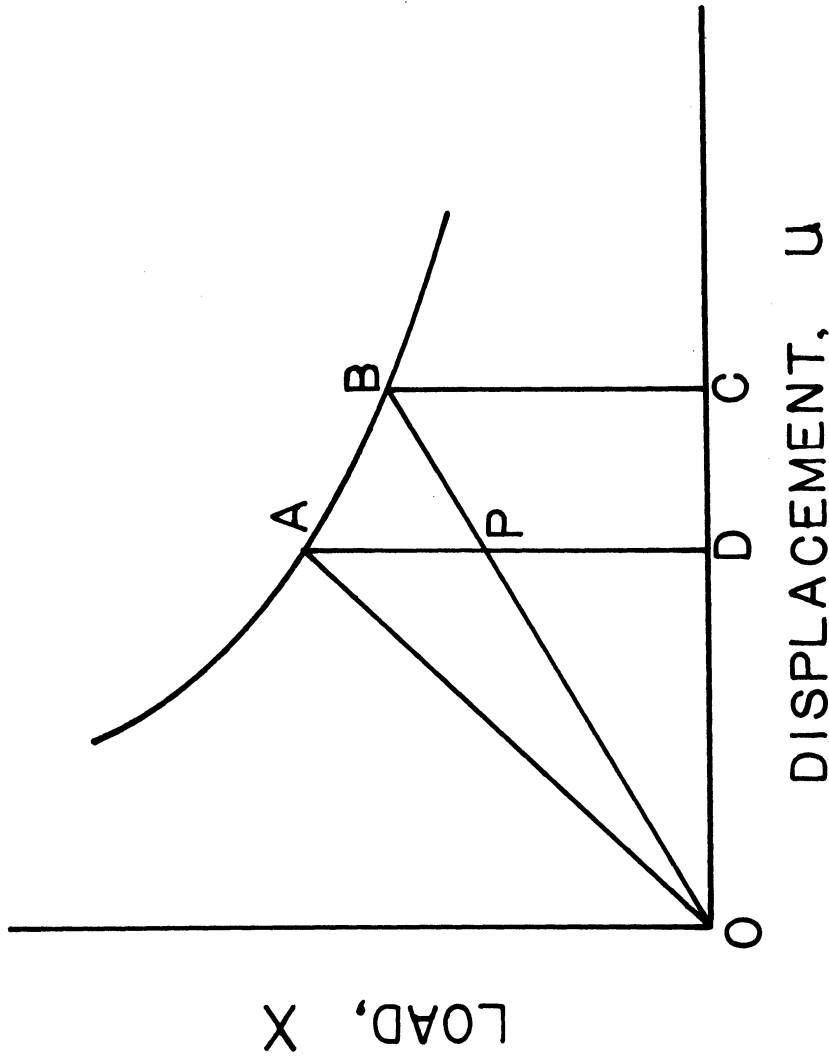


Figure 3 Graphical representation of Gurney's method of measuring the Fracture Toughness, R, during the quasi-static crack propagation.

Equation (2.14) can be written in other forms;

$$\begin{aligned}
 Xdu &= RdA + \frac{1}{2}d(uX) = RdA + \frac{1}{2}Xdu + \frac{1}{2}udX \\
 RdA &= \frac{1}{2}(Xdu - udX) = \frac{1}{2}X^2d(u/X) \\
 R &= \frac{1}{2}X^2 \frac{d(u/X)}{dA}
 \end{aligned}
 \tag{2.16}$$

Equation (2.16) has the same form as that for the strain energy release rate G_c , introduced by Irwin (1957). This equation (2.16) suggests that the fracture toughness, R , can also be measured from a knowledge of the compliance data and the load at the start of crack propagation. In fact, this method applies for case when equilibrium crack propagation cannot be attained (i.e. unstable cracking). Compliance, (u/X) , vs. crack area (A) data are first established experimentally with the specimen containing the known crack area (crack length times thickness). Differentiating these data with respect to crack area gives $d(u/X)/dA$ for a specimen of given starting crack area. R can be calculated by introducing the load at fracture X_c and $d(u/X)/dA$ of the specimen tested.

II.3 Applications of linear elastic fracture mechanics

Cracks of brittle fracture in solids can be classified into three independent modes of kinematic movements of upper and lower crack surface with respect to each other. These three modes of I) opening, II) sliding and III) tearing are shown schematically in Figure 4. They are conven-

tionally called modes I, II and III, respectively (Irwin 1958). Only mode I will be discussed in this chapter for brevity, since similar analyses hold for the remaining modes and the mode of fracture in this dissertation is the mode I unless stated otherwise.

Irwin (1957) modified Westergaard's solution (1939) of stress functions for the local stress distribution around a crack tip. For the region of a tensile crack shown in Figure 5, the stress distributions around the crack tip can be expressed as;

$$\sigma_x = \frac{K}{\sqrt{2\pi r}} \cos(\theta/2) \{1 + \sin(\theta/2) \sin(3\theta/2)\}$$

$$\sigma_y = \frac{K}{\sqrt{2\pi r}} \cos(\theta/2) \{1 - \sin(\theta/2) \sin(3\theta/2)\}$$

$$\tau_{xy} = \frac{K}{\sqrt{2\pi r}} \sin(\theta/2) \cos(\theta/2) \cos(3\theta/2)$$

$$\sigma_z = \begin{cases} \nu(\sigma_y + \sigma_x) & \text{plane strain} \\ 0 & \text{plane stress} \end{cases} \quad (2.17)$$

where the coordinates are as shown in Figure 5. K is called the stress intensity factor which provides a single-parameter characterization of the stress state around the crack tip. K is subscripted as K_I , K_{II} and K_{III} depending on the mode of crack surface displacement as shown in Figure 4. The stress intensity factor, K, is related with the strain energy release rate, G, which in turn has the same value as the frac-

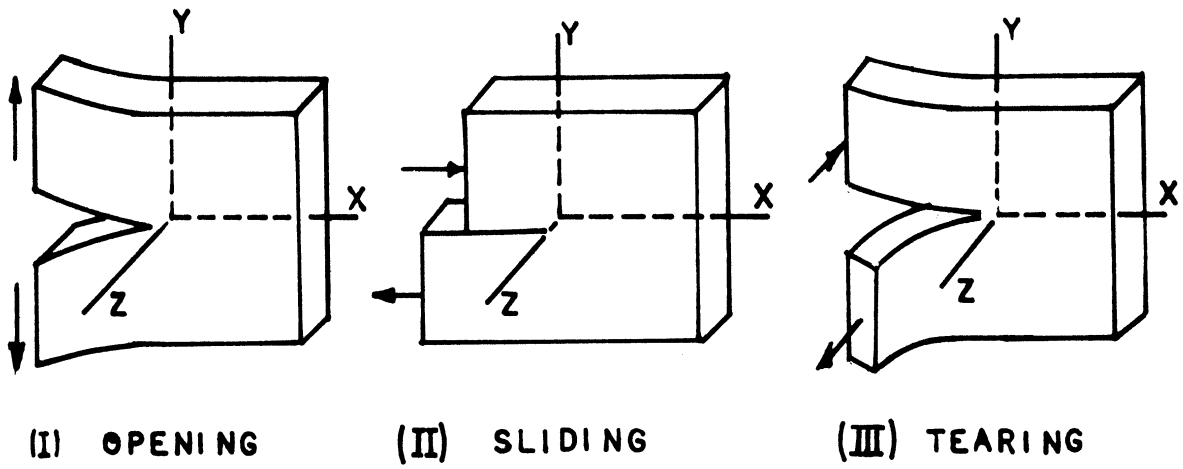


Figure 4. Three modes of fracture

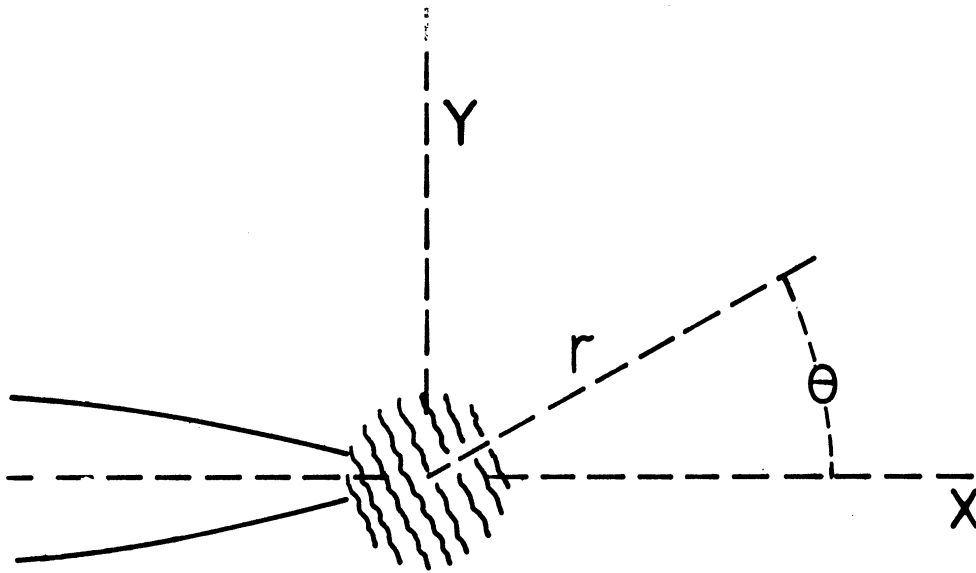


Figure 5. Coordinate system associated with equation(2.17)

ture toughness, R, by a simple relationship,

$$\begin{aligned} G = R &= (K^2/E)(1-\nu^2) && \text{plane strain} \\ G = R &= (K^2/E) && \text{plane stress} \quad (2.18) \end{aligned}$$

where E is Young's modulus. It is a common practice to use the expression $R=K^2/E$ for both plane strain and plane stress cases because the difference between the two cases is not significant (Brown and Srawley 1966). This practice will be followed in the present study unless stated otherwise.

K is determined from the specimen geometry and the applied load. The analytical approach to determine K as a function of geometry and load involves a complex mathematical operation even for a simple geometry. Paris and Sih (1965) provide a summary of the results on the analysis of the stress intensity factor K, for various type of specimen and loading modes. An alternative way to avoid these mathematical complexities is to determine K experimentally through compliance measurement method which will be described next.

The expression for strain energy release rate, G, has the same form as one for fracture toughness, R, shown in equation (2.16),

$$\begin{aligned} G = R &= \frac{1}{2} X^2 \frac{d(u/X)}{dA} \\ \text{or} \quad G = R &= \frac{1}{2} X^2 \frac{d(u/X)}{Bda} \end{aligned}$$

where B is thickness of the specimen. Since K and G are related by equation (2.18), it follows from equation (2.18) and equation (2.16),

$$K^2 = \frac{EB}{2} \frac{X^2}{WB^2} \frac{d(u/X)}{d(a/W)} \quad (2.19a)$$

or commonly expressed in non-dimensional form as;

$$\frac{K^2 B^2 W}{X^2} = \frac{EB}{2} \frac{d(u/X)}{d(a/W)} \quad (2.19b)$$

where W is the width, B is thickness of the specimen and u is the displacement of loading pin. Equation (2.19b) suggests that K can be determined experimentally by measuring the rate of change of compliance as a function of crack length for the given specimen geometry. In practice, the prototype specimens are made with different crack lengths. The compliance, (u/X), of each specimen is measured experimentally by taking the reciprocal of its stiffness, (X/u). These compliance data are plotted as a function of a non-dimensionalized crack length, (a/W). This set of results is then fitted to a polynomial in (a/W) by a standard statistical method of "best fit". The fitting function for compliance, (u/X), is differentiated with respect to (a/W) to obtain $\frac{d(u/X)}{d(a/W)}$ in terms of polynomials in (a/W);

$$\frac{d(u/X)}{d(a/W)} = f(a/W) \quad (2.20)$$

Applying this result in equation (2.19b) we get,

$$\begin{aligned} \frac{K^2 B^2 W}{X^2} &= \frac{EB}{2} f(a/W) \\ &= \frac{EB}{2} \sum_0^n A_i (a/W)^i \end{aligned} \quad (2.21)$$

where $A_i (a/W)^i$ represents a polynomial in (a/W) . Good agreement between the experimental and analytical results were reported by Brown and Srawley (1966).

Care must be taken in the experimental K-calibration of a strain rate sensitive material, because the modulus value to be used in equation (2.19) varies for different rates of loading. This will be discussed further in chapter IV.

CHAPTER III

PRELIMINARY INVESTIGATIONS AND THE DESIGN OF THE SPECIMEN

In designing a fracture specimen for the present study, the most important factors to be considered are the predictions of crack path and the crack speed for the given specimen geometry under a given crosshead speed. Derivation of crack speeds will be given in the next section and the analysis for crack paths will be given in this section. Both analyses are done for the cleavage specimen which is used throughout this study.

III.1 Analysis of crack path

Control of the crack path in a straight line can be made possible by various methods. Benbow (1957, 1961) and Svensson (1961) applied a compressive stress along the length direction of their cleavage specimen to suppress the tensile bending stress which causes the crack path to deviate from a straight line. Berry (1963b), Broutman and McGarry (1965) and Ripling et al (1967) introduced side grooves along the desired crack path to increase the tensile stress within the grooved area so that a crack would follow this preferential path. These modifications of loading mode or specimen geometry cause some uncertainty in the experimental results. Their effect on fracture toughness is not yet understood. For example, the complex triaxial stress state at the root

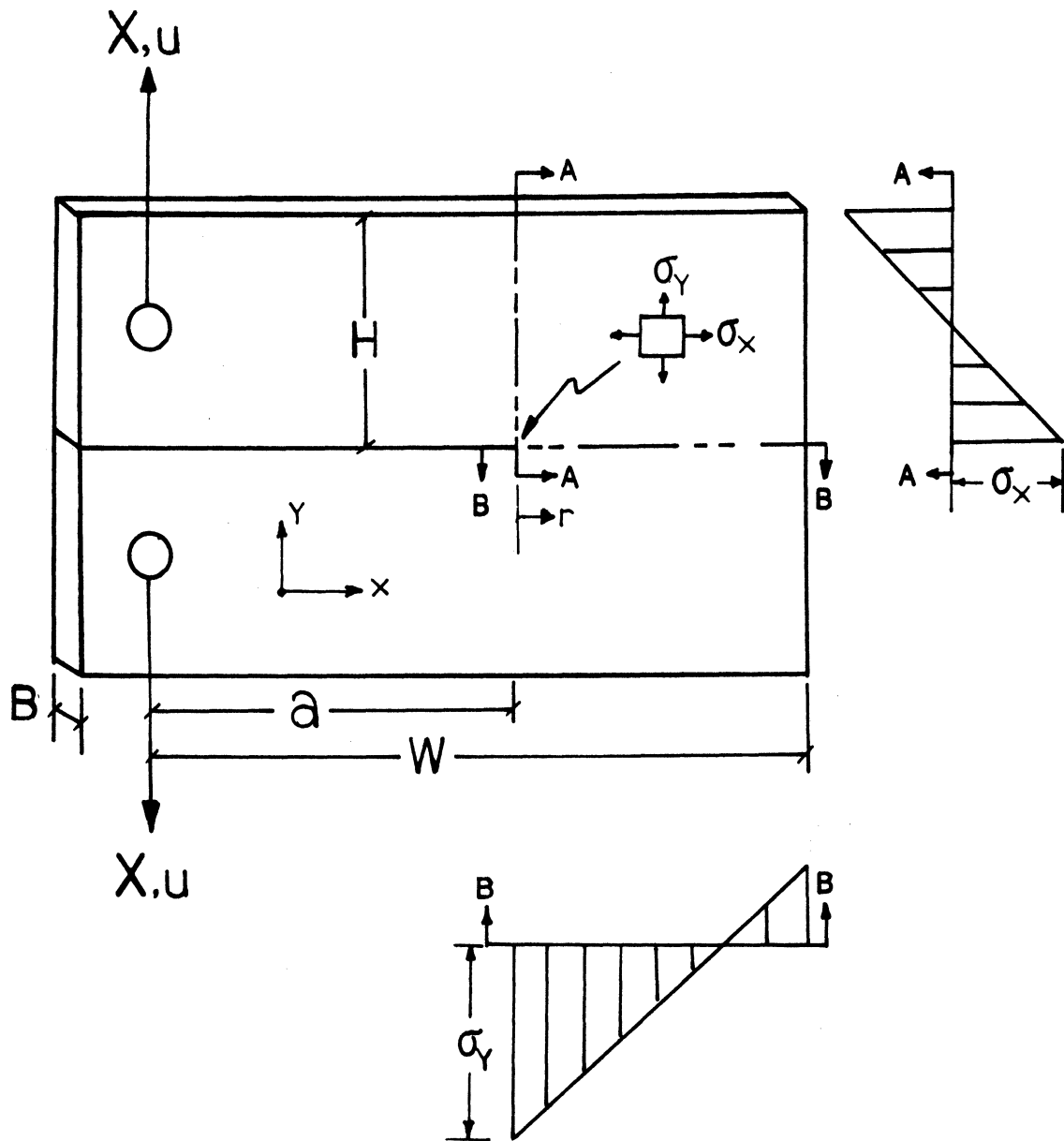
of the grooved region for the side grooved specimen remains a "formidable" problem to be analyzed (Irwin 1965). Broutman and Kobayashi (1971) reported that the residual stress induced during machining the side grooves can cause the toughness value of PMMA to be substantially higher than the value measured in the "annealed" state. With this in mind, the present study utilizes the cleavage specimen without side grooves.

III.1.1 Linear stress analysis

A linear analysis of the nominal stress distribution of a cleavage specimen has been reported by Manjoine (1965). Cotterell (1970) reported a higher probability of the crack to run straight when the nominal stress normal to the crack surface is higher than the stress parallel to the existing crack line. Atkins and Caddell (1973) made a similar analysis and extended this further to provide a comprehensive guide for the design of fracture specimen that leads to straight crack paths. Their analysis is followed in this section.

Consider a cleavage specimen of length, W , height, $2H$, thickness, B , and crack length, a , being loaded with splitting force, X , as shown in Figure 6. The nominal stress at the crack tip can be calculated by assuming that the bending stress is linearly distributed across the section A-A and B-B;

$$\sigma_x \Big|_{r=0} = \frac{(X \cdot a)(H/2)}{I_{A-A}} = \frac{(X \cdot a)(H/2)}{(BH^3/12)} = \frac{6X \cdot a}{BH^2} \quad (3.1)$$



$$\sigma_x \Big|_{r=0} = \frac{(X \cdot a)(H/2)}{I_{A-A}}$$

$$\sigma_y \Big|_{r=0} = \frac{\left(x \cdot \frac{W+a}{2}\right) \left(\frac{W-a}{2}\right)}{I_{B-B}} + \frac{x}{B(W-a)}$$

Figure 6. Nominal stress levels in a cleavage fracture specimen (following Reference 2).

$$\begin{aligned}\sigma_y \Big|_{r=0} &= \frac{\{X \cdot (W+a)/2\} \cdot (W-a)/2}{I_{B-B}} + \frac{X}{B(W-a)} \\ &= \frac{3X(W+a)}{B(W-a)^2} + \frac{X}{B(W-a)}\end{aligned}\quad (3.2)$$

These can be expressed in non-dimensional form as;

$$p_x = \frac{\sigma_x}{(X/BW)} = 6(a/W)(W/H)^2 \quad (3.1a)$$

$$\begin{aligned}p_y &= \frac{\sigma_y}{(X/BW)} = \frac{1}{(1-a/W)} + \frac{3(1+a/W)}{(1-a/W)^2} \\ &= \frac{(1-a/W) + 3(1+a/W)}{(1-a/W)^2}\end{aligned}\quad (3.1b)$$

These non-dimensional stress, $p_x = \frac{\sigma_x}{(X/BW)}$ and $p_y = \frac{\sigma_y}{(X/BW)}$ are plotted against non-dimensional crack length, a/W , in Figure 7. Straight lines represent the non-dimensional stress, p_x , for different values of W/H and the single curve represents the non-dimensional stress, p_y . The crack will run straight along the center line as long as $p_y > p_x$ but it will turn away from the straight path when $p_y \leq p_x$. A specimen geometry of $W/H = 1.67$ was chosen for the present study, for which p_y is greater than p_x for any crack length (a/W), and straight crack path is predicted.

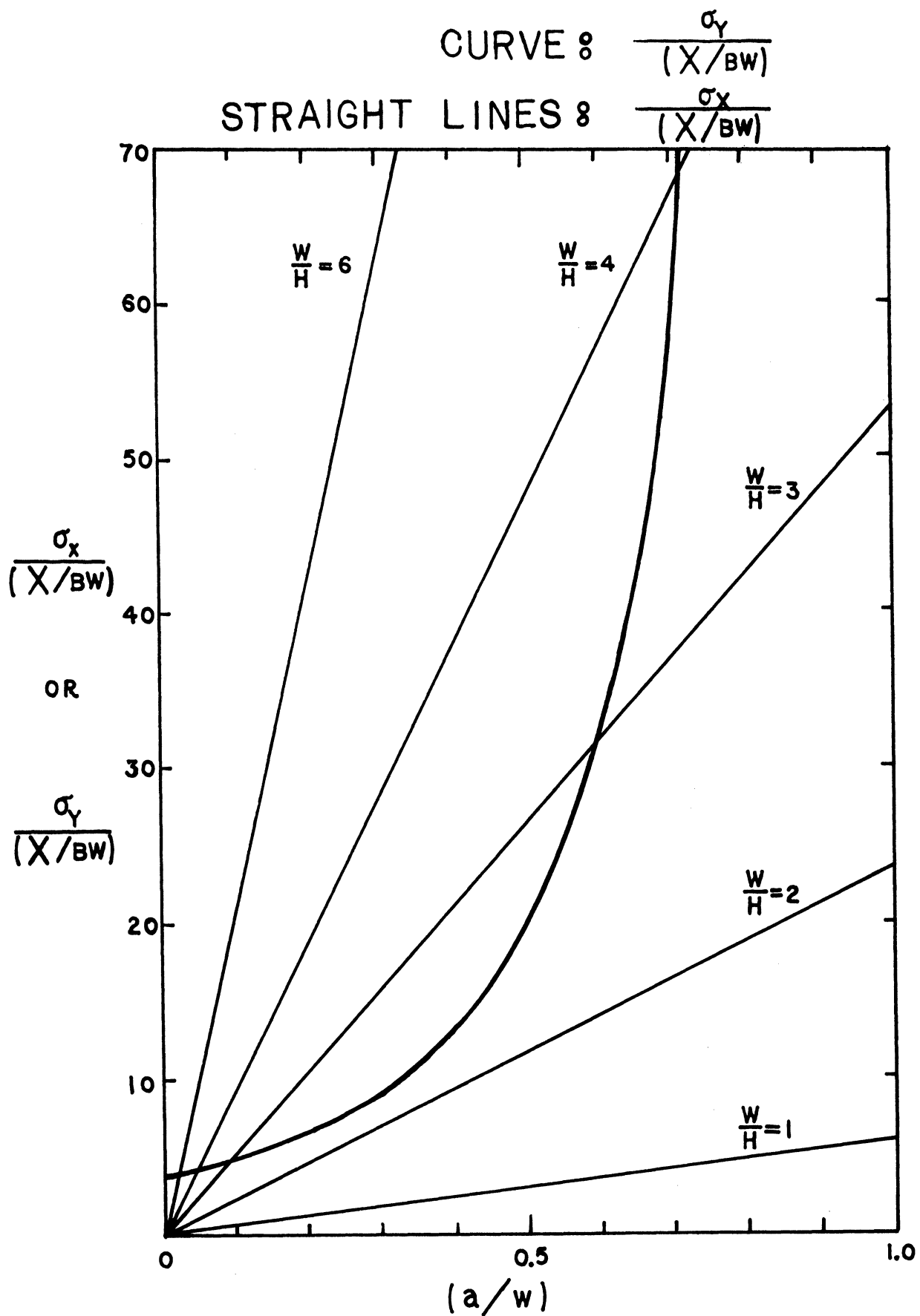


Figure 7. Comparison of stress in x-direction and stress in y-direction in a specimen shown in Figure 6 (following reference 2).

III.1.2 Modified Stress Analysis

The stress distribution along the section A-A and B-B in Figure 6 has been treated to be linear in the previous section as a first approximation. The linear stress distribution along section A-A would be;

$$\sigma_x \Big|_r = \frac{6Xa}{BH^2} \left(1 - \frac{2r}{H}\right) \quad (3.3)$$

Similarly, along the section B-B,

$$\sigma_y \Big|_r = \frac{3X(W+a)}{B(W-a)^2} \left\{1 - \frac{2r}{(W-a)}\right\} + \frac{X}{B(W-a)} \quad (3.4)$$

where r is the distance measured from the crack tip. Section B-B is not, in practice, part of a simple beam and a sharp notch at the crack tip causes high stress concentration. Therefore, a more realistic stress distribution along section B-B should 1) account for the stress concentration and 2) also satisfy the static equilibrium condition with the external load and moment.

The stress distribution around the crack along section B-B can be obtained from the linear elastic fracture mechanics expression as equation (2.17).

By putting $\theta=0$,

$$\sigma_y \Big|_r = \frac{K}{\sqrt{2\pi r}} + o(1) \quad (3.5)$$

K is the stress intensity factor which is a function of the specimen geometry and external load, and it can be determined experimentally through the compliance calibration described in section II.3. $\sigma(1)$ is the nominal stress level along section B-B which is usually ignored because it is considered to be small compared to the first term. This assumption is appropriate when the size of the specimen is large compared to the crack length, but it is not so accurate when the size of the specimen becomes comparable to the crack length. This is the case in the compact tension specimen used in this study. Then equation (3.5) predicts only tensile component of stress and this stress state alone cannot satisfy equilibrium condition of the test piece under external load and moment. The expression that will satisfy both stress concentration at the notch and static equilibrium of the system would more likely have the form;

$$\sigma_y \Big|_r = \frac{K}{\sqrt{2\pi r}} + C_1 - C_2 r \quad (3.6)$$

where C_1 and C_2 are constants to be determined from the static equilibrium condition. An analysis has been made for the specimen geometry shown in Figure 8, as follows:

From force equilibrium,

$$X = \int_0^b (\sigma_y \cdot B) dr \quad (3.7)$$

From moment equilibrium,

$$XW = \int_0^b (\sigma_y \cdot B)(b-r)dr \quad (3.8)$$

where b equals (W-a).

Introducing equation (3.6) into equation (3.7) and (3.8), the unknown constants C_1 and C_2 can be determined.

$$C_1 = \frac{X}{Bb} + \frac{6X}{Bb^2} \left(W - \frac{b}{2} \right) - \frac{4K}{\sqrt{2\pi b}} \quad (3.9)$$

$$C_2 = \frac{12X}{Bb^3} \left(W - \frac{b}{2} \right) - \frac{4K}{b\sqrt{2\pi b}}$$

Introducing the two constants into equation (3.6),

$$\sigma_y \Big|_r = \frac{K}{\sqrt{2\pi r}} \left[1 - 4 \left(\frac{r}{b} \right)^{\frac{1}{2}} \left(1 - \frac{r}{b} \right) \right] + \frac{X}{Bb} + \frac{3X(2W-b)}{Bb^2} \left(1 - \frac{2r}{b} \right) \quad (3.10a)$$

or, substituting b by (W-a),

$$\sigma_y \Big|_r = \frac{K}{\sqrt{2\pi r}} \left[1 - 4 \left(\frac{r}{W-a} \right)^{\frac{1}{2}} \left(1 - \frac{r}{W-a} \right) \right] + \frac{X}{B(W-a)} + \frac{3X(W+a)}{B(W-a)^2} \left(1 - \frac{2r}{W-a} \right) \quad (3.10b)$$

Note that equation (3.10b) has the same expression as equation (3.4), except for one additional term to account for the presence of a sharp notch.

Stress distribution along the section A-A in Figure 6 can also be derived by a similar method. The distribution of

stress in x-direction, σ_x along section A-A in Figure 6 can be obtained from equation (2.17).

$$\begin{aligned} \sigma_x \Big|_r &= \frac{K}{\sqrt{2\pi r}} \cos(\pi/4) \{1 + \sin(\pi/4) \sin(3\pi/4)\} + 0'(1) \\ &= \frac{K}{\sqrt{2\pi r}} \frac{1}{\sqrt{2}} \left(1 + \frac{1}{\sqrt{2}} \frac{1}{\sqrt{2}}\right) + 0'(1) \\ &= \frac{1.5}{\sqrt{2}} \frac{K}{\sqrt{2\pi r}} + 0'(1) \\ &\approx \frac{K}{\sqrt{2\pi r}} + 0'(1) \end{aligned} \tag{3.11}$$

$0'(1)$ is the nominal stress level which is the linear bending stress not to be ignored for a finite specimen size.

Introducing the nominal bending stress terms,

$$\sigma_x \Big|_r = \frac{K}{\sqrt{2\pi r}} + C'_1 - C'_2 r \tag{3.12}$$

where both constants C'_1 and C'_2 are to be determined using the force and moment equilibrium conditions given as equation (3.7) and equation (3.8), respectively.

$$\begin{aligned} C'_1 &= \frac{6Xa}{BH^2} - \frac{4H}{\sqrt{2\pi H}} \\ C'_2 &= \frac{12Xa}{BH^3} - \frac{4K}{H\sqrt{2\pi H}} \end{aligned} \tag{3.13}$$

Introducing these two constants in equation (3.12), we get.

$$\sigma_x \Big|_r = \frac{K}{\sqrt{2\pi r}} \left[1 - 4(r/H)^{1/2}(1-r/H) \right] + \frac{6Xa}{BH^2}(1-2r/H) \quad (3.14)$$

Equation (3.10b) and equation (3.14) give more realistic expressions for the stress distribution along the section B-B and section A-A (see Figure 6) than the linear approximations given in equation (3.3) and equation (3.4), respectively. These are compared with the experimental data in the next section to show which expression is more realistic.

When equation (3.10b) and equation (3.14) are used to compare the stress, σ_x and σ_y , near the crack tip ($r \ll 1$, but $r \neq 0$), the first terms in both equations reduce to a common value, $\frac{K}{\sqrt{2\pi r}}$. The remaining terms in each equation have the same form as the results from linear analysis in equations (3.3) and (3.4). So the difference of these two stresses, σ_x and σ_y , at the crack tip using the refined equations (3.10b), and (3.14), is equal to the difference of stresses from to ex- analysis in equations (3.1a) and (3.1b). This seems to explain why the crack path predictions from linear analysis were in good agreement with the actual crack paths, which is determined by the relative magnitude of the stress compoments, σ_x and σ_y , at the current crack tip. So the crack path prediction based on linear analysis given in previous section is still valid. And Figure 7 can be used as a guide for designing a fracture specimen for straight paths.

In summary, stress distribution along the section

B-B and A-A are (see Figure 6 and 8 for symbols),

- 1) From a linear stress analysis,
stress along section A-A;

$$\sigma_x \Big|_r = \frac{6Xa}{BH^2} (1-2r/H) \quad (3.3)$$

stress along section B-B;

$$\sigma_y \Big|_r = \frac{3X(W+a)}{B(W-a)^2} \left(1 - \frac{2r}{W-a}\right) + \frac{X}{B(W-a)} \quad (3.4)$$

where r represents the distance measured from the crack tip in either x - or y - direction.

- 2) From linear elastic fracture mechanics,
stress along section B-B;

$$\sigma_y \Big|_r = \frac{K}{\sqrt{2\pi r}} \quad (3.5)$$

stress along section A-A;

$$\sigma_x \Big|_r = \frac{K}{\sqrt{2\pi r}} \quad (3.11)$$

- 3) From modified stress analysis,
stress along section B-B;

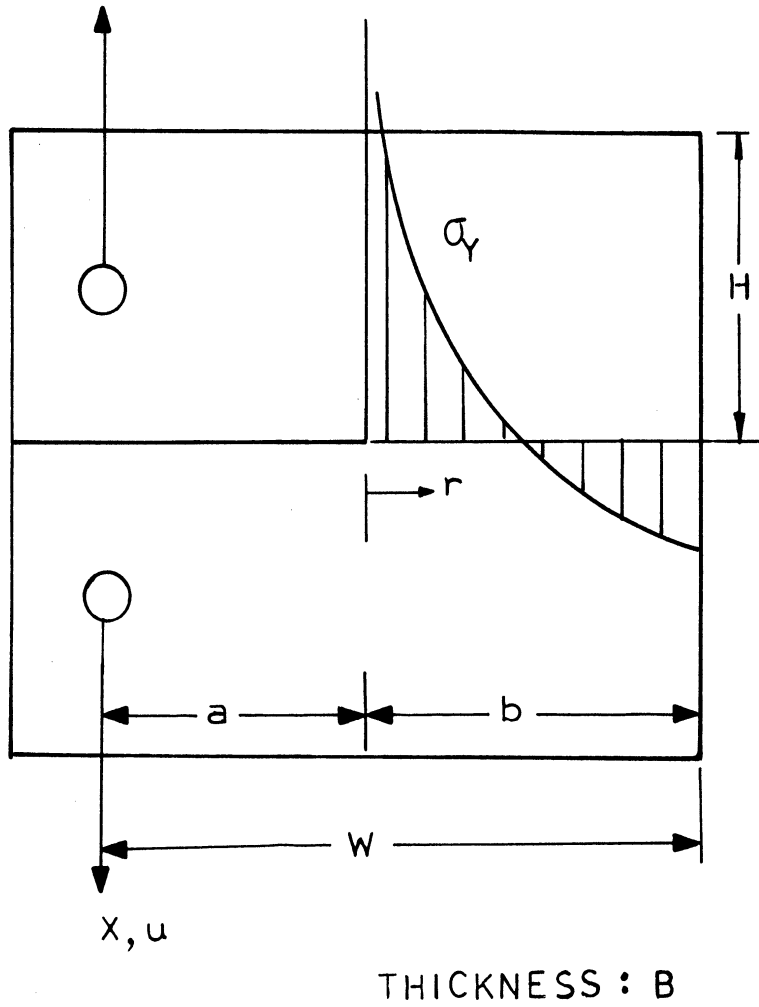


Figure 8. Stress state along the expected crack path

$$\sigma_y \Big|_r = \frac{K}{\sqrt{2\pi r}} \left[1 - 4 \left(\frac{r}{W-a} \right)^{\frac{1}{2}} \left(1 - \frac{r}{W-a} \right) \right] + \frac{3X(W+a)}{B(W-a)^2} \left(1 - \frac{2r}{W-a} \right) + \frac{X}{B(W-a)} \quad (3.10b)$$

stress along section A-A;

$$\sigma_x \Big|_r = \frac{K}{\sqrt{2\pi r}} \left[1 - 4 \left(\frac{r}{H} \right)^{\frac{1}{2}} \left(1 - \frac{r}{H} \right) \right] + \frac{6Xa}{BH^2} (1 - 2r/H) \quad (3.14)$$

III.2 Experimental measurement of stress distribution along the crack path

The stress distribution along the expected crack path was measured experimentally in order to check which analysis is most realistic.

Four PMMA specimens had identical geometries: B=5.9 mm (0.233 in), W=101.6 mm (4 in), H=60.9 mm (2.4 in) and the initial crack length a=50.8 mm (2 in). Strain gages were attached on each specimen at pertinent locations to measure the strains at various locations along the expected crack path. Strain gages were chosen that matched thermal expansion coefficients of the PMMA sheets used in this test. The types of gages used were BAE-13-125AA-350-TE made by BEAN company. A two gage-bridge was employed; one gage was attached to the actual specimen and the other to a dummy

specimen. First, a calibration of stress and strain in terms of output voltage was established from a uniaxial tensile test where a strain gage was mounted on a gage section of the tensile specimen. Traces of stress, strain and output voltage were recorded simultaneously. Figure 9 shows the calibration curve obtained from the tensile test. After the calibration was completed, each fracture specimen was loaded on an Instron machine at a crosshead speed of 8.33 $\mu\text{m}/\text{sec}$ (0.02 in/min). The load X was recorded on the Instron chart paper and voltage output from the strain gage mounted at various points along the crack path was amplified by Ellis Bridge Amplifier and then recorded on x-y-y plotter. Figure 10 shows the location of the gages along the expected crack path. All four locations are shown on one test piece for convenience. (Actually only one gage is mounted on each of the four identical test pieces at locations shown in Figure 10).

Figure 11 shows the stresses, σ_y , at various locations of the specimen, the load, X , and the crack length, 'a', as function of time. Note that compressive stresses are recorded initially for all locations except for gage No. 1. Stress at each location shows linear behavior as a function of time until the crack initiates. As the crack starts, the stress state deviates from the linear relationship with the applied load and as the crack approaches the strain gage location, the stress rises sharply into tensile

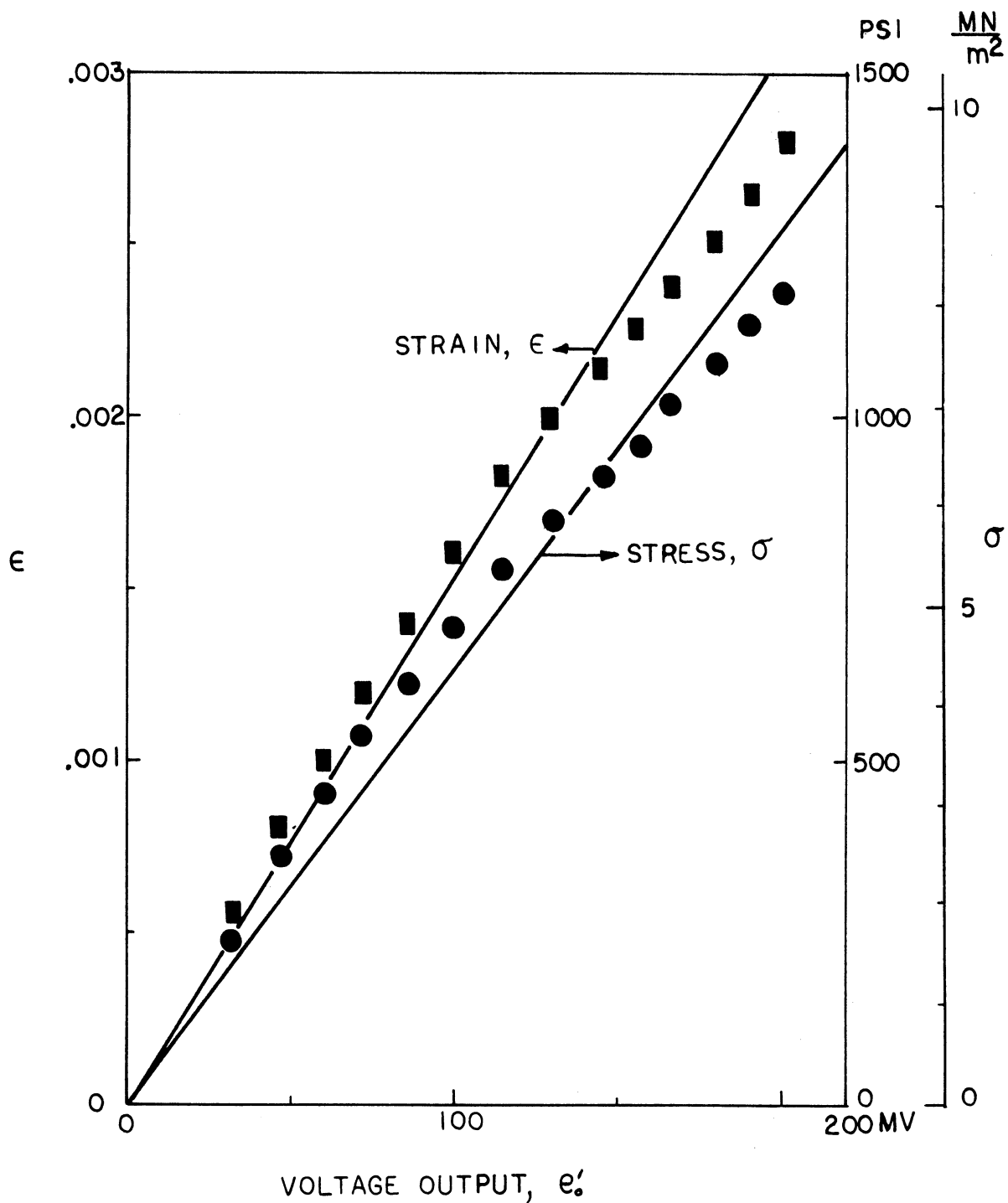
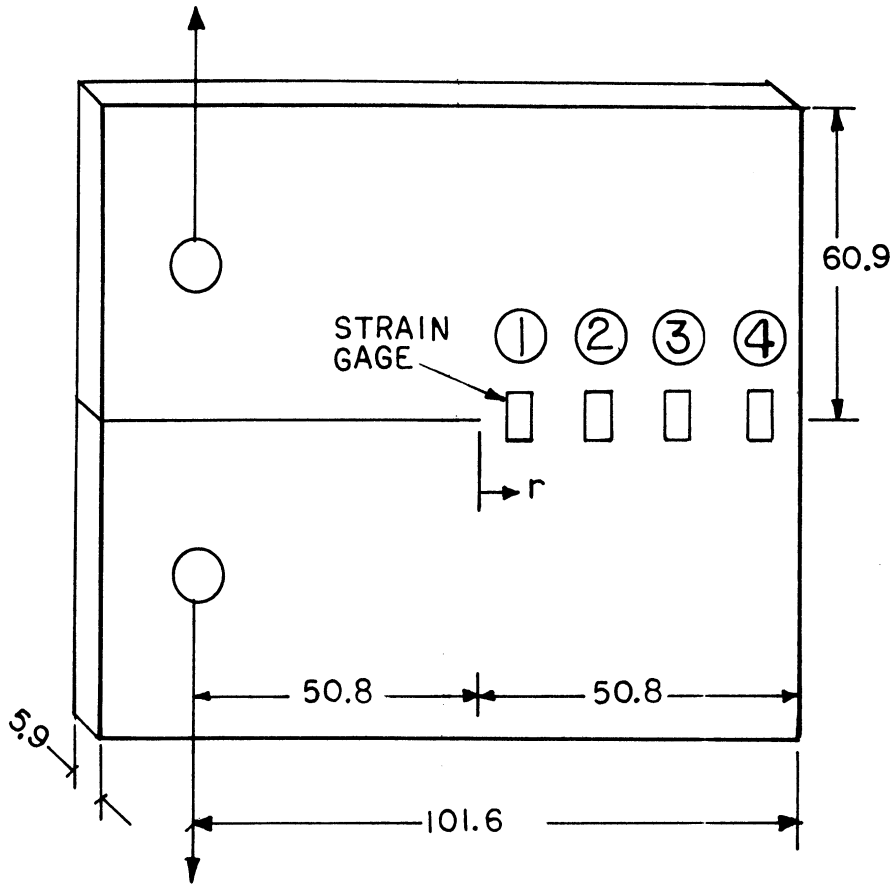


Figure 9. Strain gage calibration curve and stresses calculated from uniaxial tension



UNITS IN mm

ONE STRAIN GAGE ON EACH OF THE 4 IDENTICAL TEST PIECES : 1,2,3,4

GAGE LOCATION	SPECIMEN NUMBER			
	1	2	3	4
r (mm)	6.35	19.05	31.75	44.5

Figure 10. Sequential location of strain gages on the four fracture specimens

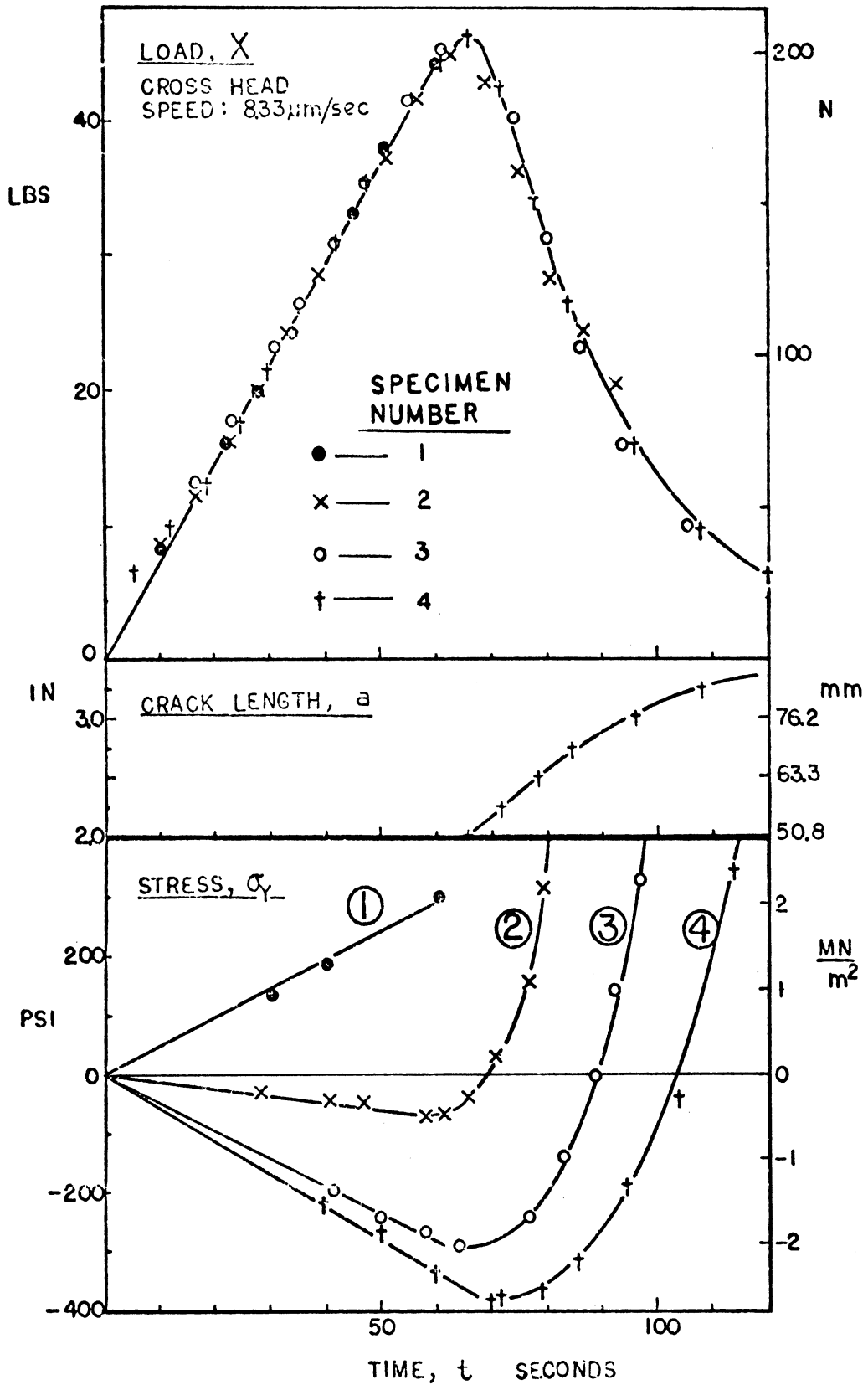


Figure 11. Load, crack length and presumed stress as a function of time. Numbers in stress-time plot indicate strain gage number in Figure 10.

values in a very short time.

The stress distributions predicted from the three analyses are compared with the experimental results before crack initiation, in Figure 12. For the specimen geometry used in the experiment (see Figure 10), equations (3.4), (3.5) and (3.10b) reduce to;

from equation (3.4),

$$\begin{aligned} \frac{\sigma_y}{(X/Bb)} \Big|_r &= 1 + \frac{3(1+a/W)}{(1-a/W)} \left(1 - \frac{2r}{b}\right) \\ &= 1 + \frac{3(1+.5)}{(1-.5)} \left(1 - \frac{2r}{b}\right) \\ &= 1 + 9\left(1 - \frac{2r}{b}\right) = 10 - 18(r/b) \end{aligned}$$

from equation (3.5),

$$\begin{aligned} \frac{\sigma_y}{(X/Bb)} \Big|_r &= \frac{KBb}{X\sqrt{2\pi r}} = \frac{KBb^{1/2}}{X\sqrt{2\pi(r/b)}} \\ &= \frac{KBW^{1/2}(1-a/W)^{1/2}}{X\sqrt{2\pi(r/b)}} \\ \frac{KBW^{1/2}}{X} &= 9.79 \text{ obtained from Srawley et al (1973)} \\ \frac{\sigma_y}{(X/Bb)} \Big|_r &= \frac{9.79(1-0.5)}{\sqrt{2\pi}} (r/b)^{-1/2} \\ &= 2.76 (r/b)^{-1/2} \end{aligned}$$

from equation (3.10b),

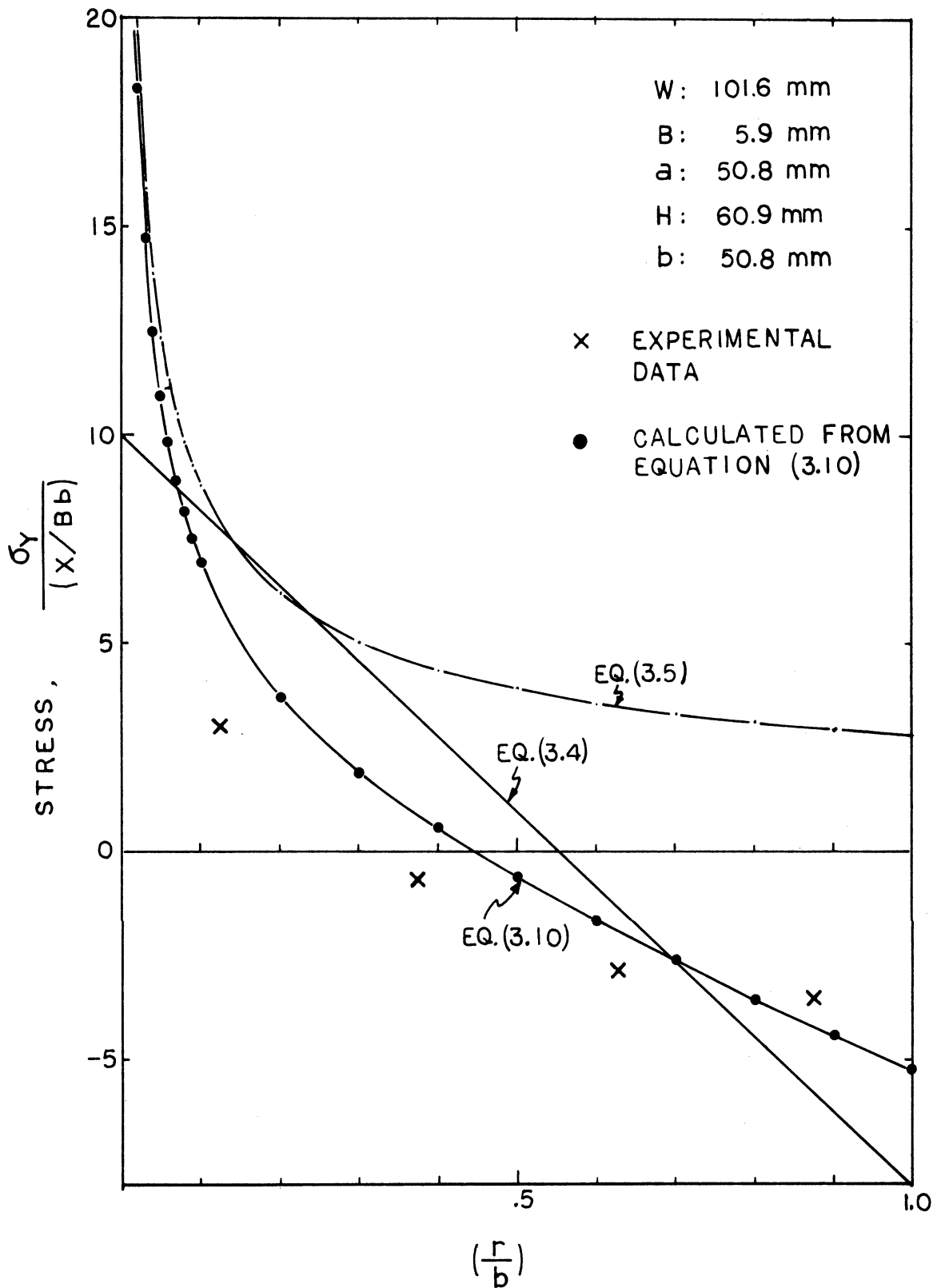


Figure 12. Comparison of various analyses with experimental results

$$\frac{\sigma_y \Big|_r}{(X/Bb)} = 2.76(r/b)^{-\frac{1}{2}} \{1 - 4(r/b)^{\frac{1}{2}}(1-r/b)\} + 10 - 18(r/b)$$

Above three equations are compared with the experimental results in Figure 12. There exists a considerable difference between the analytical solutions and the experimental data. Among the three, equation (3.10b) gives a closest value to the experimental points. Equation (3.10b) is a more refined analysis compared to the linear analysis, but it still needs further refinement. This is out of the scope of the present work.

III.3 Crack speed analysis

The crack speed analysis in this section deals with the case when cleavage specimens of various geometries are pulled at constant crosshead speed \dot{u} . The crack is assumed to move quasi-statically such that there exists an equilibrium crack length, a , and load, X , for a given crosshead displacement, u . This equilibrium load, X , and crack length, a , at a given crosshead displacement, u , are in turn, a function of the fracture toughness, R , of a material as well as specimen geometry. Consequently, in the case of quasi-static equilibrium cracking, the crack length, a , can be uniquely determined for a given crosshead displacement, u . da/du is equivalent to $\frac{da/dt}{du/dt} = \dot{a}/\dot{u}$, thus, crack speed during fracture of a specimen at constant crosshead speed, \dot{u} , can be obtained from the information of the rate of the

change of crack length against crosshead displacement, i.e., da/du. Thus da/du was obtained from the following procedure.

1)
$$\frac{KBW^{\frac{1}{2}}}{X} = [Y(a)]_{W.H.B} \quad (3.15)$$

2) Applying equation (3.15) to equation (2.19b),

$$\frac{K^2 B^2 W}{X} = \frac{EBW}{2} \frac{d(u/X)}{da} = [Y(a)]_{W.H.B}^2 \quad (3.16)$$

where Y(a) is a function of specimen geometry, which is available in the literature.

3) By integrating equation (3.16) with respect to "a",

$$u/X = Z(a)]_{W.H.B} \quad (3.17)$$

4) Introducing equation (3.15) into (3.17),

$$u = \frac{KBW^{\frac{1}{2}}}{Y(a)} \cdot Z(a)$$

since $K = \sqrt{ER}$,

$$u = \frac{B\sqrt{ERW}}{Y(a)} \cdot Z(a) \quad (3.18)$$

5) Equation (3.18) describes displacement, u, as an explicit function of crack length, a, so it is possible to differentiate it with respect to "a",

$$\frac{du}{da} = \frac{d}{da} \left[\frac{B\sqrt{ERW}}{Y(a)} \cdot Z(a) \right] \quad (3.19)$$

since,

$$du/da = \dot{u}/\dot{a}$$

$$\dot{a}/\dot{u} = \frac{1}{(du/da)} = \frac{1}{\frac{d}{da} \left[\frac{B\sqrt{ERW}}{Y(a)} \cdot Z(a) \right]} \quad (3.20)$$

Since the crosshead speed $\dot{u} = \text{constant}$, \dot{a} can be obtained by multiplying the \dot{a}/\dot{u} by \dot{u} . Only two types of specimen geometry were considered in this analysis. One is compact tension specimen which has the geometry $W/H \leq 2$, and the other is semi-infinite specimen which has the geometry, $W/H \geq a/H + 2$. Analysis of crack speed is valid for the straight crack path only and so it will be applicable for the specimen with the geometry that will give straight crack path throughout the test (Refer to Figure 7). As shown in Figure 7, one of the ways to generate straight cracks irrespective of crack length is to use specimen geometry: $W/H \leq 2$. For the slender specimen with $W/H \gg 2$, side grooves would be made along the median line of the specimen to generate a straight crack path along the grooved line. Crack speed analysis for these two types of specimen geometry will be given in the following two sections.

III.3.1 Crack speed analysis for the compact tension specimen ($W/H \leq 2$)

The stress intensity factor of a semi-infinite notch approaching the free edge of half-plane was solved by Paris and Sih (1965); Srawley and Gross (1966) reformulated it non-dimensionally to use with the compact tension specimen. We have,

$$\frac{KBW^{\frac{1}{2}}}{X} = \frac{0.537+(2.17) \cdot \frac{(1+a/W)}{(1-a/W)}}{(1-a/W)^{\frac{1}{2}}} = Y(a/W) \quad (3.21)$$

From equation(2.20b)

$$\frac{K^2 B^2 W}{X^2} = \frac{EB}{2} \frac{d(u/X)}{d(a/W)}$$

Combining equation(2.20b) and (3.21)

$$\frac{EB}{2} \frac{d(u/X)}{d(a/W)} = \frac{\left[0.537+(2.17) \frac{(1+a/W)}{(1-a/W)}\right]^2}{(1-a/W)} = \left[Y(a/W)\right]^2 \quad (3.22)$$

Equation(3.22) can be integrated with respect to (a/W), and the result is;

$$\begin{aligned} \frac{EB}{2}(u/X) &= -2.666 \log_e(1-a/W) - \frac{14.172}{(1-a/W)} + \frac{9.416}{(1-a/W)^2} \\ &+ 4.756 + C_0 = \frac{1}{2} Z(a/W) \end{aligned} \quad (3.23)$$

The integration constant C_0 is determined from the compliance of the specimen with zero crack length,(u/X). From this C_0

can be determined by $C_o = \frac{EB}{2}(u/X)$. This quantity is not negligible and it can be obtained from actual compliance measurements of rectangular shaped specimens with no cracks present. Compliances were measured on a PMMA compact tension specimen using the displacement gage shown in Figure 22. For $W=101.6$ mm (4 in.), $H=61$ mm (2.4 in.), $B=6.35$ mm (0.25 in.) $a=0$ mm it was found that,

$$(u/X)_o = 4.1 \times 10^{-5} \text{ (in/lb)} = 0.2345 \times 10^{-6} \text{ (m/N)}$$

with $E=3.24$ GN/m² (470,000 psi),

$$C_o = \frac{EB}{2} (u/X)_o = 2.41$$

Alternatively, C_o can be obtained by considering the limiting case of Figure 6, where the crack length $a=0$.

σ_y at $r=0$ is;

$$\begin{aligned} \sigma_y \Big|_o &= \frac{X}{BW} + \frac{\{X \cdot (W/2)\} \cdot (W/2)}{I_{A-A}} = \frac{X}{BW} + \frac{XW(W/2)}{BW^3/12} \\ &= \frac{X}{BW} + \frac{3X}{BW} = \frac{4X}{BW} \end{aligned}$$

$$\sigma_y \Big|_o = \frac{4X}{EBW} = u/H$$

$$\text{so } C_o = \frac{EB}{2}(u/X) = \frac{2H}{W} \quad (3.24)$$

For the specimen geometry used in the actual compliance

measurement given above, equation (3.24) gives $C_0=1.2$. This is about half of the measured value. Considering that this is a simplified analysis not counting the complex stress state around the loading pin, this difference is not surprising. For the present analysis, the actual measured value of $C_0=2.41$ was used in equation (3.23). From equation (3.23),

$$\frac{u}{X} = \frac{1}{EB} Z(a/W) \quad (3.25)$$

From equation (3.21),

$$X = \frac{KBW^{1/2}}{Y(a/W)} \quad (3.26)$$

Since $K=\sqrt{ER}$

$$X = \frac{\sqrt{ER} BW^{1/2}}{Y(a/W)} \quad (3.27)$$

Substituting X in equation (3.25) by equation (3.27),

$$\begin{aligned} u &= \frac{1}{EB} Z(a/W) \frac{\sqrt{ERW} B}{Y(a/W)} = \frac{1}{E} \frac{Z(a/W)}{Y(a/W)} \sqrt{ERW} \\ &= \sqrt{\frac{RW}{E}} \frac{Z(a/W)}{Y(a/W)} \end{aligned} \quad (3.28)$$

Now that the displacement, u, is expressed in terms of a single variable, (a/W), the differentiation of u in terms of (a/W) is possible. The expression for crack speed can be obtained from the following procedure:

Differentiating equation(3.28),

$$\begin{aligned} \frac{du}{da} &= \frac{du}{Wd(a/W)} = \frac{1}{W} \sqrt{\frac{RW}{E}} \frac{d}{d(a/W)} \left[\frac{Z(a/W)}{Y(a/W)} \right] \\ &= \sqrt{\frac{R}{EW}} \frac{d}{d(a/W)} \left[\frac{Z(a/W)}{Y(a/W)} \right] \end{aligned} \quad (3.29)$$

The function $\left[Z(a/W)/Y(a/W) \right]$ has a complex form and differentiating this function analytically involves a tremendous effort. Consequently, the differentiation was performed numerically by computer. Differentiation interval $\Delta(a/W)$ was set to be 0.025. When these values of du/da were obtained numerically, the reciprocal of these value taken to be da/du . So,

$$\dot{a}/\dot{u} = da/du = \frac{1}{du/da} \quad (3.30)$$

In order to plot these values irrespective of material properties such as E and R, a crack speed parameter that contains these property parameters is used in Figure 13,i.e., $\sqrt{\frac{R}{EW}} \frac{\dot{a}}{\dot{u}}$.

The analytical result of equation (3.30) was compared with the actual crack speed data. Table 1 shows the experimental crack speed data. The first two sets of data i) and ii) were obtained using a movie camera when the PMMA compact tension specimen was pulled at crosshead speed of $\dot{u}=83.3$ m/s (0.2 in/min) and 333 m/s (0.4 in/min), respectively. The specimen geometry used in obtaining each set of data was identical except for crack length (see table 1).

TABLE 1
EXPERIMENTAL CRACK SPEED DATA

Material: PMMA

Specimen Geometry: W=101.6 mm(4")

H= 61 mm(2.4")

B= 6.35 mm(0.25")

1) $\dot{u}=83.3 \mu\text{m}/\text{sec}(0.2 \text{ in}/\text{min})$

Crack speed measured by a movie camera

Crack length: $a_0=50.8 \text{ mm}(2")$

Crack speed range: 1.69 to 8.38 mm/sec

Young's Modulus: $E= 3.20 \text{ GN}/\text{m}^2(470,000 \text{ psi})$

\bar{R} for this range: $481.5 \text{ J}/\text{m}^2(2.75 \text{ lb-in}/\text{in}^2)$

Film speed: 8 Frames/sec

a(mm)	Frame No.	a/W^\dagger	$\dot{a}(\text{mm}/\text{sec})^\dagger$	\dot{a}/\dot{u}^\dagger	$\sqrt{\frac{R}{EW}}(\dot{a}/\dot{u})^\dagger$
50.8	0				
		0.516	6.35	75	0.092
54	4	0.546	8.38	99.1	0.121
57.2	7	0.578	8.38	99.1	0.121
60.3	10	0.6075	6.35	75	0.092
63.5	14	0.640	5.08	60	0.074
66.7	19	0.672	6.35	75	0.092
69.9	23	0.703	5.08	60	0.074
73.0	28	0.734	4.24	50	0.061
76.15	34	0.766	2.82	33.3	0.041
79.4	43	0.797	3.175	37.5	0.046
82.3	51	0.828	1.691	20	0.025
85.6	66				

TABLE 1 (CONTINUED)

ii) $\dot{u}=333 \mu\text{m}/\text{sec}(0.79 \text{ in}/\text{min})$

Crack speed measured by a movie camera

Crack length: $a= 50.8 \text{ mm}(2")$

Crack speed range: 3.7 to 35 mm/sec

Young's modulus: $E= 3.20 \text{ GN}/\text{m}^2(470,000 \text{ psi})$

\bar{R} for this range: $569 \text{ J}/\text{m}^2(3.25 \text{ lb-in}/\text{in}^2)$

Film speed: 16 Frames/sec

$a(\text{mm})$	Frame N_0	a/W^\dagger	$\dot{a}(\text{mm}/\text{sec})^\dagger$	\dot{a}/\dot{u}^\dagger	$\sqrt{\frac{\bar{R}}{EW}} (\dot{a}/\dot{u})^\dagger$
68.9	3				
		0.683	14.7	44	0.058
69.82	4				
		0.6955	25.25	75.7	0.100
71.4	5				
		0.711	25.6	76.9	0.103
73	6				
		0.73	28.8	86.5	0.1115
75.2	7				
		0.749	25.6	76.9	0.103
76.8	8				
		0.766	29.6	88.9	0.1183
78.75	9				
		0.781	20	60	0.0797
80	10				
		0.795	25.6	76.8	0.100
81.6	11				
		0.810	19.2	57.6	0.0765
82.8	12				
		0.83	15.7	47.1	0.0626
85.75	15				
		0.855	11.7	35.1	0.0456
87.95	18				
		0.874	8.3	24.9	0.0331
89.5	21				
		0.892	8.4	25.2	0.03345
91.6	25				
		0.908	5.9	17.7	0.02355
92.7	28				

TABLE 1 (CONTINUED)

iii) $\dot{u} = 8.33 \text{ } \mu\text{m/sec (0.02 in/min)}$

Crack speed measured visually

Crack length : $a_0 = 30.48 \text{ mm (1.2")}$

Crack speed range: 0.16 to 1.33 mm/sec

Young's Modulus : $E = 3.20 \text{ GN/m}^2 \text{ (470,000 psi)}$

R for this range : $394 \text{ J/m}^2 \text{ (2.25 lb-in/in}^2 \text{)}$

a/W	\dot{a}/\dot{u}	$\sqrt{\frac{R}{EW}} (\dot{a}/\dot{u})$
0.365	160	0.179
0.425	140	0.157
0.485	140	0.157
0.55	140	0.157
0.625	127	0.142
0.7	111	0.124
0.785	71	0.079
0.84	64	0.072
0.9	19	0.021

† Each number in these columns is an average value of the parameter in the interval of crack lengths shown in the first column.

The third set of data was obtained by tracing the crack location visually on a PMMA specimen which was pulled at slow speed (8.33 $\mu\text{m/s}$ or 0.02 in/min). At this slow crosshead speed, the crack was moving at such a slow speed that it was possible to make a pip mark on the chart paper whenever the crack passed marks of 6.35 mm (1/4 in) intervals that had been scribed prior to testing. In calculating $\sqrt{\frac{R}{EW} \frac{\dot{a}}{u}}$, a constant R value was used by taking the average of the fracture toughness values obtained in the corresponding crack speed range (see chapter IV). Young's modulus was assumed to be constant in this range of testing speeds at $E=3.24 \text{ GN/m}^2$ (470,000 psi), the value obtained from a uniaxial tensile test of PMMA at a strain rate of $\dot{\epsilon} \approx 10^{-4}/\text{sec}$ (see chapter IV for the detailed analysis on equivalent strain rate during the fracture test).

Both the analytical and the experimental crack speed data are shown in Figure 13. The experimental data obtained at $\dot{u}=83.3 \mu\text{m/s}$ (0.2 in/min) are in close agreement with the analytical crack speed curve, but the crack speeds obtained from $\dot{u}=333 \mu\text{m/s}$ (0.79 in/min) show a considerable deviation. The absence of data points between $a/W=0.5$ to 0.68 for $\dot{u}=333 \mu\text{m/s}$ is because the crack jumped unstably at the initiation and it was arrested at $a/W=0.68$. From this point on the crack started to move quasi-statically. An upward trend around $a/W=0.7$ is caused by the crack starting from zero speed to the equilibrium speed. The crack speed data obtained from $\dot{u}=8.33 \mu\text{m/s}$ (0.02 in/min) also shows higher values

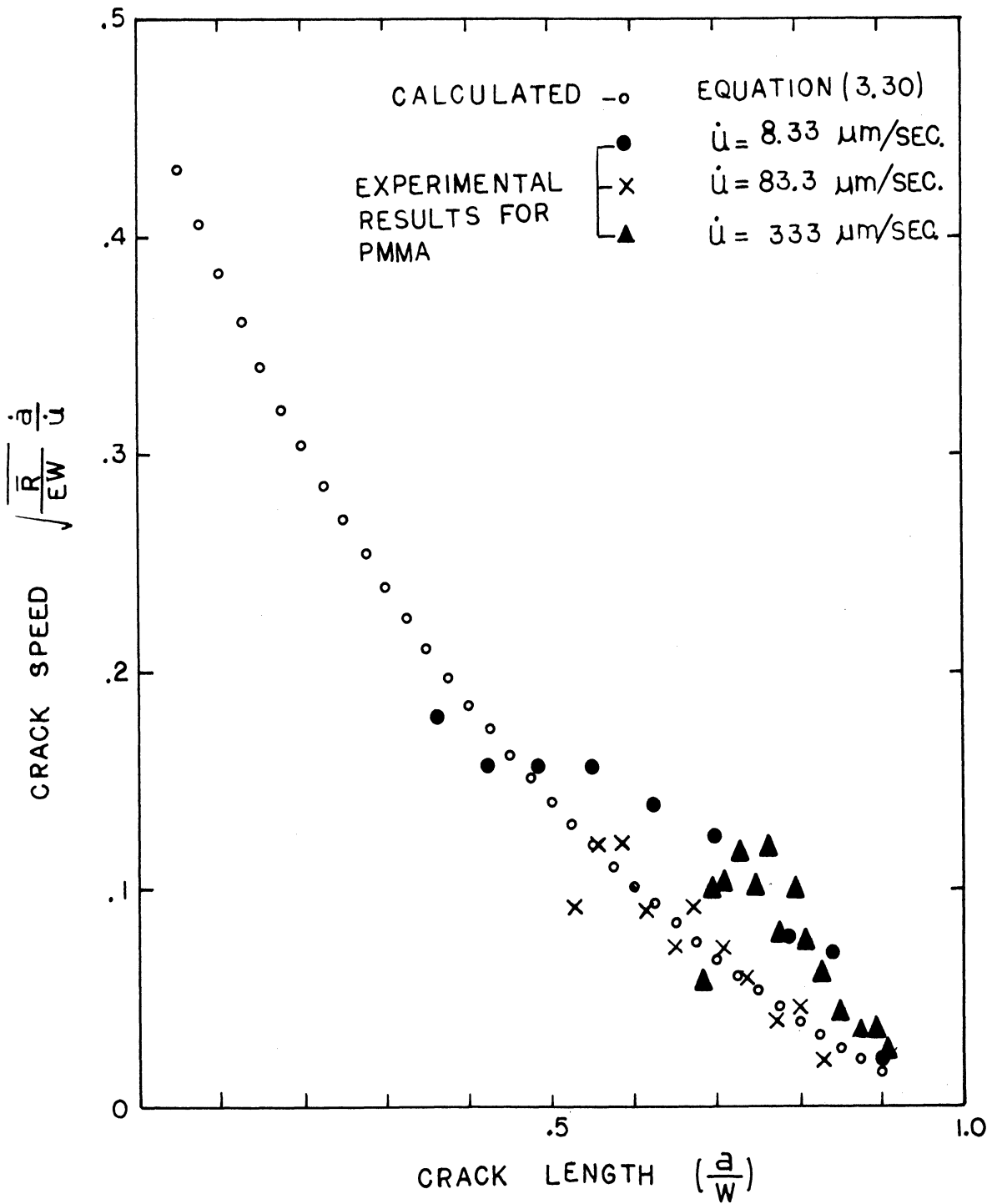


Figure 13. Comparison of experimental crack speed with the predicted values based on the present analysis (see table 1 for specimen geometry)

than the analytic results.

Yet, the crack speed predicted from the present analysis seems to coincide with the lower end of the scatter in the crack speeds as measured.

III.3.2 Crack speed analysis for semi-infinite cleavage specimen with side grooves [$W/H \geq (a/H)+2$]

It is sometimes desired to have the crack run at a very slow speed so that the fracture process can be studied visually while the crack is running, without requiring complex instrumentation. One way of achieving this slow crack speed is to use a very slow crosshead speed, but the ordinary testing machine provides only a limited range of crosshead speeds. An alternative way of achieving a slower crack speed is by adjusting the design of a specimen. An intuitive observation is that the crack speed may decrease as the cleavage specimen gets slender and becomes more compliant. However, as already shown in the first section of this chapter (refer to Figure 7) a crack has a higher tendency to turn away from the straight path as the specimen geometry becomes more slender (i.e., W/H gets larger than 2). This undesirable situation can be avoided by making a pair of side grooves along the median line of a slender cleavage specimen, as mentioned at the beginning of this chapter. The depth of the side grooves can be adjusted until a straight crack path is achieved.

Prediction of crack speeds for these side-grooved cleavage specimens will now be given in order to make a com-

parison with the available experimental data in the literature. No actual experiments with the grooved specimens were performed in the present study.

Following the same procedure as shown in the previous section, the expression for non-dimensionalized stress intensity factor for the slender specimen ($W/H \geq 2$) was first obtained using the suggestion of Srawley and Gross (1966).

$$\frac{KBH^{\frac{1}{2}}}{X} = 3.46(a/H + 0.7) \quad (3.31a)$$

The equation (3.31a) is modified to account for the effect of side grooves with the notch thickness, B_N (Johnson and Radon 1972),

$$\frac{K\sqrt{BB_N}H^{\frac{1}{2}}}{X} = 3.46(a/H + 0.7) \quad (3.31b)$$

Introducing the relationship $K=\sqrt{ER}$ into equation (3.31b) and squaring both sides,

$$\frac{ERBB_NH}{X^2} = 12(a/H + 0.7)^2 \quad (3.32)$$

Since $R = \frac{1}{2} X^2 \frac{d(u/X)}{B_N da}$ as shown in equation (2.16), equation (3.32) becomes,

$$\frac{EBH}{2} \frac{d(u/X)}{da} = 12(a/H + 0.7)^2 \quad (3.33a)$$

or

$$\frac{EB}{2} \frac{d(u/X)}{d(a/H)} = 12(a/H + 0.7)^2 \quad (3.33b)$$

By integrating equation (3.33b) with respect to (a/H),

$$(u/X) = \frac{24}{EB} \left[\frac{1}{3}(a/H)^3 + 0.7(a/H)^2 + 0.49(a/H) \right] \quad (3.34)$$

The integration constant $u/X \Big|_{a/H=0}$ was set at zero from equation (3.29), because the magnitude of this value is negligible compared to the compliance value of slender specimen when a crack is introduced.

From equation (3.32),

$$X = \frac{\sqrt{ERBB_N H}}{3.46(a/H + 0.7)} \quad (3.35)$$

Introducing equation (3.35) into equation (3.34),

$$u = 6.94 \sqrt{\frac{RH}{E} \frac{B_N}{B}} \frac{1/3(a/H)^3 + 0.7(a/H)^2 + 0.49(a/H)}{(a/H + 0.7)} \quad (3.36)$$

Differentiating equation (3.36) with respect to "a",

$$\frac{du}{da} = \frac{1}{H} \frac{du}{d(a/H)} = 6.94 \sqrt{\frac{R}{EH} \frac{B_N}{B}} \left[(a/H + 0.7) - \frac{1/3(a/H)^3 + 0.7(a/H)^2 + 0.49(a/H)}{(a/H + 0.7)^2} \right] \quad (3.37a)$$

or in other form,

$$\frac{du}{da} = 6.94 \sqrt{\frac{R}{EW} \frac{B_N}{B}} \sqrt{\frac{W}{H}} \left[(a/W)(W/H) + 0.7 - \frac{\frac{1}{3}(a/W)^3 (W/H)^3 + 0.7(a/W)^2 (W/H)^2 + 0.49(a/W)(W/H)}{\{(a/W)(W/H) + 0.7\}^2} \right] \quad (3.37b)$$

The crack speed can then be obtained from,

$$\dot{a}/\dot{u} = da/du = \frac{1}{(du/da)} \quad (3.38)$$

where dot implies the time derivative of each variable.

Calculated crack speed is plotted as a function of non-dimensional crack length in Figure 14. For convenience of plotting, a non-dimensional crack speed parameter,

$\frac{\dot{a}}{\dot{u}} \sqrt{\frac{R}{EW} \frac{B_N}{B}}$, is used. B_N/B is the ratio between the thickness

at the grooved section and the thickness of the non-grooved section. As this ratio reaches unity, this parameter has the same form as one given in the previous section for the compact tension specimen, i.e., $\frac{\dot{a}}{\dot{u}} \sqrt{\frac{R}{EW}}$. The calculated results for the compact tension specimen is also shown in Figure 14 for comparison. Table 2 contains the experimental crack speed data reported by Broutman and McGarry (1965) and they are plotted in Figure 15 together with the calculated results for the corresponding geometry. The results predicted from the present analysis are in reasonable agreement with the

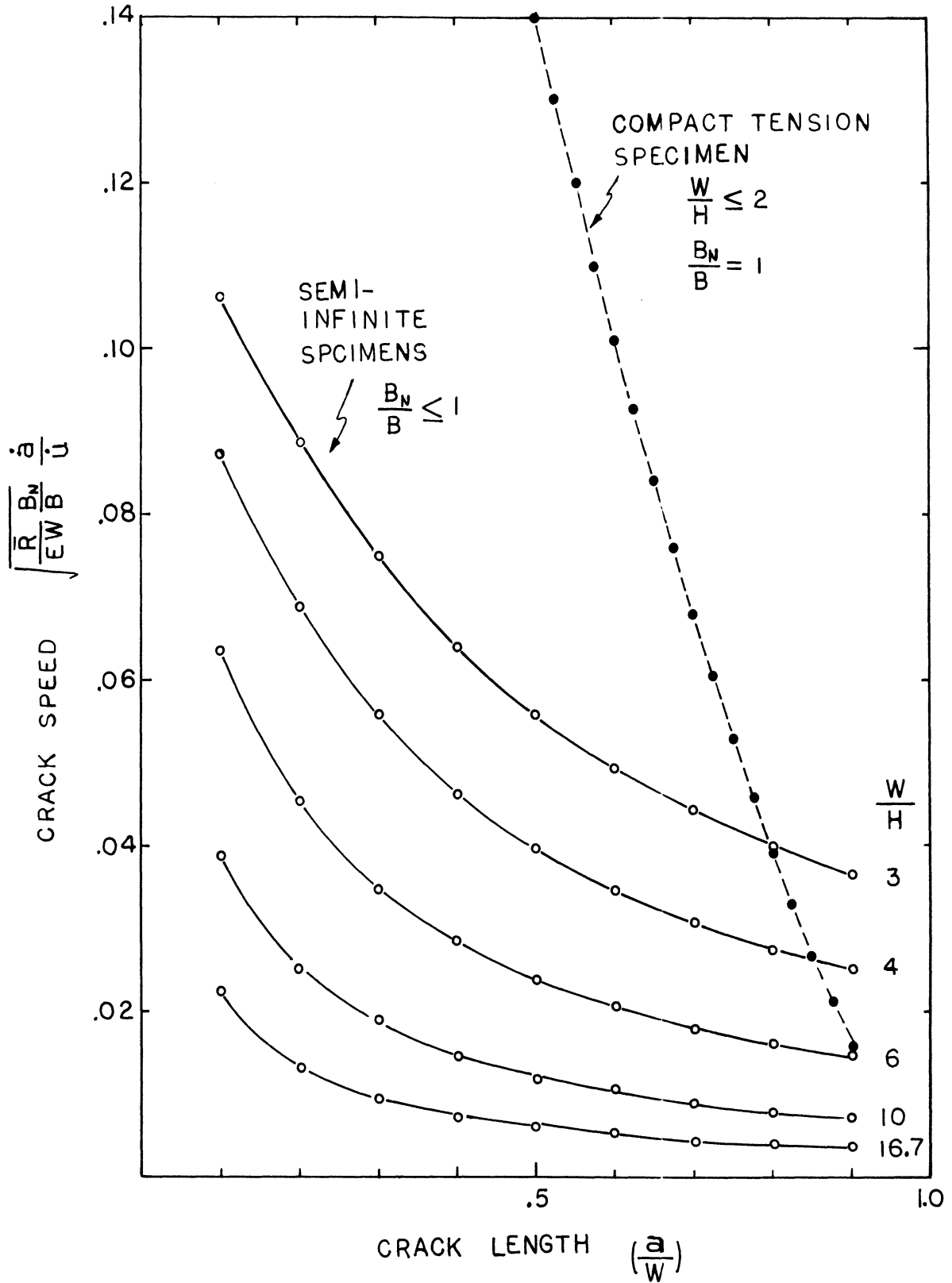


Figure 14. Calculated crack speed of cleavage specimen with $W/H \geq (a/H)+2$

TABLE 2

EXPERIMENTAL CRACK SPEED DATA FROM
A SIDE GROOVED CLEAVAGE SPECIMEN
(BROUTMAN AND MCGARRY 1965)

Material : Plexiglas II (Polymethylmethacrylate)

Crosshead speed: $\dot{u} = 83.3 \mu\text{m/sec}$ (0.2 in/min)

Specimen Geometry: $W = 254 \text{ mm}$ (10")

$H = 15.23 \text{ mm}$ (0.6")

$B = 6.35 \text{ mm}$ (0.25")

$\bar{B}_N = 3.73 \text{ mm}$ (0.147")

Young's modulus : $E = 2.83 \text{ GN/m}^2$

Average Fracture Toughness: $\bar{R} = 416 \text{ J/m}^2$ (2.38 lb/in)

a/W	$\Delta a / \Delta u$	$\sqrt{\frac{\bar{R}}{EW} \frac{B_N}{B} \frac{\dot{a}}{\dot{u}}} \times 10^3$
0.2275	25	14.52
0.2525	17.85	10.38
0.2775	17.85	10.38
0.3025	20.8	12.1
0.3275	13.9	8.08
0.3525	31.2	18.1
0.3775	12.5	7.26
0.4025	10.4	6.05
0.4275	10.4	6.05
0.4525	8.34	4.85
0.4775	8.34	4.85
0.5025	11.37	6.6
0.5275	20.8	12.1

TABLE 2 (CONTINUED)

a/W	$\Delta a/\Delta u$	$\sqrt{\frac{\bar{R}}{EW} \frac{B_N}{B} \frac{\dot{a}}{u} \times 10^3}$
0.5525	13.9	8.08
0.5775	7.35	4.27
0.6025	8.34	4.84
0.6275	8.94	5.19
0.6525	8.34	4.84
0.6775	8.94	5.19
0.7025	7.36	4.28
0.7275	5.95	3.46
0.7525	6.59	3.83
0.7775	5	2.91
0.8025	4.63	2.69

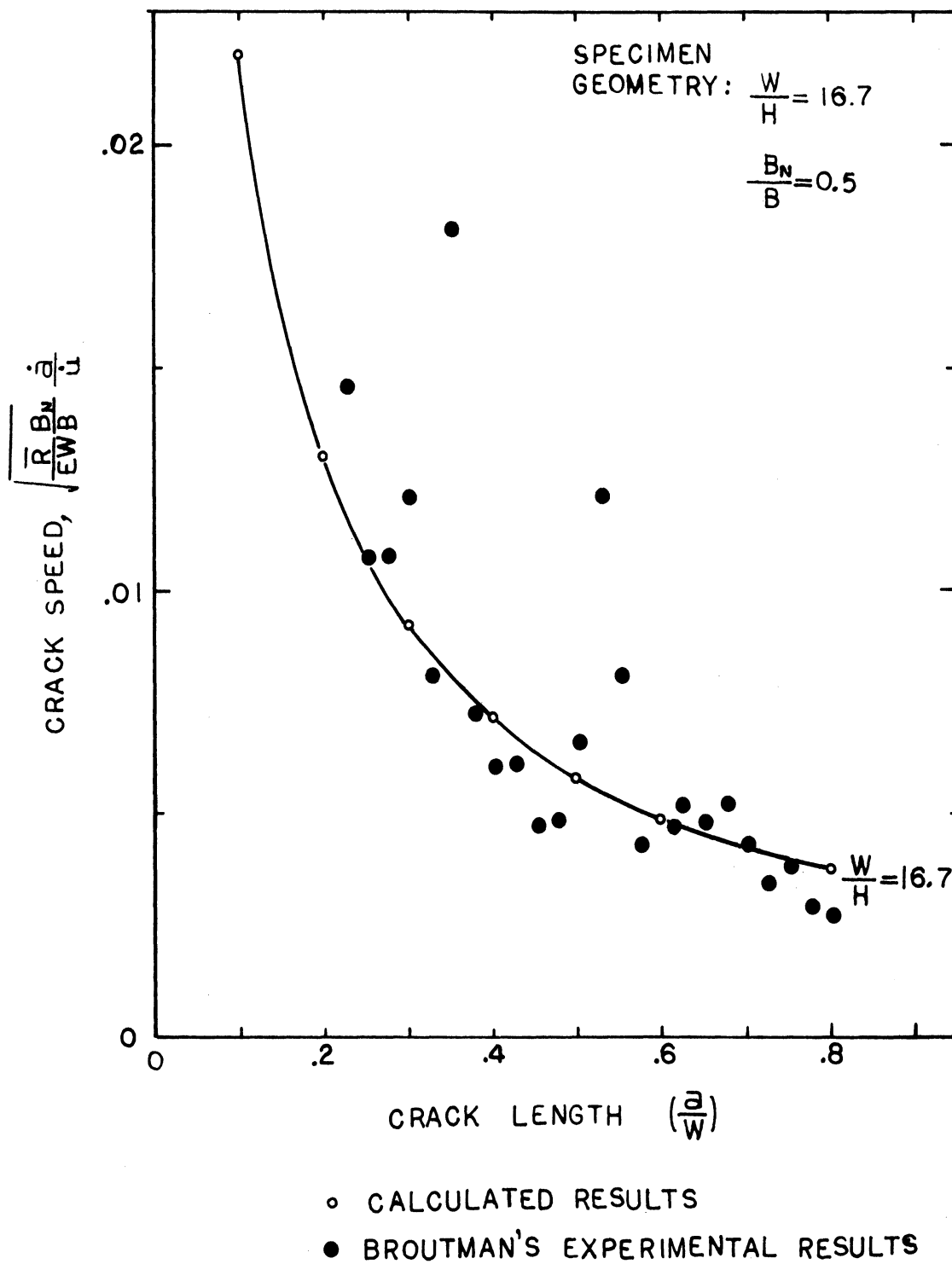


Figure 15. Comparison of calculated crack speed with the experimental crack speed reported by Broutman(1965) for PMMA

experimental data. Some of the scatter in experimental data may be due to the fact that the crack does not move continuously but rather in a somewhat "jerky" manner.

As a concluding remark for this chapter, the crack speed analysis given in this chapter can be used for three major purposes.

- 1) It provides a guide in designing a cleavage specimen for particular fracture tests. Since a number of geometric and material parameters are included in the analysis, one can choose an alternative parameter in achieving a desired crack speed when some of the design parameters are limited for control.
- 2) An estimation of crack speed is possible for a given specimen geometry pulled at constant crosshead speed.
- 3) Conversely, a variable crosshead speed control is possible to achieve a constant crack speed by using the du/da relationship given in equation (3.37).

Achieving a constant crack speed is very important in the study of rate sensitive fracture toughness behavior. By achieving a constant speed, a single value of R can be obtained for the corresponding crack speed (Hardy and Hudson 1973).

CHAPTER IV

TIME-TEMPERATURE DEPENDENT FRACTURE TOUGHNESS OF GLASSY POLYMERS

IV.1 Background

The fracture toughness of glassy polymers is, as other properties, temperature and rate sensitive. The temperature dependent behavior and the rate dependent behavior have been studied separately by several workers. For example, Berry (1963a) and Broutman and McGarry (1965) studied the effect of temperature on "fracture surface energy", γ , of PMMA in tension and cleavage, respectively. Neither author considered the effect of strain rate as a significant variable. They reported the average value of γ , at each temperature for the range of strain rates they employed. Similarly most time dependent fracture toughness tests have been performed at room temperature using the crack speed as a parameter to represent the strain rate; this is demonstrated by the works of Vincent and Gotham (1966), Williams et al (1968) and Marshall et al (1969). Few workers have attempted to examine the variation of fracture toughness where both the temperature and strain-rate vary simultaneously. All of the above authors found increasing K_{IC} values of PMMA as crack speed increases until it suddenly starts to decrease at about 50 mm/s above which no stable cracking was possible. This sudden change in fracture behavior at 50 mm/s was explained in terms of iso-

thermal to adiabatic transition by Williams (1972) and in terms of molecular relaxation transition by Johnson and Radon (1972) This instability condition will be discussed further in the present chapter based on the experimental observations.

Importance of a molecular relaxation mechanism in the fracture process of polymer was emphasized by Boyer (1968) and Heijboer (1968). They investigated the role of the secondary relaxation mechanisms as the source of toughness of glassy polymers below the glass transition temperature T_g . An attempt to correlate the conventional impact tests with 1 kHz dynamic mechanical test results did not prove to be successful (Heijboer 1968). Johnson and Radon (1972) made a similar attempt with K_{IC} test results. They claimed that the K_{IC} value shows a sharp peak at a loading rate equivalent to the frequency at which the damping loss shows a peak in the dynamic mechanical test at the same temperature. Broutman and Kobayashi (1971) reported the variation of fracture surface energy, γ , of PMMA as a function of both temperature and crack speed. They claimed that the primary relaxation mechanism (α -mechanism) prevails in the stable crack growth region and the secondary relaxation mechanism in the unstable fast crack propagation region. Their claim was based on the activation energy obtained from the horizontal shift of the fracture surface energy data. This is contradictory to Boyer's (1968) observation that the stable crack growth is

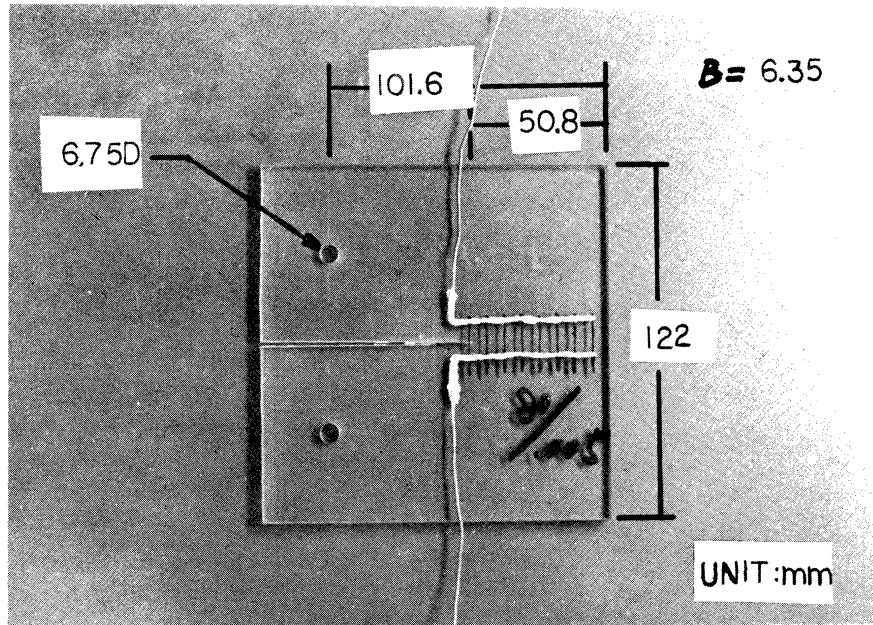
in fact an extension of a craze growth at the advancing crack tip which, in turn, is governed by the secondary relaxation mechanism in PMMA (Boyer 1968). Broutman and Kobayashi obtained the fracture surface energy using the relationship, $G = \frac{1}{2} X^2 \frac{d(u/X)}{Bda}$ and converted it into γ by, $2\gamma = G$. Since the compliance is a function of the rate dependent modulus, they had to make a compliance calibration for each test specimen during the actual tests because compliance changes as a function of temperature and rate of loading. Gurney's method described in II.2 provides a very convenient means of measuring the fracture toughness of rate sensitive material, thus eliminating a tedious procedure of compliance calibration for each test condition. The purpose of the present experiments is to investigate the variation of toughness of two glassy polymers, PMMA and PC, as a function of both temperature and rate of loading. K_{IC} was obtained from the conventional expression available from the fracture mechanics and R was obtained from the load-displacement curve using Gurney's method for obtaining the fracture toughness during the stable crack propagation.

IV.2 Experimental Procedure

IV.2.1 Fracture Specimen Preparation

Commercial grades of 6.35 mm ($\frac{1}{4}$ in) thick PMMA (Plexiglas G) and PC (Lexan) were obtained from a local vendor (Cadillac Plastic Co.). Specimens were machined to

the geometry shown in Figure 16. PMMA specimens were prepared in two steps; first, a starter slot was made along the centerline of the specimen up to $a=44.5 \text{ mm}(1\frac{3}{4} \text{ in})$ by a milling cutter, $63.5 \text{ mm}(2\frac{1}{2} \text{ in})$ in diameter and $0.813 \text{ mm}(0.032 \text{ in})$ thick; the individual teeth were ground to have a 45° inclusive angle. Each specimen was then slowly loaded ($8.33 \text{ } \mu\text{m/s}$) on an Instron machine and when the crack started to increase in length the load was reduced by a quick return travel ($833 \text{ } \mu\text{m/s}$) of the crosshead to prevent the crack from "running away". By repeating this load cycling procedure several times, the crack was extended to a length of $a=50.8 \text{ mm}(2 \text{ in})$. Care had to be taken in machining pin holes. If too fast a cutting speed is used for drilling, the hole becomes tapered along the thickness direction, being wide on the top and narrow on the bottom. This causes an eccentric loading inside the loading pin hole thereby generating a moment at the crack front due to this eccentric loading. These situations are illustrated in Figure 17. Two cases are described: Figure 17a is the case when the taper is in the same direction, and this causes the crack front line to make an angle less than 90° to the side wall surface ($\theta < 90^\circ$). A different case occurs when the two tapers are in the opposite direction, as shown in Figure 17b. The crack front, in this case, splits into several segments, each running at a different elevation, and the overall crack front does not lie in a horizontal plane but makes an angle to the horizon-



a) FRACTURE SPECIMEN

b) SPECIMEN PREPARATION

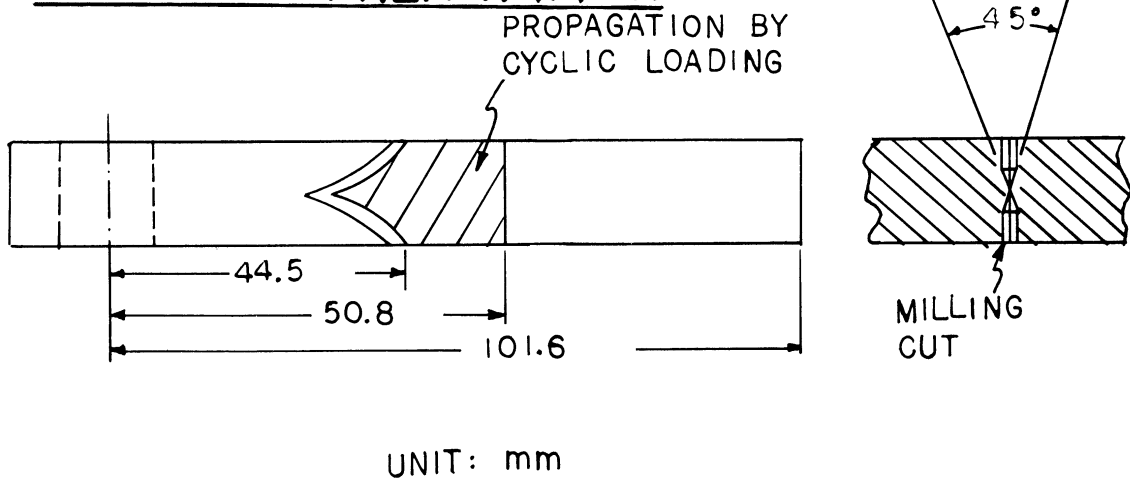
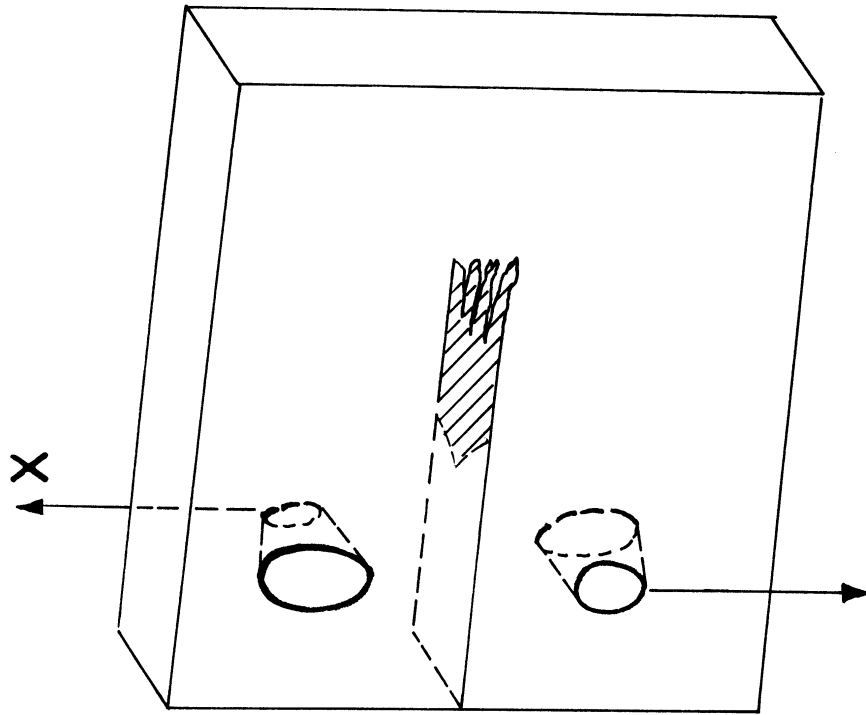
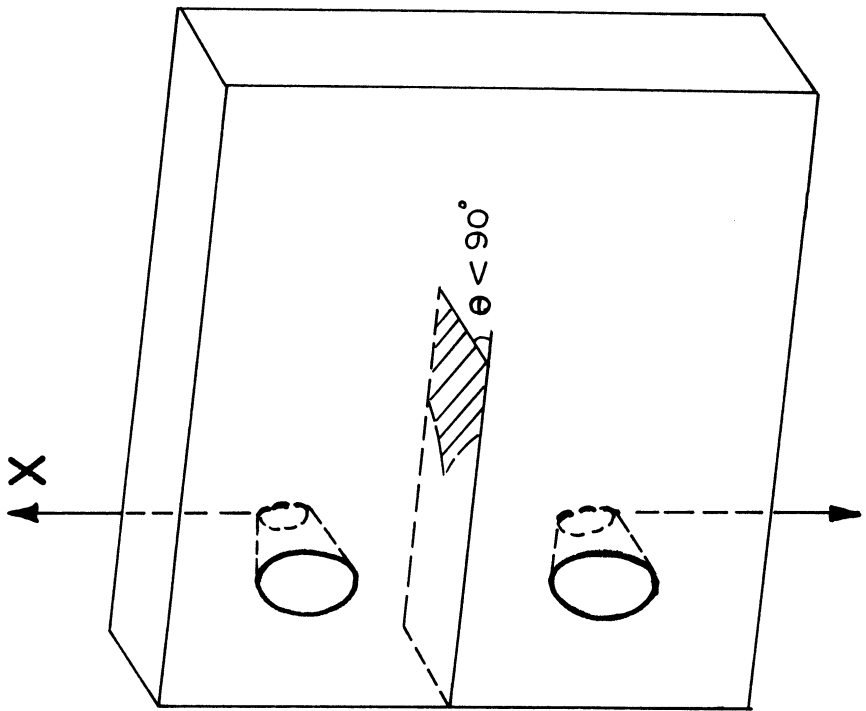


Figure 16. Fracture Specimen used in the present experiment



a) TAPER IN THE SAME DIRECTION



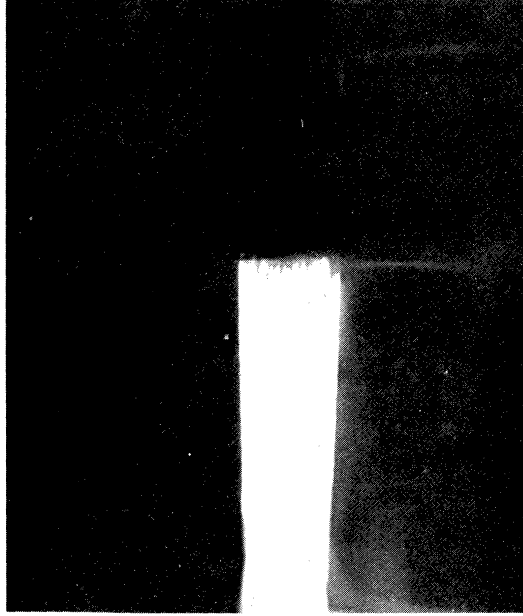
b) TAPER IN OPPOSITE DIRECTION

Figure 17. Eccentric loadings caused by tapered pin holes

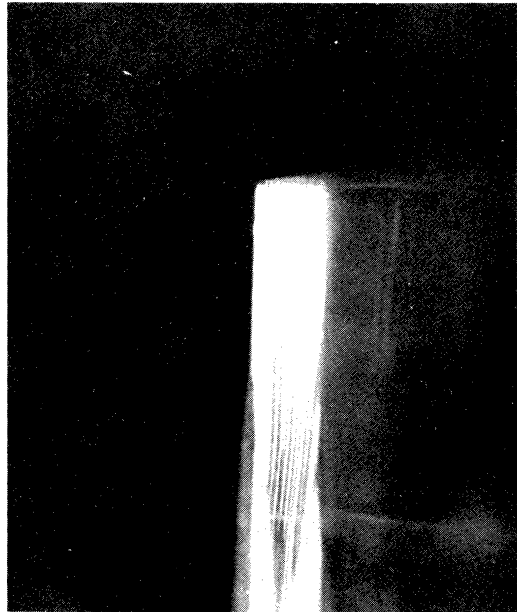
tal plane. When a fracture test is performed with specimens having the "abnormal" crack front shape, shown in Figure 17b, an unusually high load at fracture is achieved compared to that obtained from a 'normal' specimen. This undesirable effect can be avoided by using a lower cutting speed during the drilling operation. A satisfactory result was obtained by using a 78 mm/s (220 rpm with 17/64 in diameter drill) cutting speed. Figure 18 shows examples of "normal" and abnormal crack front shape (only one abnormal case is given here, i.e. the case of Figure 17b). Also important is the good alignment of loading elements including the loading yokes shown in Figure 22. This load-cycling method of generating a natural crack provided less scatter in the experimental fracture toughness data compared to other methods such as saw cuts or razor cuts.

Unfortunately the technique described above could not be applied when preparing PC specimens. When a specimen of this material is slowly loaded on an Instron at room temperature, a plastic zone usually develops before the crack propagation; in a few cases it propagated unstably without forming a plastic zone. It was decided that in preparing the PC fracture specimens, no cyclic loading would be applied to generate a natural crack. Instead, the milling cutter was used exclusively to introduce the initial crack length of $a=50.8$ mm (2 in).

After preparing the PMMA and PC fracture specimens,



Abnormal



Normal

Figure 18. Comparison of normal crack tip shape and abnormal crack tip shape for PMMA

a ladder-like circuit was drawn in the path of the crack using low and high resistance paints purchased from Micro-circuit Co., Inc., New Buffalo, Michigan. In Figure 16a, the dark paint causes high electrical resistance while the resistance of the silvery paint on the sides is negligible. The resistance values can be adjusted by either changing the length or changing the width of the paint brush stroke. As shown in Figure 16 a pair of lead wires was attached at the two terminals of this ladder-like circuit painted on the specimen. Connections were made using tape or conducting glue. A constant voltage was supplied across the circuit and as the crack moved it cut the resistance paint. Each cut caused a step decrease in current output from this circuit since the resistance was changed. This provided a means of measuring the location of the crack tip as a function of time. This information was then used to calculate crack speed and, also, the fracture toughness, R , at the corresponding interval of crack length. The interval between each resistance leg was chosen to be 6.35 mm ($\frac{1}{4}$ in).

This resistant paint technique provides a rather inexpensive means of tracing the crack movement compared to the commercially available "crack propagation measurement gage" available from Micro-measurement Co. Inc., in Detroit, Michigan.

IV.2.2 Temperature Control

Fracture studies were performed on an Instron machine equipped with an environmental chamber (shown in Figure 19), the temperature of which was controlled by a thermostat dial. The operating temperature range for the present study was from 193 °K to 353 °K. Low temperatures were achieved by injection of liquid CO₂ (at 900 psi) through a nozzle, while temperatures above ambient were obtained with an electrical heater. A chamber fan provided good forced convection for fast heat transfer to the test specimen. The actual temperature of the specimen was monitored by a copper-constantan thermocouple which is located near the testpiece, the output being recorded on an x-y-y plotter as a function of time. A fracture test was conducted 10 minutes after the temperature reached a steady state condition shown on the x-y-y plotter.

IV.2.3 General Test Procedure

Figure 20 shows a schematic diagram of the test set-up and Figure 21 shows a picture of the experimental arrangement.

Specimens were pulled by a loading yoke shown in Figure 22, using crosshead speeds that ranged from 0.833 μm/s (0.002 in/min) to 8.33 mm/s (20 in/min). The crack opening displacement at the loading pins was measured by means of an extensometer adapted to a sliding pin assembly as shown in Figure 19 and 20. Signals from the load cell and extensometer were fed into separate channels of a

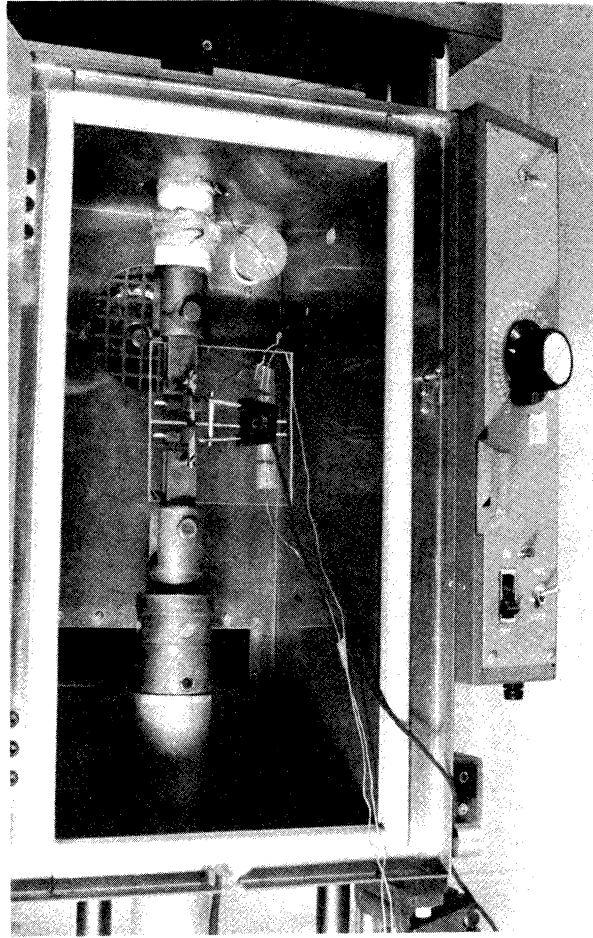


Figure 19. A fracture specimen mounted on an Instron machine equipped with an environmental chamber

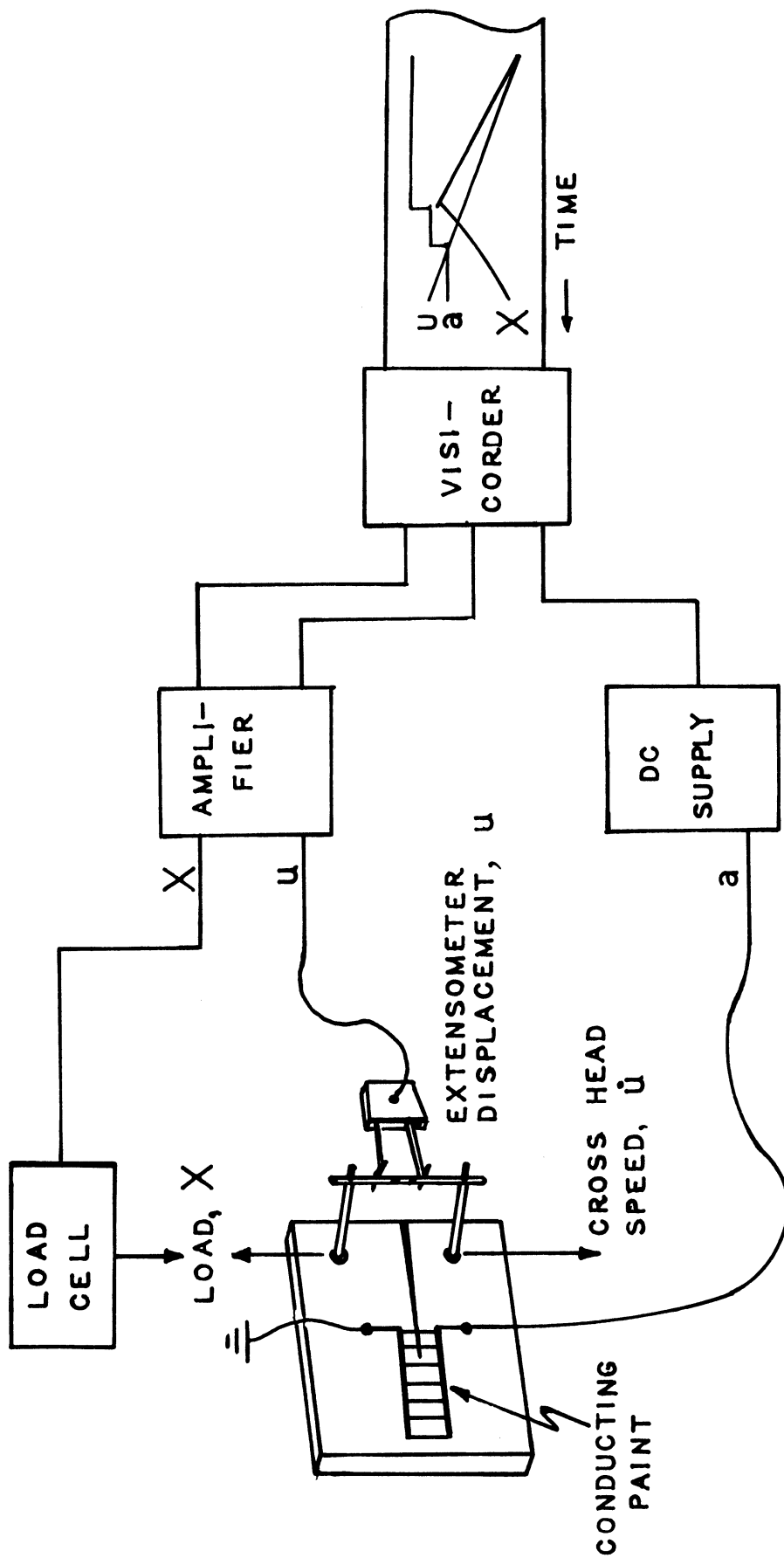
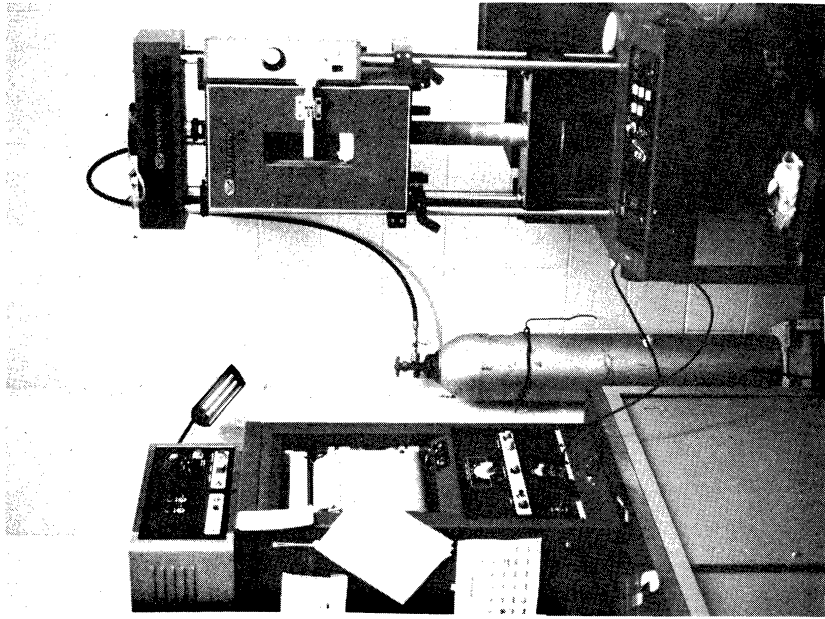


Figure 20. Schematic diagram of fracture test set-up



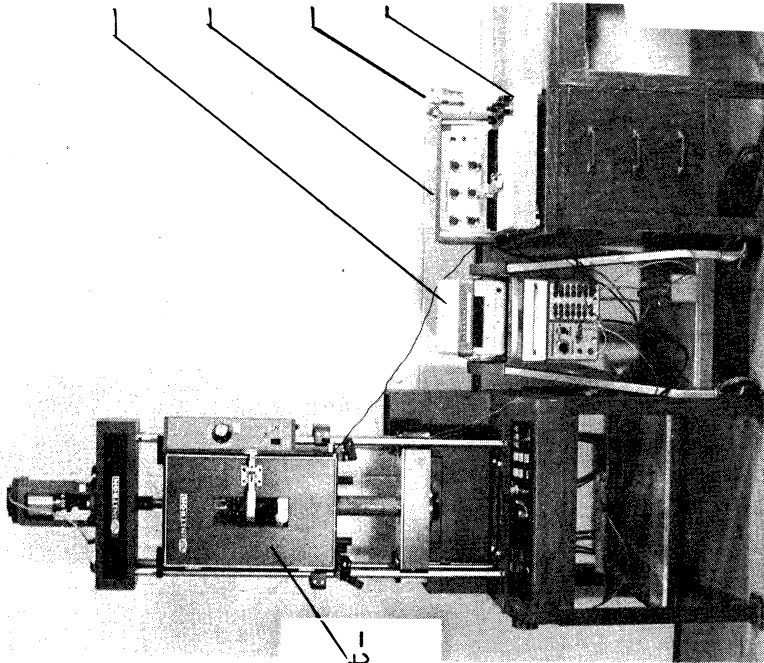
Visicorder

3-Channel
Amplifier

Ice-water

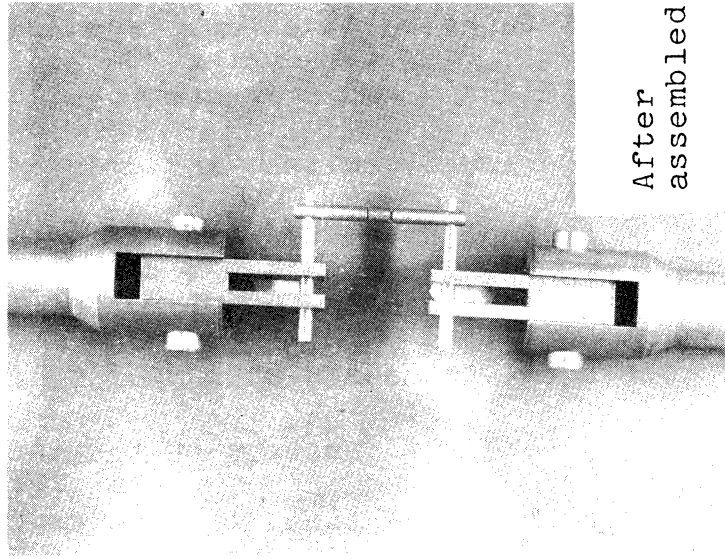
Temperature
Recorder

Liquid CO₂
Supply

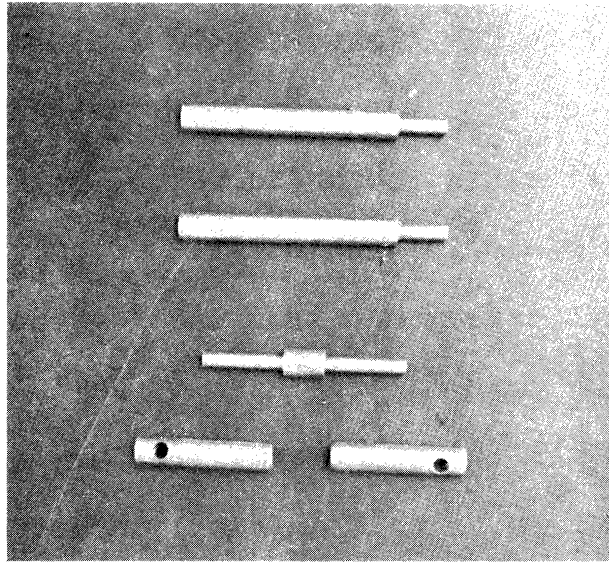


Environment-
al Chamber

Figure 21. Pictures of experimental set-up used in obtaining R and KIC measurements

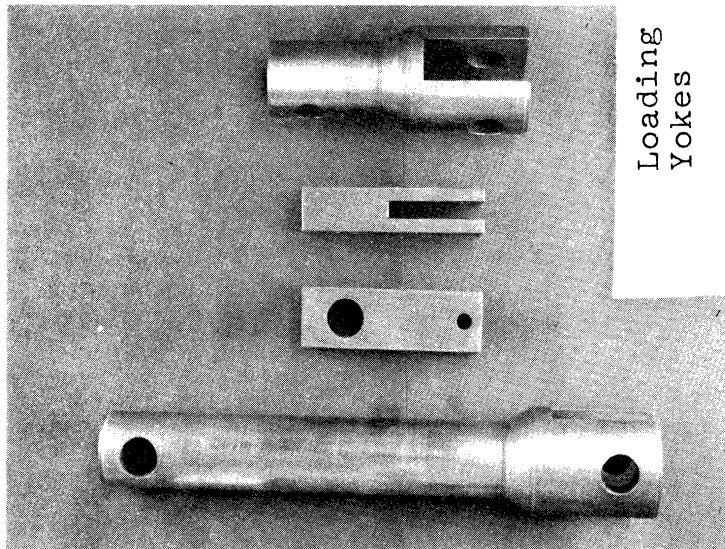


After assembled



Loading Pin

Sliding Pin



Loading Yokes

Figure 22. Loading yokes, loading pins and sliding pin

Visicorder (Honeywell 906C) after being amplified. The signal from the resistance paint circuit was fed directly into the Visicorder without amplification. All three signals were recorded simultaneously on the Visicorder chart paper which moved at a constant speed. A signal fed into each channel of the Visicorder causes the mirror of the galvanometer to rotate and this causes ultraviolet light from a mercury lamp to deflect as a function of the input signal. The trace of this ultraviolet light is recorded on the ultraviolet-light-sensitive chart paper. Crack speed was obtained directly from the chart, and the load-displacement curve (X-u curve) was reconstructed from the chart record, which allowed the fracture toughness value, R , to be measured graphically as described in section II.2 of this dissertation. K_{IC} values were also determined from the load curve by converting either peak loads (in the case of PMMA) or pop-in loads (in the case of PC) to K_{IC} via fracture mechanics K-calibration results available in the literature.

IV.2.4 K calibration

An expression for the stress intensity factor, K , can be obtained from either analytical or experimental methods (refer to section II.3). Both the analytical and experimental K-calibration results are available in the literature for the compact tension specimen used in the present experiment. These K-calibration data were checked by comparing with the experimental K-calibration obtained from the

compliance measurement of the real specimen with varying crack lengths. A series of compliance data was obtained from the PMMA fracture specimens with the geometry shown in Figure 16a except that the starting crack length was a variable. Specimens were pulled at 8.33 $\mu\text{m/s}$ crosshead speed.

Compliance values and the crack lengths are non-dimensionalized by multiplying the compliance value by $\frac{EB}{2}$ and by dividing the crack length by W. Because Young's modulus of PMMA is strain rate and temperature sensitive, the modulus value to be used in non-dimensionalizing the compliance values should be one that was measured at the strain rate equivalent to that employed during the compliance measurement. An analysis of equivalent strain rate for the fracture test is given section IV.4.3. Since the rate and temperature sensitive modulus value is required in the analysis, a series of tensile tests was performed at different strain rates and temperatures as given in Appendix I.

The strain rate expression for the stationary crack is given in section IV.4.3.1 as,

$$\dot{\epsilon} = \frac{e_y}{t_c} = e_y \frac{\dot{u}}{u_c} \quad (4.16)$$

where e_y is the total strain corresponding to the 0.3% offset yield stress obtained from the uniaxial stress-strain curve, t_c is the time measured from the start of load application to the crack initiation, \dot{u} is the crosshead speed and u_c is the critical crack opening displacement at the loading

pins measured at the onset of fracture initiation. The value of u_c is dependent on the initial crack length and for three fracture specimens, was measured to be,

$$\begin{aligned} u_c &= 0.42 \text{ mm} \quad \text{for} \quad a/W = 0.3 \\ u_c &= 0.51 \text{ mm} \quad \text{for} \quad a/W = 0.5 \\ u_c &= 0.74 \text{ mm} \quad \text{for} \quad a/W = 0.7 \end{aligned} \quad (4.1)$$

The crosshead speed used was 8.33 $\mu\text{m/s}$ and e_y was obtained from the uniaxial tensile test at room temperature (Appendix I). The total strain, e_y , corresponding to the 0.3% offset yield stress, remained almost constant at $e_y = 0.020$, regardless of the strain rate involved for PMMA. Thus, using the equation (4.16) already quoted on the previous page,

$$\begin{aligned} \dot{e} &= 3.96 \times 10^{-4} \text{ s}^{-1} \quad \text{for} \quad a/W = 0.3 \\ \dot{e} &= 3.28 \times 10^{-4} \text{ s}^{-1} \quad \text{for} \quad a/W = 0.5 \\ \dot{e} &= 2.25 \times 10^{-4} \text{ s}^{-1} \quad \text{for} \quad a/W = 0.7 \end{aligned} \quad (4.2)$$

The Young's modulus for this range of strain rate is found from Appendix I to be 3.24 GN/m² (470,000psi), and this value together with B=6.35 mm was used in normalizing the experimental compliance data in Figure 23.

The non-dimensionalized experimental compliance data were fitted with a 5th order polynomial in (a/W) by means of a least-squares-best-fit digital program called "MIDAS", available from the Statistical Research Laboratory at the University of Michigan. The resultant curve equation is,

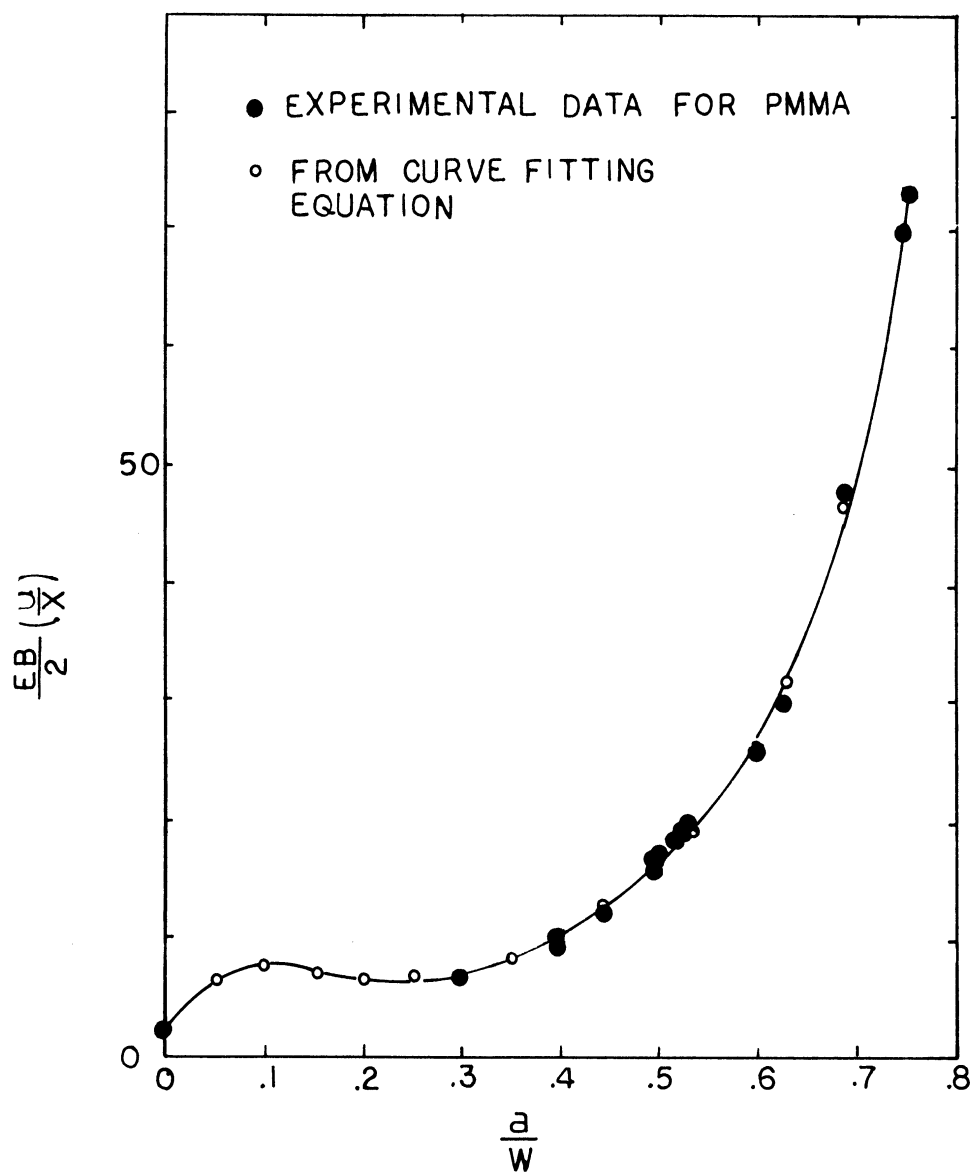


Figure 23. Experimental compliance data and the least-squares best fit curve

$$\begin{aligned} \frac{EB}{2}(u/X) &= 2.4130 + 183.7935(a/W) \\ &- 1595.4725(a/W)^2 + 5599.6385(a/W)^3 \\ &- 8391.2625(a/W)^4 + 4822.4356(a/W)^5 \end{aligned} \quad (4.3)$$

Open circles in Figure 23 are calculated from equation (4.3) while the solid circles are measured values. The curve fitting equation provides a very good fit with the experimental data in the region $0.3 \leq a/W < 0.7$, but it starts to "wiggle" at lower values of (a/W) . and does not represent experimental data for $a/W < 0.3$ consequently, equation (4.3) was considered to describe the experimental compliance data only in the region. $0.3 \leq a/W < 0.7$. Since most of the fracture tests are performed in this range of crack length no efforts have been made to find similar compliance calibration in those range of crack lengths, $a/W < 0.3$ and $a/W > 0.7$. Equation (4.3) was differentiated with respect to (a/W) to obtain experimental $\frac{EB}{2} \frac{d(u/X)}{d(a/W)}$ results, as follows;

$$\begin{aligned} \frac{EB}{2} \frac{d(u/X)}{d(a/W)} &= 183.7935 - 3190.9450(a/W) \\ &+ 16798.9155(a/W)^2 \\ &- 33565.0500(a/W)^3 \\ &+ 24112.1780(a/W)^4 \end{aligned} \quad (4.4)$$

The results of the present compliance calibration result is compared in Table 3 and Figure 24 with the results of other workers obtained from constant Young's modulus

TABLE 3

K-CALIBRATION RESULTS FOR COMPACT
TENSION SPECIMEN BY SEVERAL WORKERS(W/H=1.67)

$\frac{a}{W}$	$\frac{EB}{2} \frac{d(u/X)}{d(a/W)}$			
	Based on constant Young's modulus			Rate dependent Young's modulus
	Srawley and Gross (1972)	Newman (1973)	Srawley et al(1973)	Present Result with PMMA
0.2	20.3	15.4		
0.3	33.3	31.7	33	26.9
0.35			42.6	46.9
0.4	54	53	54.8	63.5
0.45			71.6	78.9
0.5	93	92.8	95.9	98.4
0.55			132.7	131.4
0.6	186	186.2	190.4	190.5
0.65			284.5	292.3
0.7	458.5	465	445.3	456.4
0.8	1680	1690		

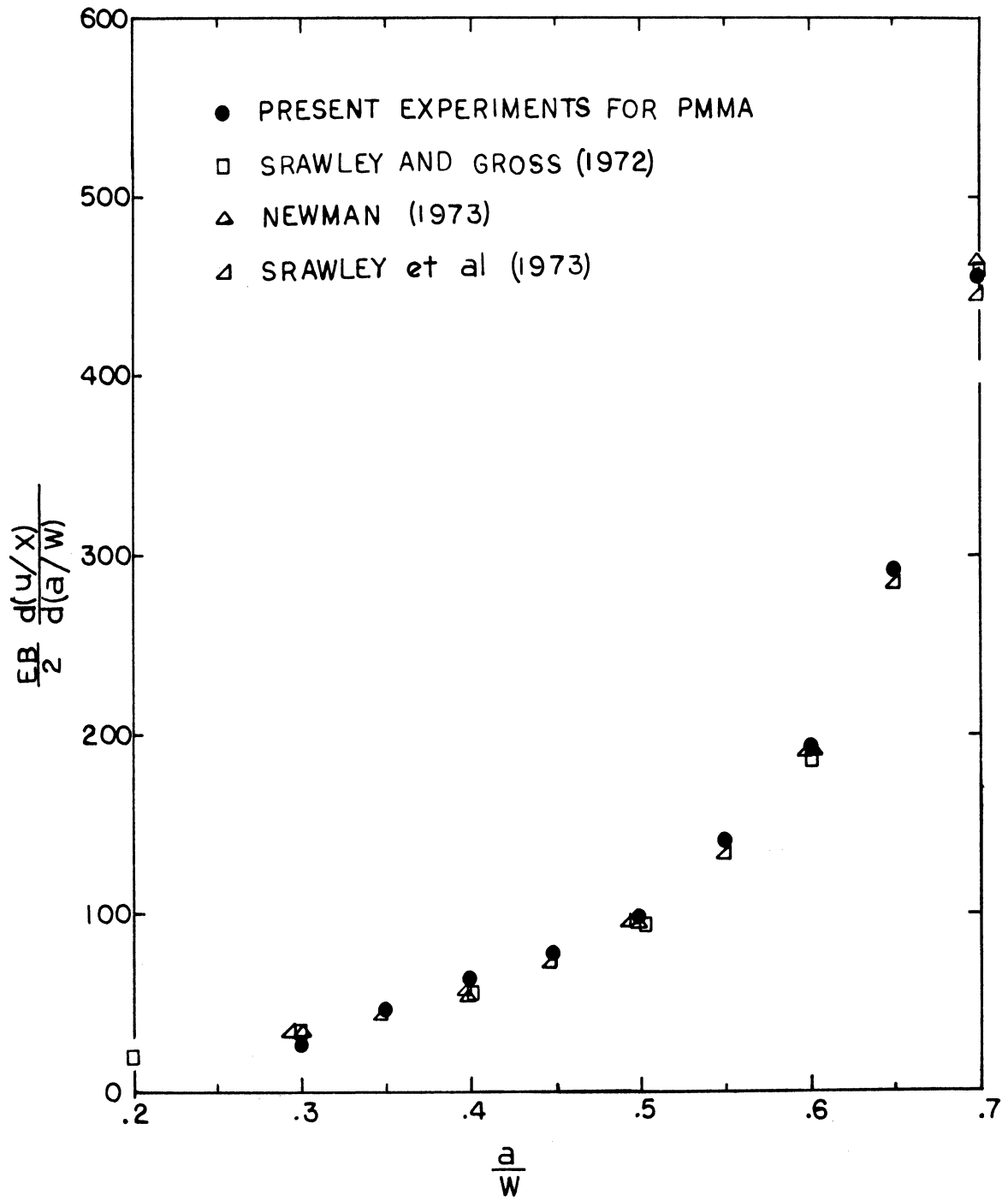


Figure 24. Comparison of K-calibration results by various workers

materials. Since the compliance of a fracture specimen, (u/X) , is inversely proportional to the Young's modulus of the material, the non-dimensionalized compliance parameter $\frac{EB}{2}(u/X)$ will have a property independent of rate dependency because the Young's modulus implicit in (u/X) is eliminated during the non-dimensionalizing procedure. Thus even if a compliance calibration is made with the rate dependent material, such as PMMA, in the non-dimensional compliance parameter, $\frac{EB}{2}(u/X)$, and consequently $\frac{EB}{2} \frac{d(u/X)}{d(a/W)}$, it should produce the same results as those obtained from the rate independent materials. Since there is no explicit expression available relating the compliance and the Young's modulus for compact tension specimen, it is not, in practice, easy to cancel the two rate dependent moduli parameter in the non-dimensional term $\frac{EB}{2}(u/X)$. An alternative method is to estimate the equivalent strain rate involved in the compliance measurement procedure and find the corresponding Young's modulus from the uniaxial tensile test result at the same strain rate. When the compliance calibration results from a rate sensitive material are compared with those from the rate independent material in Table 3, they are in reasonable agreement, thereby supporting the above argument that the same K-calibration result is applicable for both rate dependent and rate independent materials.

Since the result from equation (4.4) depends on the choice of a modulus value corresponding to the equivalent strain rates involved in the compliance measurements, the

good agreement of the present results with other results obtained from less strain rate sensitive material supports the validity of the equivalent strain rate expression used for the stationary crack; this will be discussed further in section IV.4.3. The numerical results of K-calibration given by Srawley et al (1973) will be adopted in the present study in calculating the K_{IC} values. They are chosen in preference to the present experimental K-calibration results from PMMA on two grounds; first, the two results are expected to be the same and second, the estimated equivalent modulus value used in the present K-calibration would involve more errors than the modulus value from the rate independent materials.

Thus, based on the K-calibration results of Srawley et al (1973),

$$\frac{EB}{2} \frac{d(u/X)}{d(a/W)} = 95.9 \quad (4.5)$$

for $a/W=0.5$, which is the crack length to be used in the present experiment. Using the relationship given in equation (2.19b),

$$\frac{K^2 B^2 W}{X} = \frac{EB}{2} \frac{d(u/X)}{d(a/W)} = 95.9 \quad (4.6a)$$

or

$$\frac{KBW^{1/2}}{X} = 9.79 \quad (4.6b)$$

Thus the critical stress intensity factor K_{IC} can

be calculated from equation (4.6) by introducing the geometrical dimensions B, W and the critical load value, X_c at which the crack starts to extend.

PMMA specimens start initial fracture near the maximum load in the load-displacement curve as illustrated in Figure 25a. In the case of PC, however, fracture initiates when the load-displacement curve shows a 'pop-in' mark, this is shown where the load-displacement curve exhibits a sudden change in slope as shown in Figure 25b. As the loading pin is pulled further, the load increases again and a large plastic yielding zone develops in front of the crack tip. The load starts to decrease as the crack, accompanied by a large plastic yield zone of roughly 6 mm radius, starts to move.

In applying the load values in equation (4.6b) to determine K_{IC} , the maximum load was used for PMMA and pop-in load for PC.

IV.3 Experimental Results

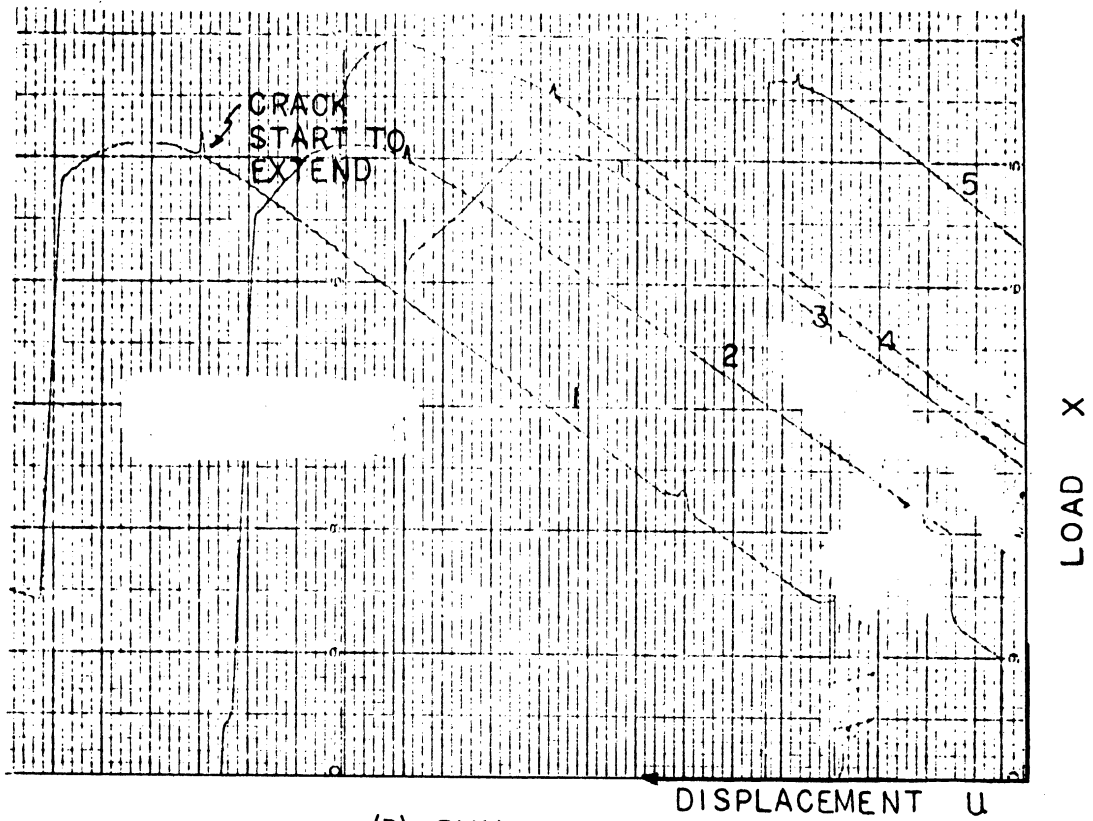
IV.3.1 PMMA

IV.3.1.1 K_{IC} results

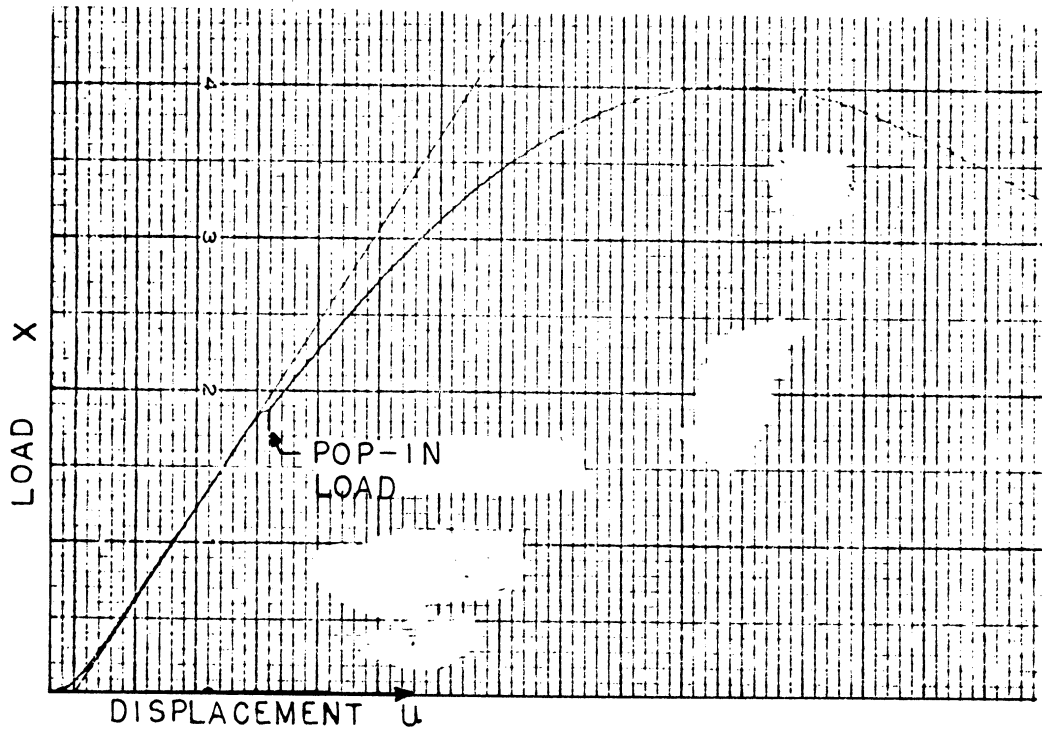
The experimental K_{IC} results obtained at temperatures ranging from 193 °K to 353 °K, and the crosshead speeds ranging from 0.833 $\mu\text{m/s}$ to 8.330 mm/s are shown in Figure 26.

A single specimen geometry was used throughout the experiment in order to avoid the probable effects of geometry.

K_{IC} values were calculated from equation (4.6b) and individual values are tabulated in Table 4.

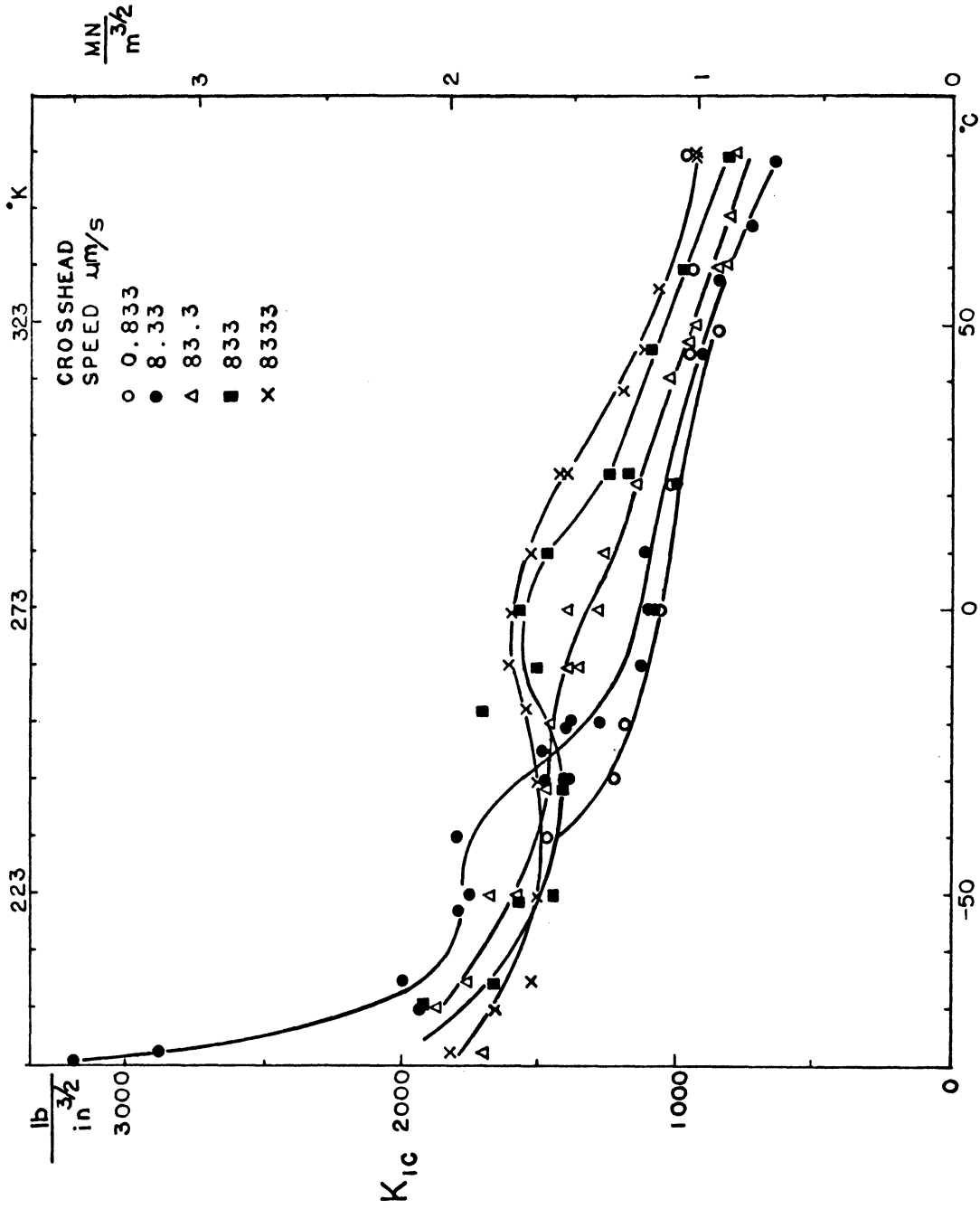


(a) PMMA



(b) PC

Figure 25. Typical load-displacement curve from PMMA and PC fracture tests from Instron chart



TEMPERATURE

Figure 26. K_{Ic} results of PMMA as a function of temperature and crosshead speed

TABLE 4
EXPERIMENTAL RESULTS OF K_{IC} OF PMMA

Crosshead Speed ($\mu\text{m/s}$)	Temperature ($^{\circ}\text{K}$)	Thickness (mm)	Maximum Load (N)	K_{IC} $\frac{3}{2}$ (MN/m^2)
0.833	233	5.89	311	1.62
	243	5.69	249	1.34
	253	5.62	240	1.31
	273	5.71	216	1.17
	296	6.06	213	1.08
	318	5.62	190	1.04
	322	5.66	171	0.93
	333	5.83	196	1.03
	353	5.85	203	1.08
	8.33	193	6.22	713
195		5.85	600	3.15
203		6.42	445	2.12
207		6.35	453	2.18
220		5.97	382	1.96
223		5.82	364	1.92
233		5.78	373	1.97
243		5.77	311	1.62
243		6.28	311	1.52
243		5.80	292	1.54
248		6.07	324	1.63
252		6.30	315	1.53
253		6.02	276	1.40

TABLE 4 (CONTINUED)

Crosshead Speed ($\mu\text{m/s}$)	Temperature ($^{\circ}\text{K}$)	Thickness (mm)	Maximum Load (N)	K_{IC} ($\text{MN/m}^{3/2}$)
8.33	253	5.78	284	1.51
	263	6.05	245	1.24
	273	6.30	241	1.17
	273	6.10	238	1.19
	283	6.05	242	1.22
	296	6.16	220	1.09
	317	6.10	198	1.00
	331	6.07	184	0.93
	341	6.40	169	0.81
	352	6.07	142	0.71
	83.3	195	5.85	356
203		6.43	431	2.05
207		6.20	389	1.92
223		5.99	360	1.84
223		5.89	333	1.73
243		6.06	320	1.62
253		5.84	304	1.60
263		5.81	289	1.53
263		6.05	292	1.48
273		6.10	280	1.40
273		6.29	316	1.54
283		6.12	276	1.38
296		6.07	249	1.25
314		6.02	221	1.12

TABLE 4 (CONTINUED)

Crosshead Speed ($\mu\text{m/s}$)	Temperature ($^{\circ}\text{K}$)	Thickness (mm)	Maximum Load (N)	K_{IC} ($\text{MN/m}^{3/2}$)
83.3	320	5.69	196	1.05
	323	6.00	199	1.02
	333	5.87	176	0.92
	334	6.10	180	0.90
	343	6.40	183	0.88
	353	5.90	162	0.84
	833	203	6.10	422
107		5.96	356	1.83
123		6.09	311	1.59
123		5.89	333	1.73
143		6.01	302	1.54
255		6.28	382	1.87
263		5.95	320	1.65
273		6.05	338	1.72
283		6.17	324	1.61
296		6.45	287	1.37
296		5.82	244	1.29
319		6.33	249	1.20
333		6.18	216	1.07
353		6.07	174	0.88
8,330		195	6.01	386
	203	5.96	356	1.83

TABLE 4 (CONTINUED)

Crosshead Speed ($\mu\text{m/s}$)	Temperature ($^{\circ}\text{K}$)	Thickness (mm)	Maximum Load (N)	K_{IC} ($\text{MN/m}^{\frac{3}{2}}$)
8,330	208	5.89	322	1.68
	223	5.74	311	1.66
	243	5.76	313	1.67
	255	5.93	329	1.70
	263	6.16	350	1.77
	273	6.08	346	1.75
	283	6.05	333	1.69
	296	6.00	298	1.52
	296	6.10	311	1.56
	311	6.07	261	1.31
	319	6.07	244	1.23
	329	6.05	231	1.17
	353	5.97	201	1.03
	353	6.07	201	1.02

IV.3.1.2 Experimental Results of R

The fracture toughness value, R , of PMMA was measured as a function of both temperature and crack speed. The experimental results of fracture toughness, R , were obtained graphically from an $X-u$ plot reconstructed from the Visicorder chart paper where X , u and ' a ' values are recorded during the crack propagation as a function of time. Figure 27 shows a typical Visicorder record of X , u and ' a ' as the chart moves at a constant speed. This information is replotted in the $X-u$ graph shown in Figure 28 where each sector area corresponds to 6.35 mm of crack propagation. Graphical measurement, by means of a planimeter, led to the R values shown. The crack speed changes significantly as the crack moves from starting position to the end of the specimen (this is predicted from the crack speed analysis in section II.3.1). Consequently, the rate dependent R values determined from the region of crack initiation may differ from those measured near the end of the test. The crack speed can be easily obtained from the Visicorder chart paper since each signal from the resistance paint circuit on the specimen causes a stepwise signal as the advancing crack cuts each leg of the ladder-like circuit. The fracture toughness values, R , obtained at various temperature, are plotted against crack speed in Figure 29 through 37. Series of fracture surfaces are included in each figure to show effect of temperature and crack speed on the resulting fracture surfaces. Further discussion will be given on this subject in Chapter V. All data points were obtained from

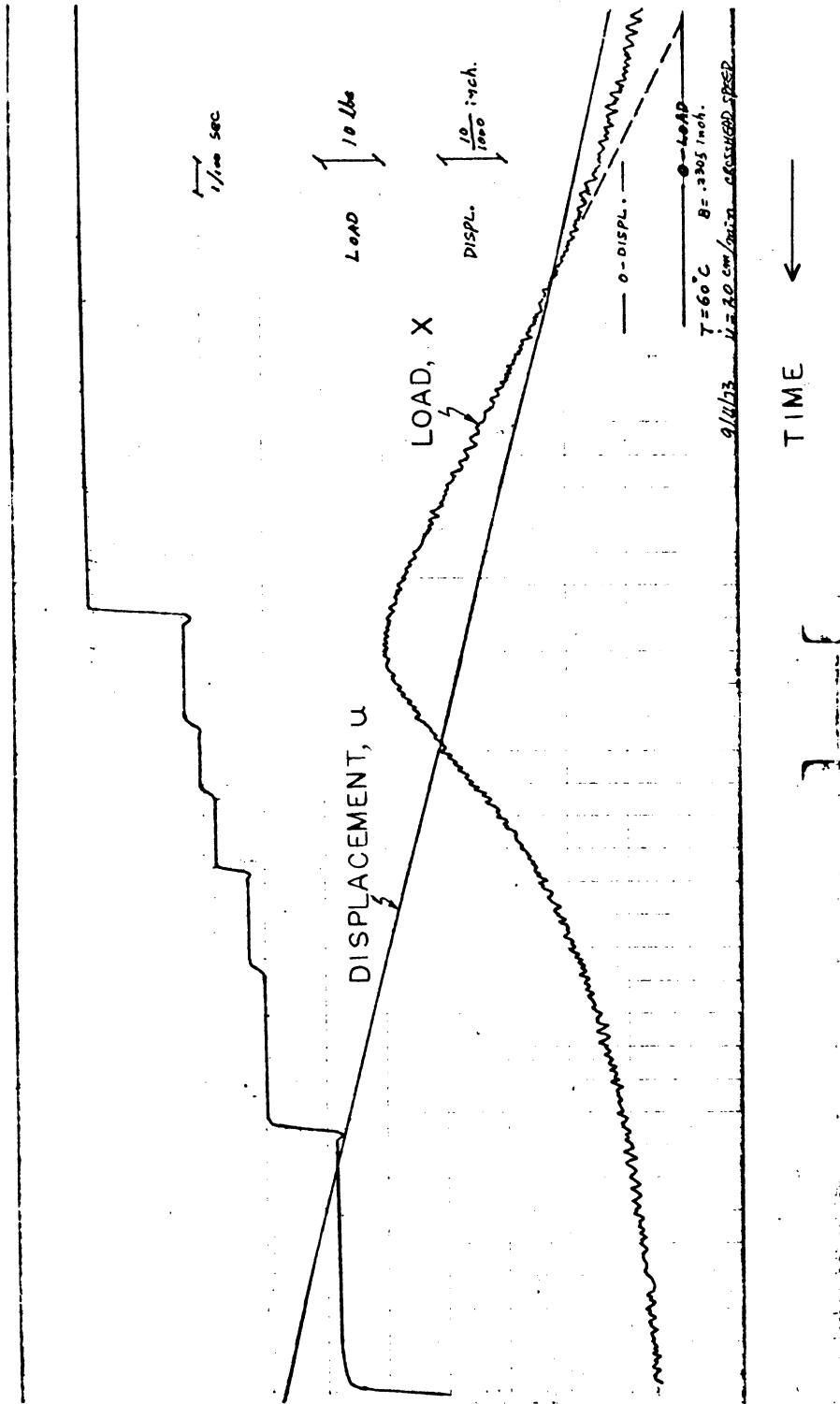


Figure 27. A typical Visicorder record showing X, u and 'a' as function of time

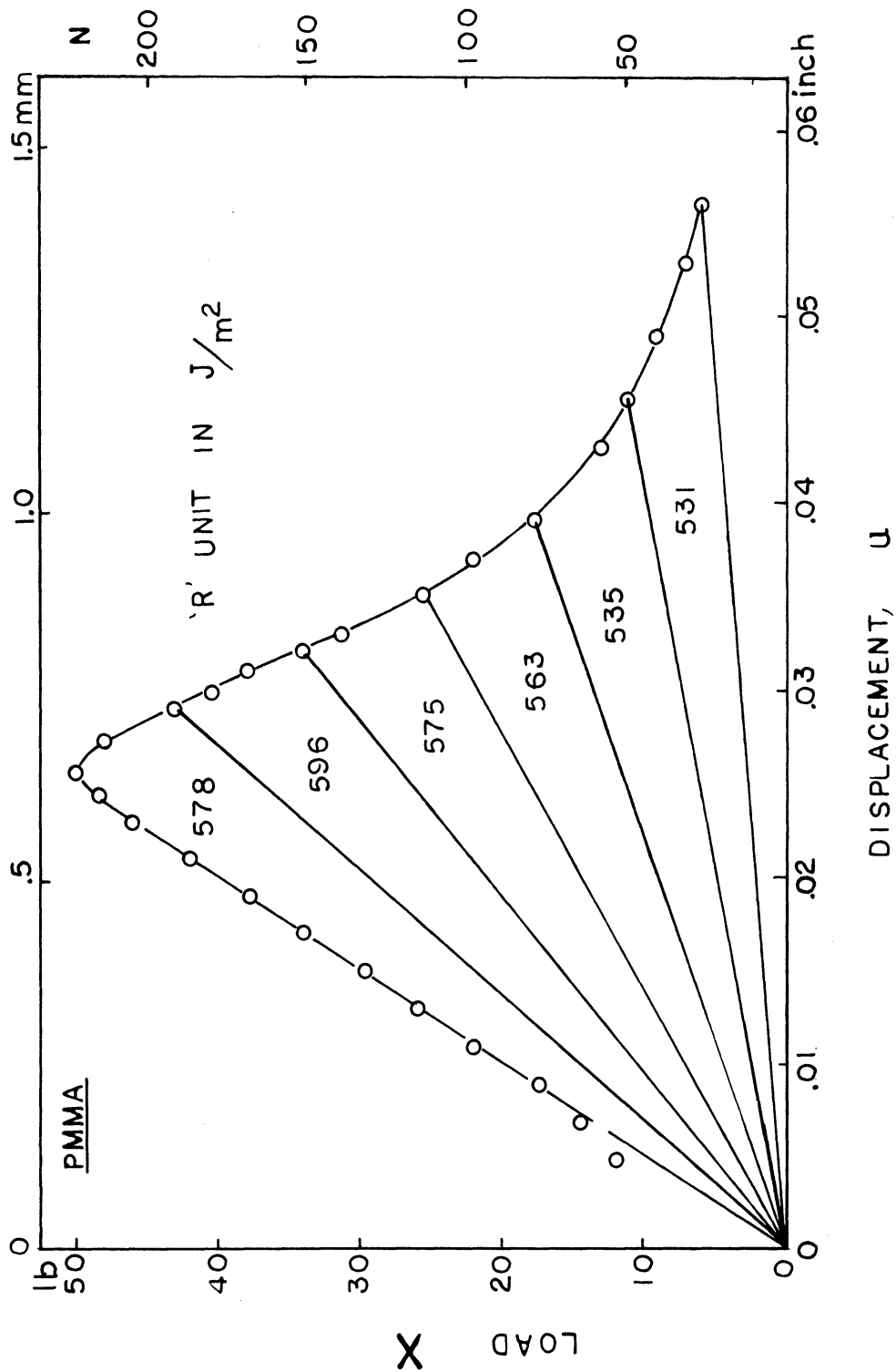


Figure 28. X-u plot reconstructed from the data in Figure 27. Each sector area corresponds to crack extension of 6.35 mm

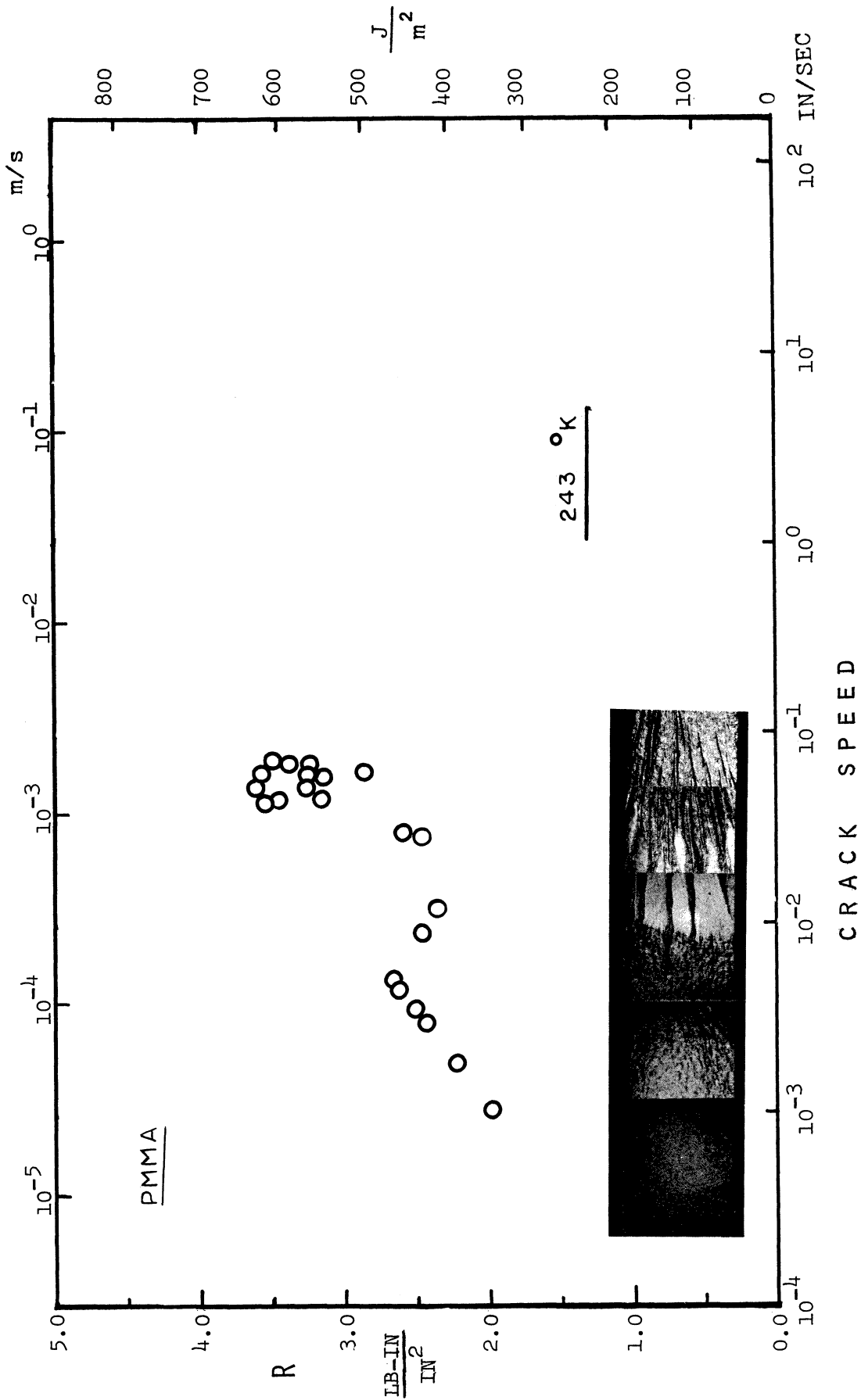


Figure 29. Fracture toughness, R, as a function of crack speed, at 243 °K

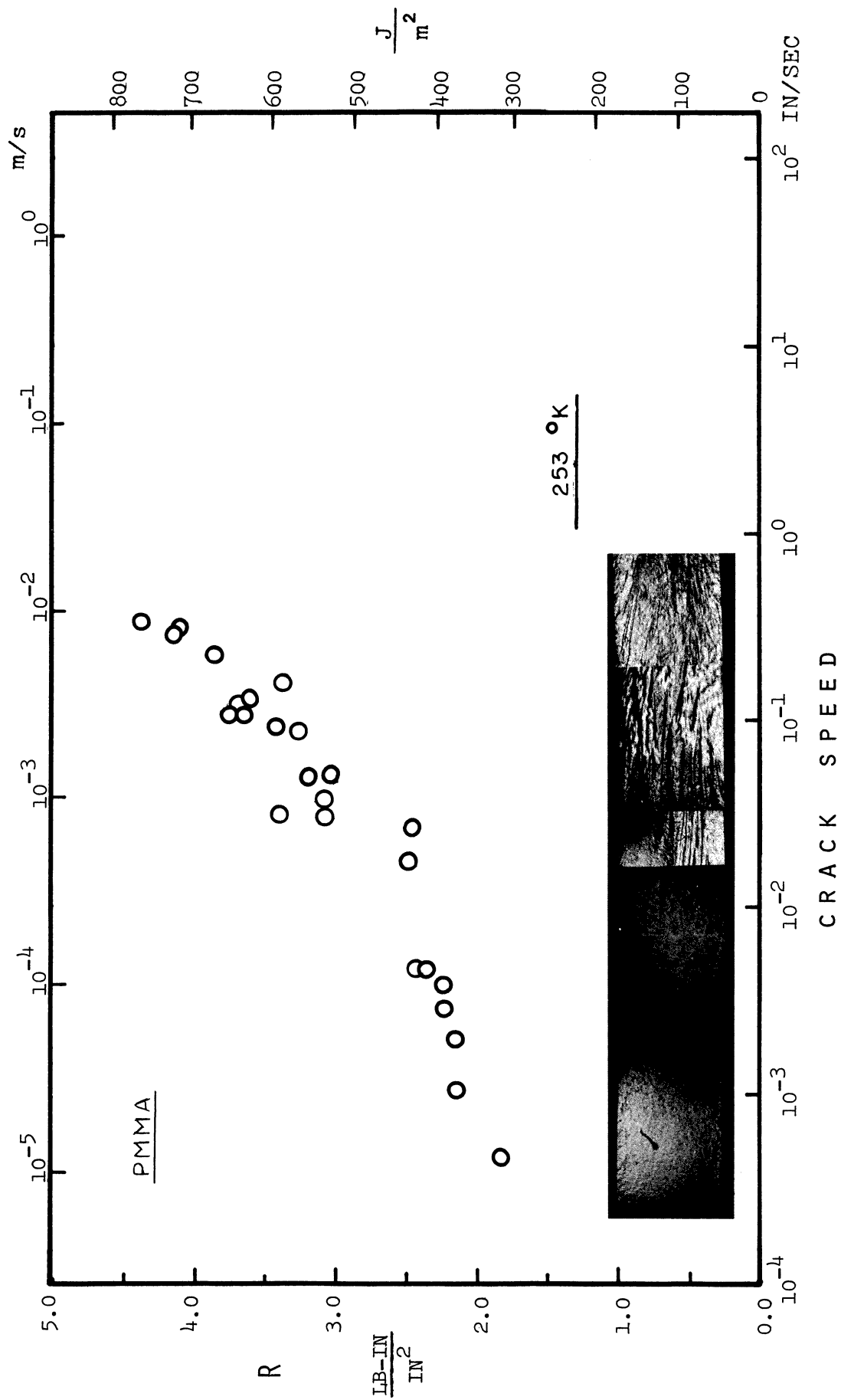


Figure 30. Fracture toughness, R, as a function of crack speed, at 253 °K

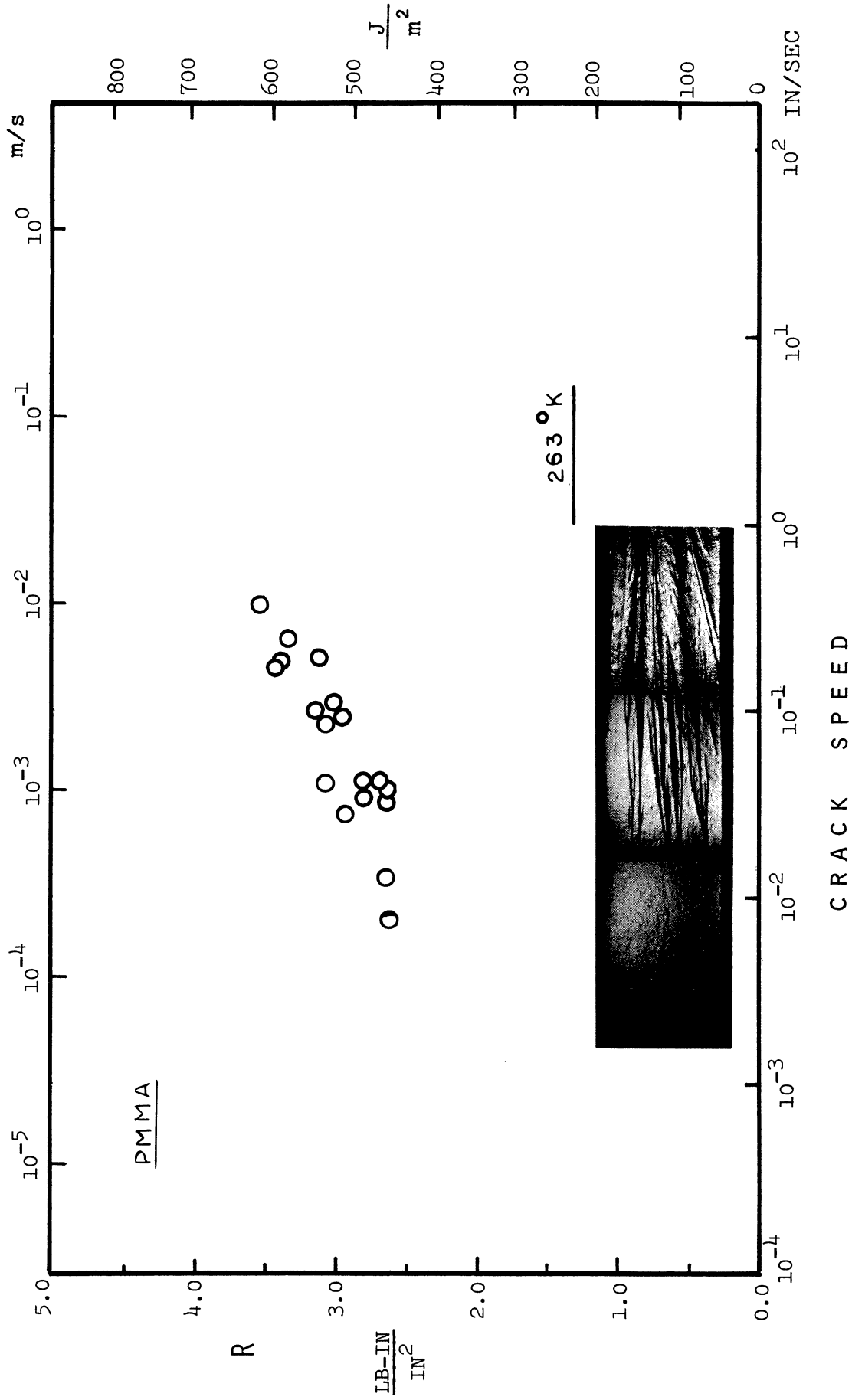


Figure 31. Fracture toughness, R , as a function of crack speed, at 263 °K

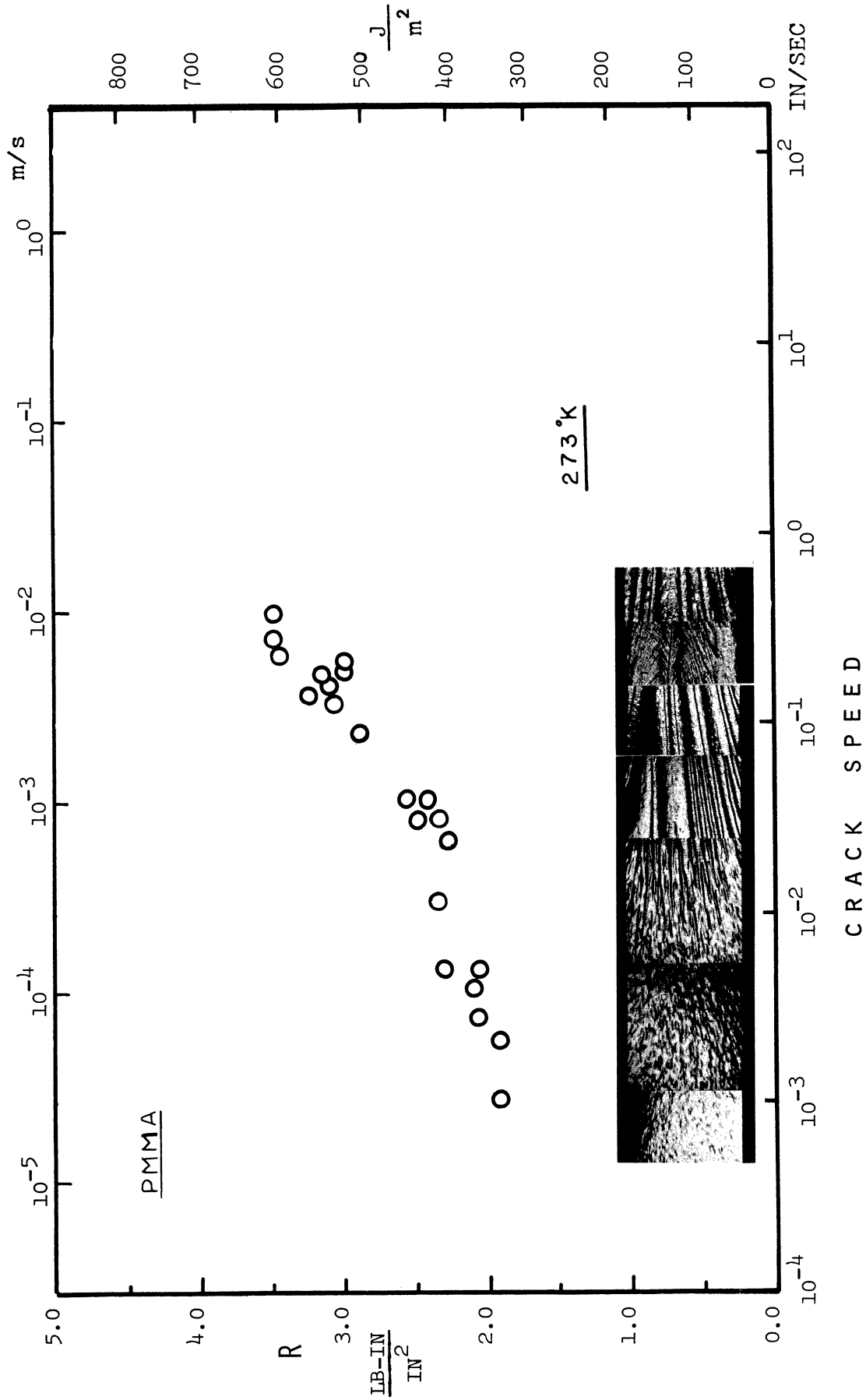


Figure 32. Fracture toughness, R, as a function of crack speed, at 273 °K

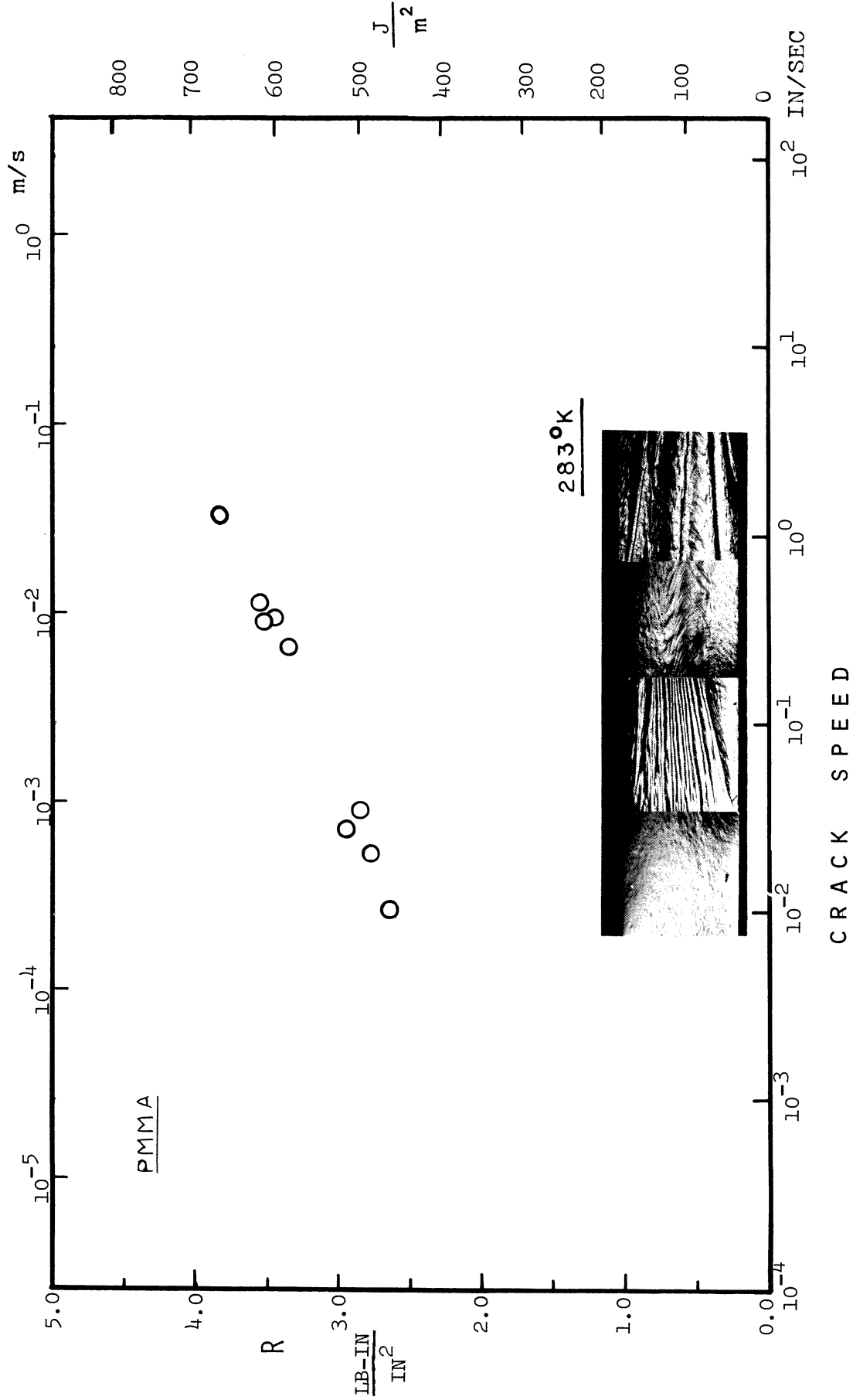


Figure 33. Fracture toughness, R , as a function of crack speed, at 283 °K

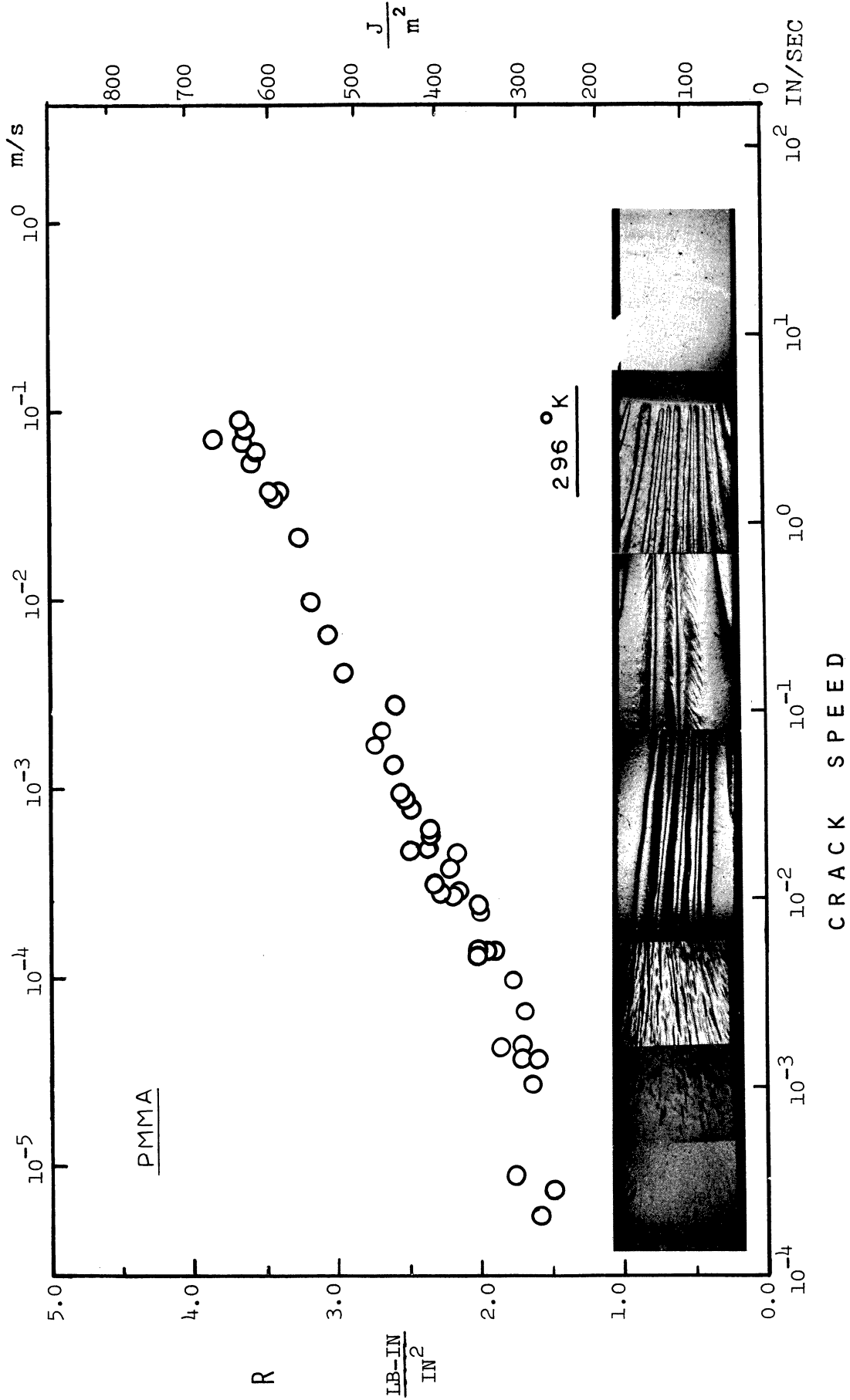


Figure 34. Fracture toughness, R, as a function of crack speed, at 296 °K

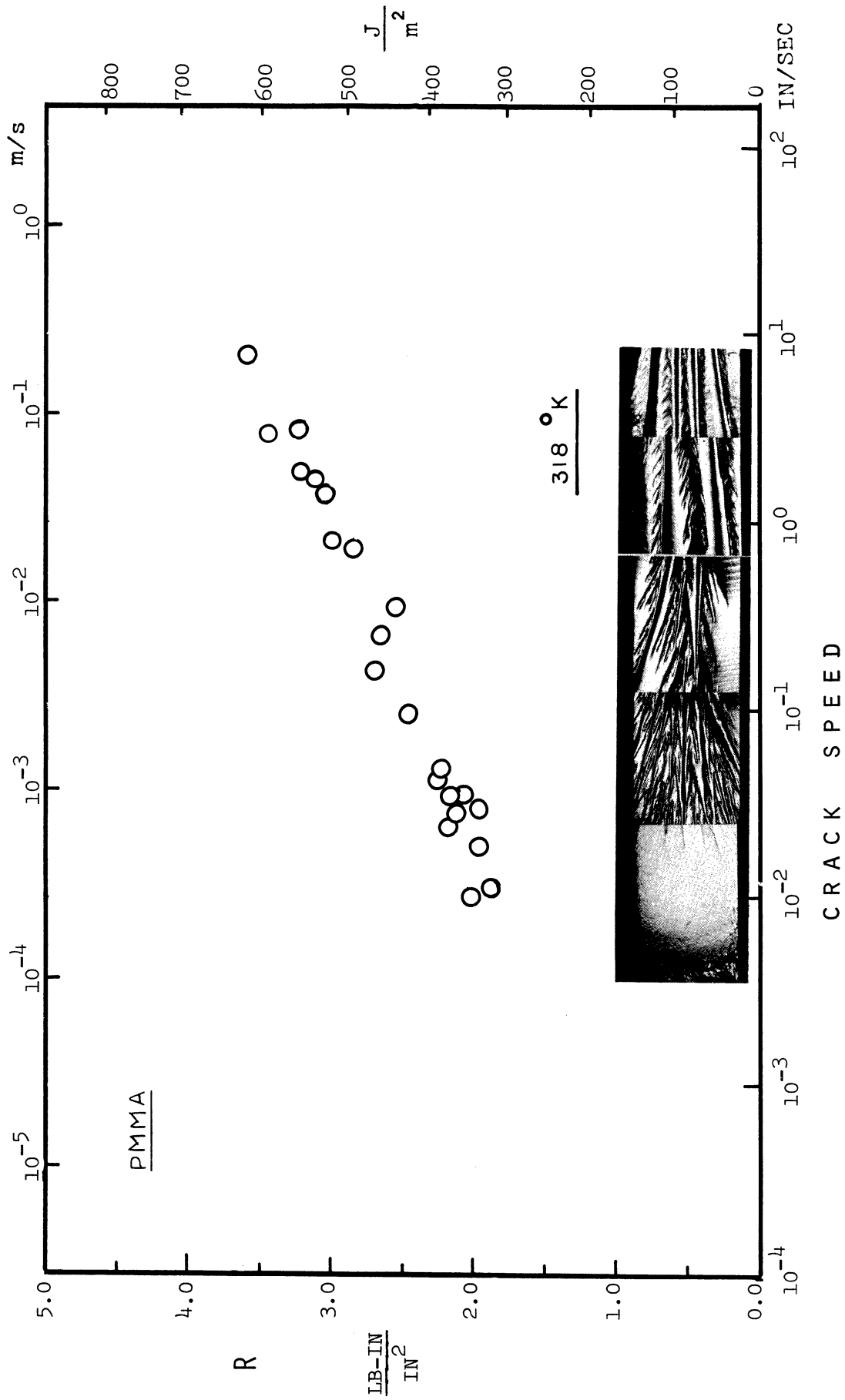


Figure 35. Fracture toughness, R , as a function of crack speed, at 318 °K

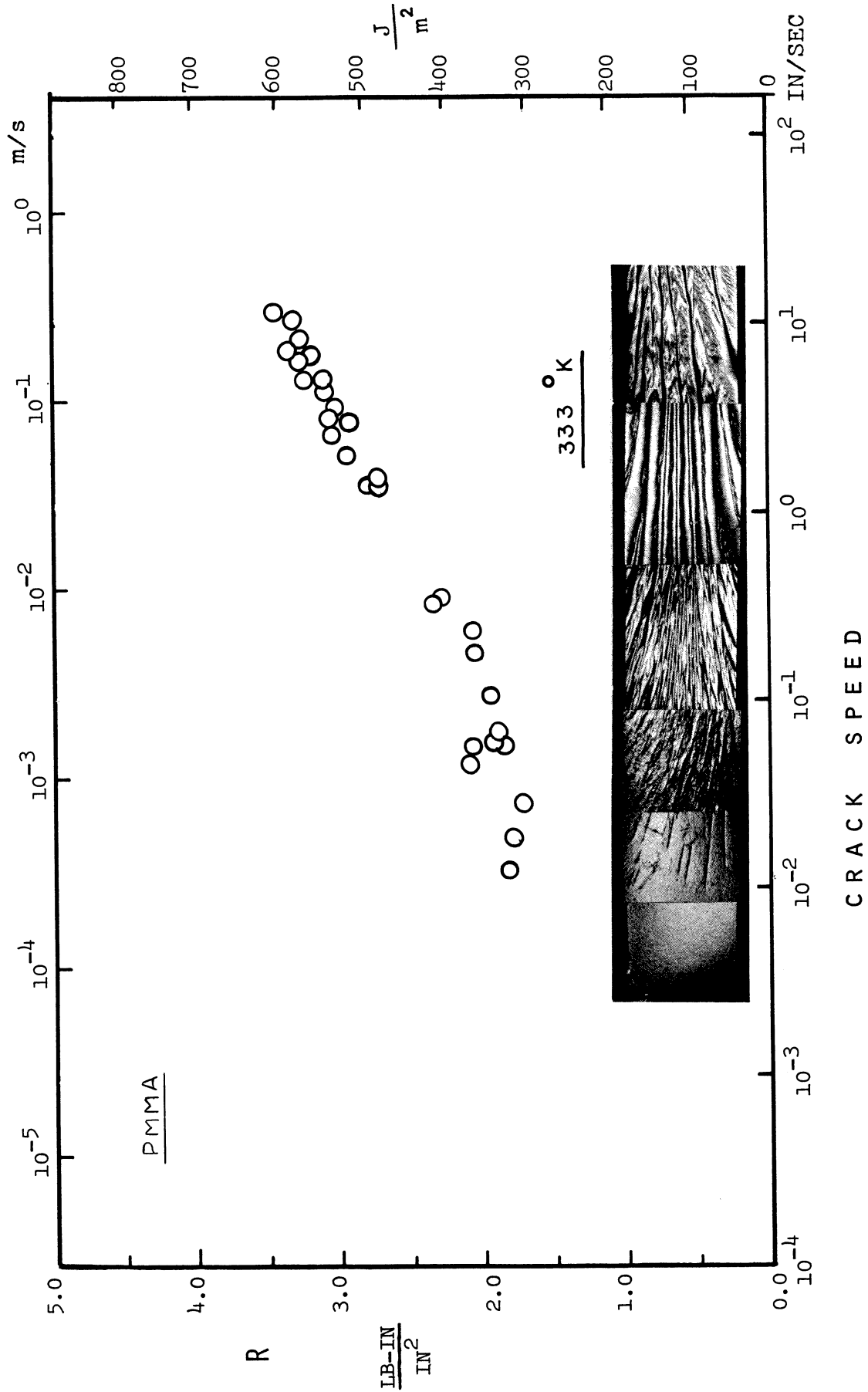


Figure 36. Fracture toughness, R , as a function of crack speed, at 333 °K

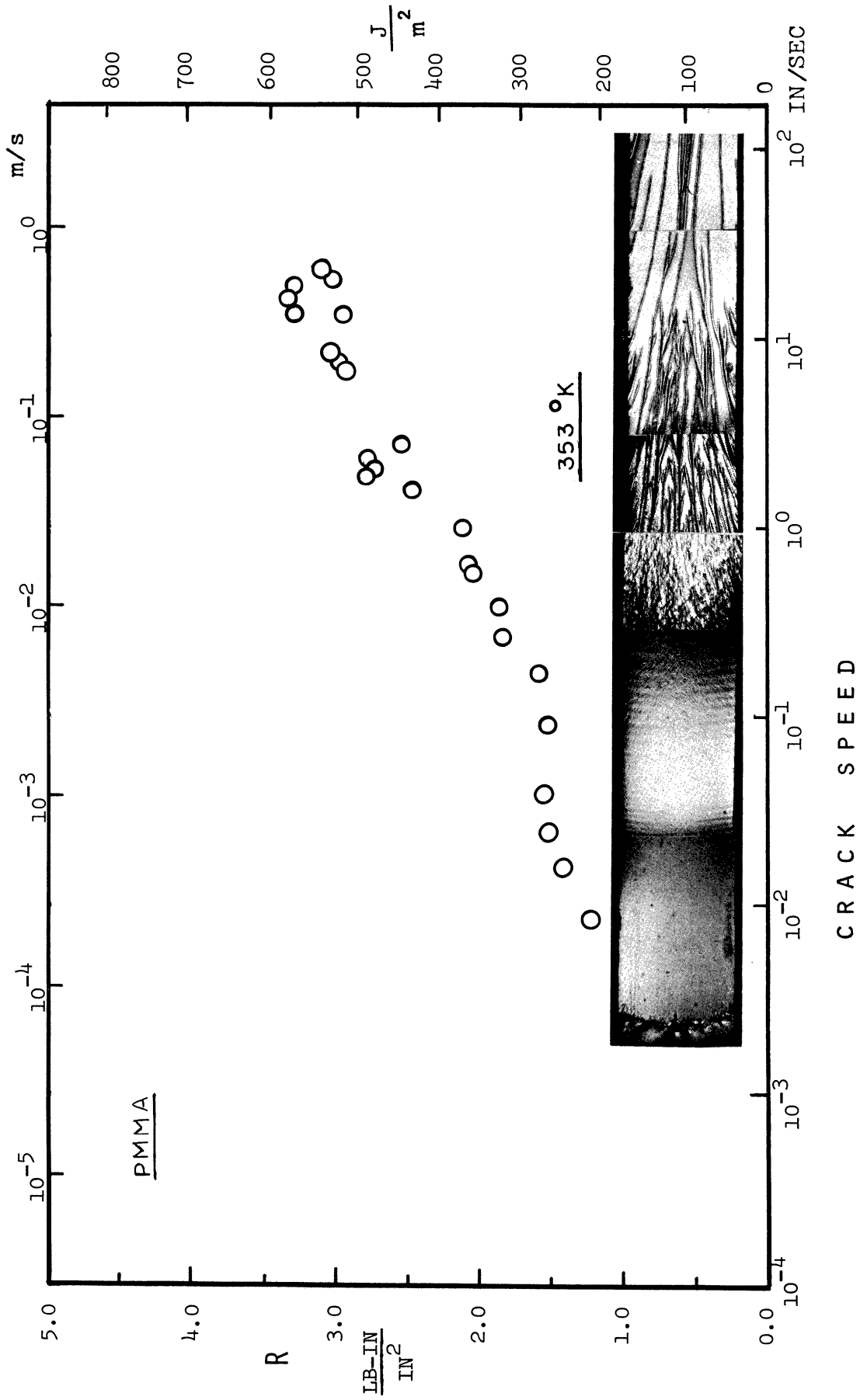


Figure 37. Fracture toughness, R , as a function of crack speed, at 353 °K

experiments with stable crack propagation. The lower limit, in each graph, corresponds to the lowest crack speed attainable with the present specimen pulled at the slowest cross-head speed (0.833 $\mu\text{m/s}$). As the crack speed increases, the fracture toughness, R , increases at every temperature, with different rates of increase. As the crack speed increased further, an upper limit was eventually reached above which no stable crack growth was attainable. This upper limit crack speed varied as a function of temperature, having generally lower values at lower temperatures.

The speed of the unstable crack cannot be measured with the Visicorder because crack speed is too fast compared to the response time of the Visicorder. A simple test to determine the crack speed in the unstable region was done by feeding the signal from the resistance paint circuit shown in Figure 16 into an oscilloscope instead of a Visicorder. Figure 38 is the picture taken from the oscilloscope during the fracture test of a PMMA test specimen pulled at the fastest crosshead speed (16.7 mm/s) at room temperature. The stepwise signal is from the resistance paint circuit on the specimen and each step decrease corresponds to a 6.35 mm ($\frac{1}{4}$ in) crack movement. The other trace records the load and it is interesting to note that the load remained constant while the crack has already propagated towards the end of the specimen, suggesting inertia effects. The estimated crack speed was about 230 m/s at room temperature (This about 0.2 times the transverse wave velocity in PMMA at room temperature.

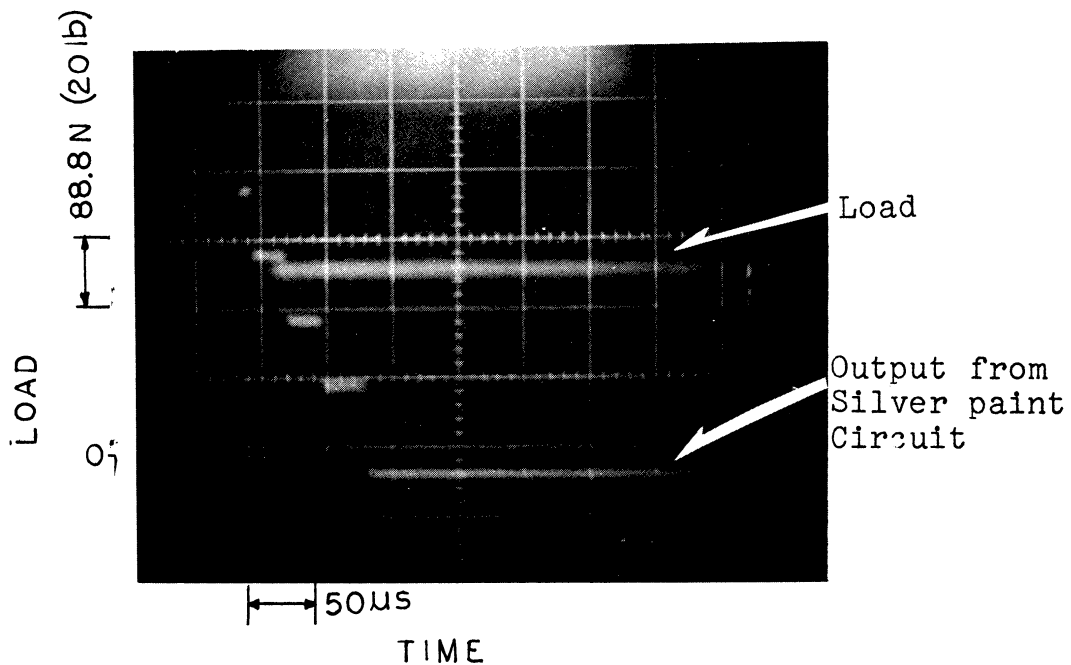
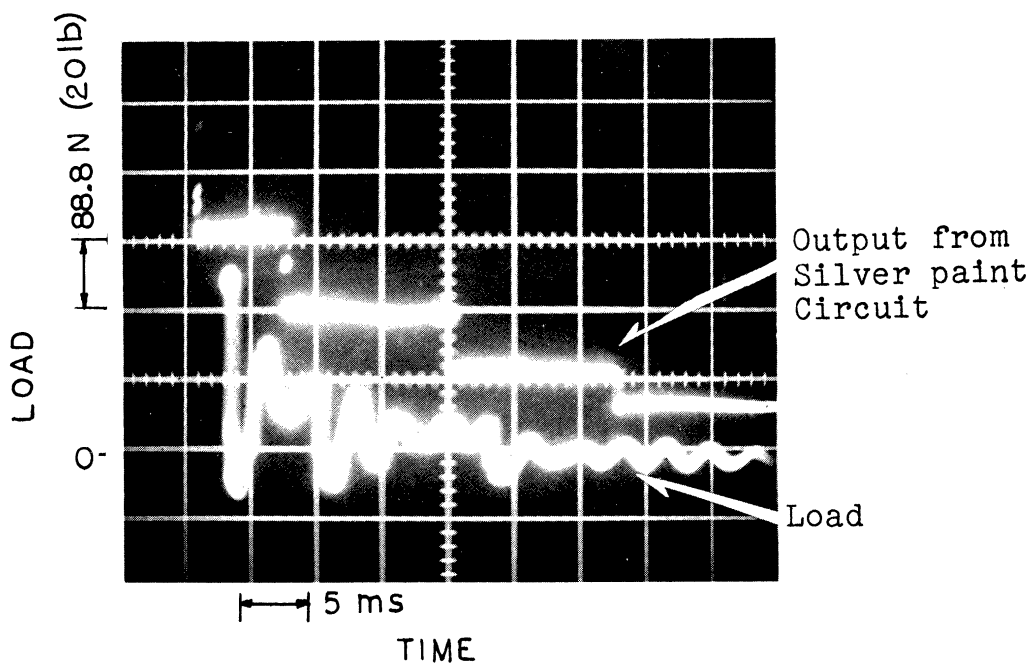


Figure 38. Picture of the oscilloscope trace during unstable crack propagation. Bottom photograph shows an expanded time scale of the initial region of the top photograph

As the testing temperature was lowered, stable crack propagation was achieved in a more limited range of crack speed, and when the temperature reached 233 °K no stable crack growth was possible even at such a slow crosshead speed as 0.833 $\mu\text{m/s}$. Absence of fracture toughness data below 243 °K implies that stable crack growth was not attainable at these temperatures. It should also be noted that when the temperature was increased to 353 °K the crack would not start when the specimen was pulled at the slowest crosshead speed (0.833 $\mu\text{m/s}$). Instead, a plastic zone developed around the starting crack front. Severe craze marks gave bright reflections of light with the highest concentration of crazes being formed along the $\sim 45^\circ$ line on both sides of the horizontal axis. As the specimen was pulled at higher crosshead speeds, this plastic zone formation was suppressed and the crack propagated stably even at such high crack speeds ~ 0.5 m/s (crack speed as fast as 1.5 m/s was recorded on the Visi-corder chart paper at 353 °K but the corresponding R values could not be determined because of the fast change of load trace in this fast crack speed range). The fracture surface at 353 °K (see Figure 37) shows a distinct change in roughness at 0.5 m/s above which smoother surface is shown. From the observation of these smoother fracture surfaces it seems likely that the fracture toughness value may decrease above 0.5 m/s (Figure 37).

IV.3.2 PC

IV.3.2.1 K_{IC} results

The experimental K_{IC} results of PC are shown in Table 5 and they are plotted in Figure 39. They were calculated by introducing the 'pop-in' load in equation (4.12b). The pop-in mark was, in general, not noticeable in the load-displacement of the fracture test made at the slowest crosshead speed (8.33 $\mu\text{m/s}$) until the temperature decreased down to 233 $^{\circ}\text{K}$. Pop-in marks on the load-displacement were most easily resolvable with the fracture test at 83.3 $\mu\text{m/s}$ crosshead speed. At higher crosshead speed, significant scatter in the pop-in load was observed for the same test condition. Two crosshead speeds (83.3 $\mu\text{m/s}$ and 8.33 mm/s) were used extensively throughout the temperature range for K_{IC} tests while a limited number of tests were also made at low temperatures in an effort to achieve various crack speeds for the study of fracture toughness value to be discussed in the next section.

Usually a pop-in mark in the load displacement curve is followed by a nonlinear increase in load, during which the plastic zone develops at the crack tip (see Figure 40). Finally the load reaches a maximum at a significantly higher level (compared to pop-in load) and starts to decrease as the crack proceeds. Sometimes an unstable, fast fracture occurred at the pop-in loads. Both pop-in load and maximum load are given in Table 5. There is a considerable scatter in K_{IC} results for the crosshead speed of 8.33 mm/s , while the results from the crosshead speed of 83.3 $\mu\text{m/s}$ are fairly consistent.

TABLE 5

EXPERIMENTAL RESULTS OF K_{IC} OF POLYCARBONATE

Crosshead Speed ($\mu\text{m/s}$)	Temperature ($^{\circ}\text{K}$)	Thickness (mm)	Pop-in Load (N)	Maximum Load (N)	K_{IC} ($\text{MN/m}^{\frac{3}{2}}$)
83.3	213	6.30	409	577	2.00
	233	6.27	404	493	1.97
	243	6.30	449	484	2.36
	253	6.22	489	489	2.42
	263	6.26	502	502	2.47
	273	6.21	621	1000	3.08
	273	6.22	609	733	3.01
	283	6.25	666	785	3.28
	296	6.25	680	680	3.34
	313	6.32	710	710	3.46
	353	6.22	764	(*)	3.78
	8,333	213	6.26	581	581
233		6.30	444	546	2.17
243		6.32	510	510	2.48
253		6.25	360	573	1.77
263		6.22	529	737	2.61
273		6.25	555	555	2.73
273		6.27	466	635	2.26
283		6.30	502	661	2.45
288		6.30	630	630	3.08

TABLE 5 (CONTINUED)

Crosshead Speed ($\mu\text{m/s}$)	Temperature ($^{\circ}\text{K}$)	Thickness (mm)	Pop-in Load (N)	Maximum Load (N)	K_{IC} ($\text{MN/m}^{\frac{3}{2}}$)
8,333	296	6.22	635	635	3.14
	313	6.30	675	675	3.30
	353	6.25	810	810	3.98

(*) Test was interrupted while load was increasing

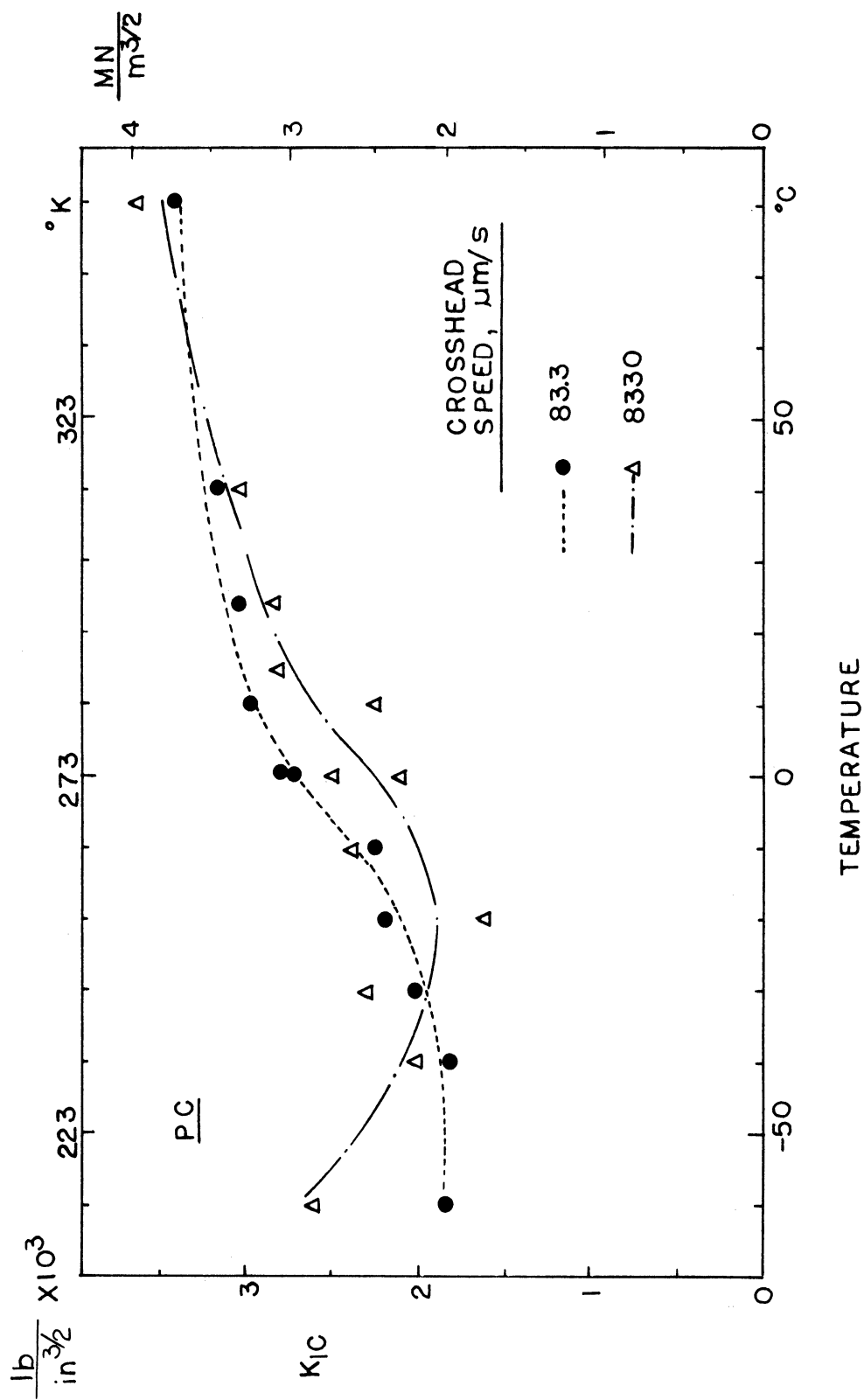


Figure 39. K_{IC} as a function of temperature and crosshead speed

IV.3.2.2 R results

When a polycarbonate fracture specimen is loaded at a constant crosshead speed (83.3 $\mu\text{m/s}$, for example), a crack first starts at the notch, it is arrested immediately (less than 3 mm of propagation which corresponds to the pop-in mark in the load displacement curve), and a fairly large plastic yield zone ($r_y \approx 6$ mm at room temperature) slowly develops in the immediate vicinity of the crack tip. When the crack starts to move, this plastic yield zone follows the crack movement in front of the crack tip. Due to this large irreversible plastic flow at the crack tip, unloading is not "displacement reversible", i.e. the specimen does not close back up completely when unloaded to zero load. Figure 40 shows a load displacement curve of two fracture tests of PC: one from continuous loading and the other from interrupted loading. A significant amount of offset displacement is shown upon unloading and this offset displacement increases as the crack length increases. This causes a difficulty in employing Gurney's method of measuring R values (see Figure 2) because the basic assumption of Gurney's method is that the strain energy in the specimen is completely recoverable upon unloading, instead of being locked up as a self-equilibrating residual stress around the plastic yield zone. Fortunately, for PC, the size of a local yield zone near the moving crack decreases as the testing temperature decreases (this can be seen from fracture surfaces which will be shown later in chapter V). When the temperature reaches 213 $^{\circ}\text{K}$, negli-

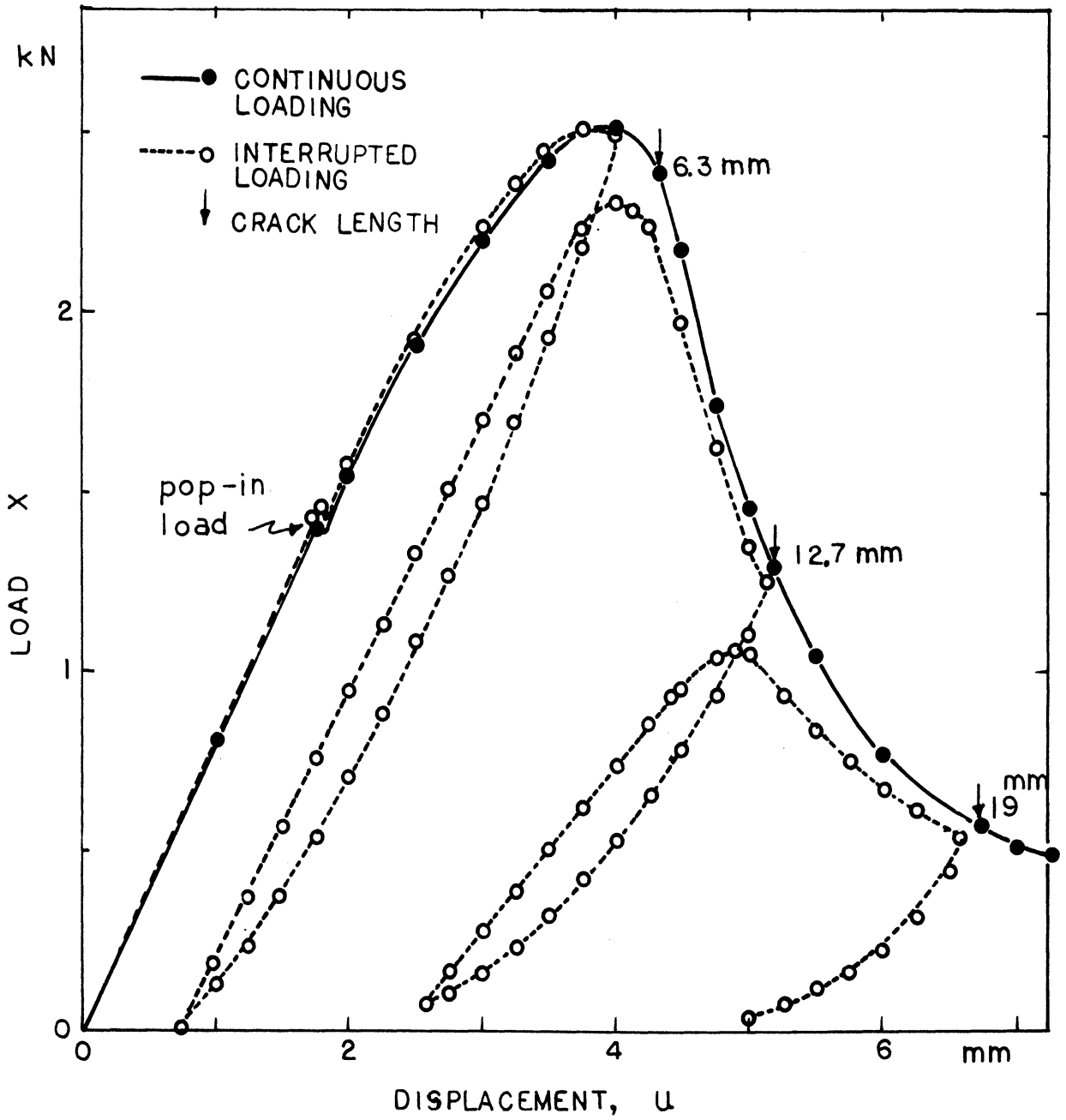


Figure 40. Load-displacement curves of PC fracture tests. (These curves were obtained from a preliminary study with single edge notch specimens of PC, instead of compact tension specimen used in the actual experiments).

gible "shear lips" are shown in the fracture surface. For this case Gurney's method is applicable and leads to negligible error in the results. As the temperature increases, the proportion of shear lip size increases further into the thickness of the specimen until the full thickness has fully yielded at room temperature. Gurney's method was employed up to 273 °K, admitting some inevitable errors due to the increasing size of the plastic shear zone. Yet because the whole section has not fully yielded (see the fracture surfaces in chapter V), this approach is assumed to provide a reasonable approximation, and gives an upper bound in R. The results are shown in Figure 41. It seems that within the range of crack speeds observed during stable crack growth tests, the fracture toughness, R, of polycarbonate shows little dependence on crack speed, except at 273 °K where a significant drop in R value is seen in one decade of crack speed (Figure 41). This may be due to the reduction of the plastic shear zone size at higher crack speeds.

IV.4 Discussion of results

IV.4.1 PMMA: Proposed Theory on Stable Crack Growth Rate

Experimental results of K_{IC} in Figure 26 show a consistent increase in K_{IC} as the temperature decreases from 353 °K to 283 °K for all of the crosshead speeds involved (higher crosshead speeds giving higher K_{IC} values). As the temperature decreased further below 283 °K, K_{IC} results start to show some transitional behavior. For example,

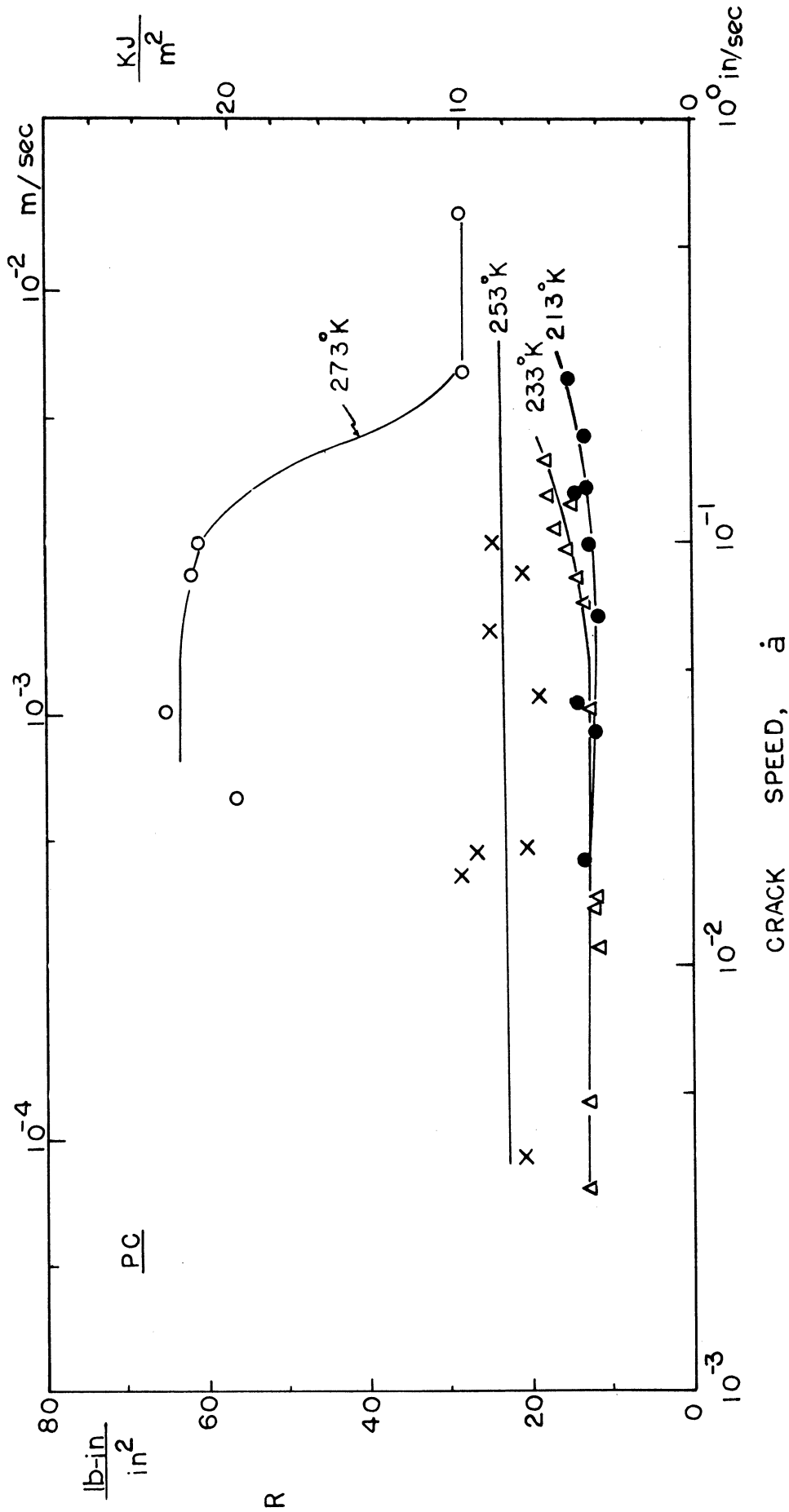


Figure 41. Fracture toughness, R , of PC as a function of crack speed at temperatures of 273°K , 233°K , 253°K and 213°K

K_{IC} results from the highest crosshead speed (8.33 mm/s) show a maxima at 273 °K. Similar transitional behavior also occurs with K_{IC} results for lower crosshead speeds at decreasing temperature.

When the fracture toughness, R , results (Figure 29 through 37) are examined, they also show that the family of R vs. $\log_{10} \dot{a}$ curves obtained above 283 °K are different from those obtained below 283 °K (see Figure 42 and 43 for comparison). An attempt is made in the following sections to describe the fracture behavior above 283 °K in terms of an empirical relationship between fracture toughness and crack speed. The transitional behavior of K_{IC} results and R results occurring below 283 °K is attributed to a transition in the molecular relaxation mechanism.

A number of studies have been reported on the kinetics of craze growths in PMMA (Sauer and Hsiao 1953, Regel 1956, Higuchi 1966). Total range of the growth involved less than 1 mm. However there are very few studies on the kinetics of actual crack growth in glassy polymers including PMMA.

Marshall, Culver and Williams (1970) studied the crack growth rate of PMMA in a methanol environment using the fracture parameter, K , as a variable. However, since the growth rate was expressed in terms of the initiation K , rather than the current K during crack propagation, their expression has a limited range of application.

Zhurkov (1965) made a general study of the kinetics of the fracture of solids under dead load conditions and found that a wide range of materials follow the Ree-Eyring (1957) stress-biased failure kinetics relationship:

$$t_f = A_0 \exp \left(\frac{\bar{U} - \phi \sigma}{\bar{k}T} \right) \quad (4.7)$$

where t_f is the time to failure measured from the moment of loading, and where

A_0 is some constant ϕ is some constant
 \bar{U} is the activation energy T is temperature in $^{\circ}\text{K}$
 \bar{k} is the Boltzmann constant σ is tensile stress

Equation (4.7) was applied to uniaxial specimens of small diameter for which the fracture propagation time was negligible compared to the crack initiation time.

From the present results of PMMA fracture toughness against crack speed, in the temperature range 283 $^{\circ}\text{K}$ to 353 $^{\circ}\text{K}$, it is proposed that the crack growth rate, \dot{a} , be expressed as,

$$\dot{a} = A_1 \exp \left\{ \frac{-(\bar{U} - \lambda R)}{\bar{k}T} \right\} \quad (4.8)$$

where R is the fracture toughness (equivalent to the strain energy release rate, G), and A_1 and λ are constants to be

determined from curve fitting the data. The activation energy \bar{U} is also obtained from the curve fitting of data.

Equation (4.8) can be rewritten as,

$$\frac{R}{T} = \frac{\bar{k}}{\lambda} \log_e \dot{a} + \frac{\bar{U}}{\lambda T} - \frac{\bar{k}}{\lambda} \log_e A_1 \quad (4.9)$$

Table 6 shows the curve fitting equations derived from equation (4.9) and the constants (λ , A_1 and \bar{U}) determined from the best fit of the experimental data. Both the experimental data and the curve fitting equations in Table 6 are modified to give an explicit expression for R , and compared in Figure 42 for the temperature range of 283 °K to 353 °K. The family of curves predicted from equation (4.9) shows a good fit with the experimental data between 283 °K to 353 °K, but the experimental points start to deviate from the predicted curve at the lower end of crack speed for each temperature. The slope of $\frac{R}{T}$ against $\log_{10} \dot{a}$ is a constant, which is 0.155 J/m² °K as shown in Table 6. However, since the fitting curves in Figure 42 are plotted in R vs. $\log_{10} \dot{a}$ rather than $\frac{R}{T}$ vs. $\log_{10} \dot{a}$, they show increasing slope as the temperature increases. When these fitting curves are extrapolated they converge into one point and the corresponding crack speed at this point came close to 10⁵ km/s, which is the value of A_1 in Table 6. This limiting value may be connected with the limiting rupture time reported by Zhurkov (1965) which is in the order of molecular vibration period.

TABLE 6

CURVE FITTING EQUATIONS AND CONSTANTS
OBTAINED FROM THE EXPERIMENTAL
FRACTURE TOUGHNESS DATA
OF PMMA

$$\frac{R}{T} = \frac{\bar{k}}{\lambda} \log_e \dot{a} + \frac{\bar{U}}{\lambda T} - \frac{\bar{k}}{\lambda} \log_e A_1$$

<u>T (°K)</u>	<u>Curve fitting equations (\dot{a} in m/s)</u>
283	$\frac{R}{T} = 0.1553 \log_e \dot{a} + 2.832 \text{ (J/m}^2 \text{ °K)}$
296	$\frac{R}{T} = 0.1553 \log_e \dot{a} + 2.56 \text{ (J/m}^2 \text{ °K)}$
318	$\frac{R}{T} = 0.1553 \log_e \dot{a} + 2.21 \text{ (J/m}^2 \text{ °K)}$
333	$\frac{R}{T} = 0.1553 \log_e \dot{a} + 1.973 \text{ (J/m}^2 \text{ °K)}$
353	$\frac{R}{T} = 0.1553 \log_e \dot{a} + 1.7 \text{ (J/m}^2 \text{ °K)}$

From the above curve fitting equations using the Boltzman constant, $\bar{k}=8.313 \text{ J/mole } ^\circ\text{K}$, the constants A_1 , λ and the activation energy \bar{U} are determined as follows.

$$A_1 = \exp (18.4) \text{ m/s}$$

$$\lambda = 53.1 \text{ m}^2/\text{mole}$$

$$\bar{U} = 86.02 \text{ kJ/mole} = 20.55 \text{ kcal/mole}$$

R values generally level off (between 250 to 300 J/m²) at the lower end of crack speed for each temperature. This agrees with the findings of Marshall et al (1970) that there exists a lower limit in K, below which no significant crack extension was observed. The upper limit of the applicable range of equation (4.9) is when the crack starts to run unstably. It may be noted that unstable crack propagation starts to occur at the crack speed when the corresponding R value reaches ~ 600 J/m² for most of the temperatures involved in the present study (except the results from 253 °K which show a value of R as high as 740 J/m² before unstable cracking occurs (Figure 43)). The activation energy of 86.02 kJ/mole (20.55 kcal/mole) obtained for the temperature range 283 °K to 353 °K is significantly larger than the apparent activation energy reported by Broutman and Kobayashi (1971) who obtained 9.3 kcal/mole for a similar range of temperature and crack speeds by horizontally shifting their fracture surface energy data. However, the present result agrees with the 24 kcal/mole given by Johnson and Radon (1972), who calculated the apparent activation energy from K_{IC} results by using the Arrhenius equation, with crosshead speed as a rate parameter. A similar treatment of the present data has been performed, as shown in Figure 44. The temperature and crosshead speed values were all picked from the K_{IC} data in Figure 45 at the same K_{IC} level (1.5 MN/m^{3/2}) which cuts across the K_{IC} curve at the region where K_{IC} is steadily increasing at decreasing temperature. An apparent activation energy of 81.2 kJ/mole was obtained from Figure 44. This activation energy obtained

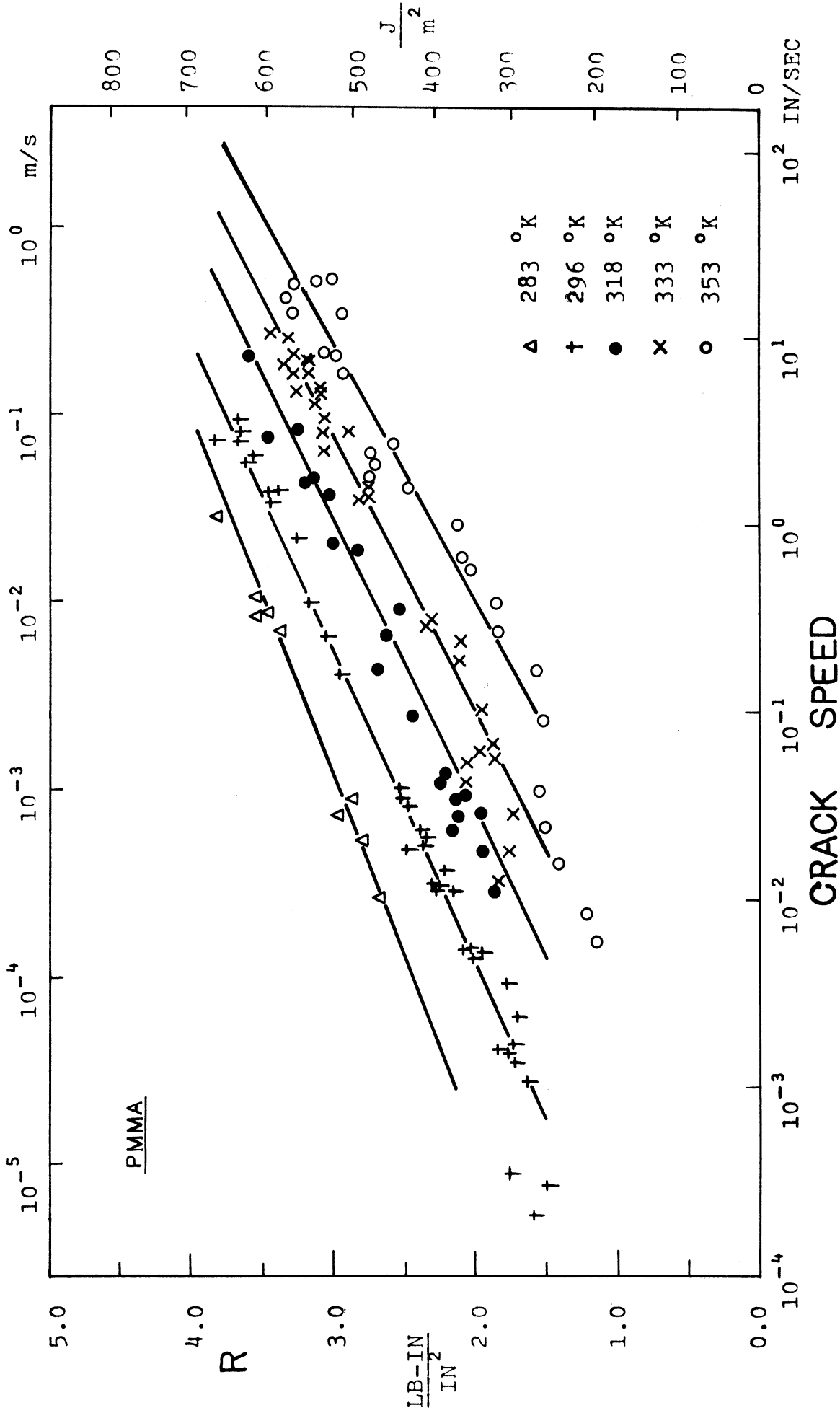


Figure 42. Fitting curves for fracture toughness against crack speed at temperatures, 283°K through 353°K

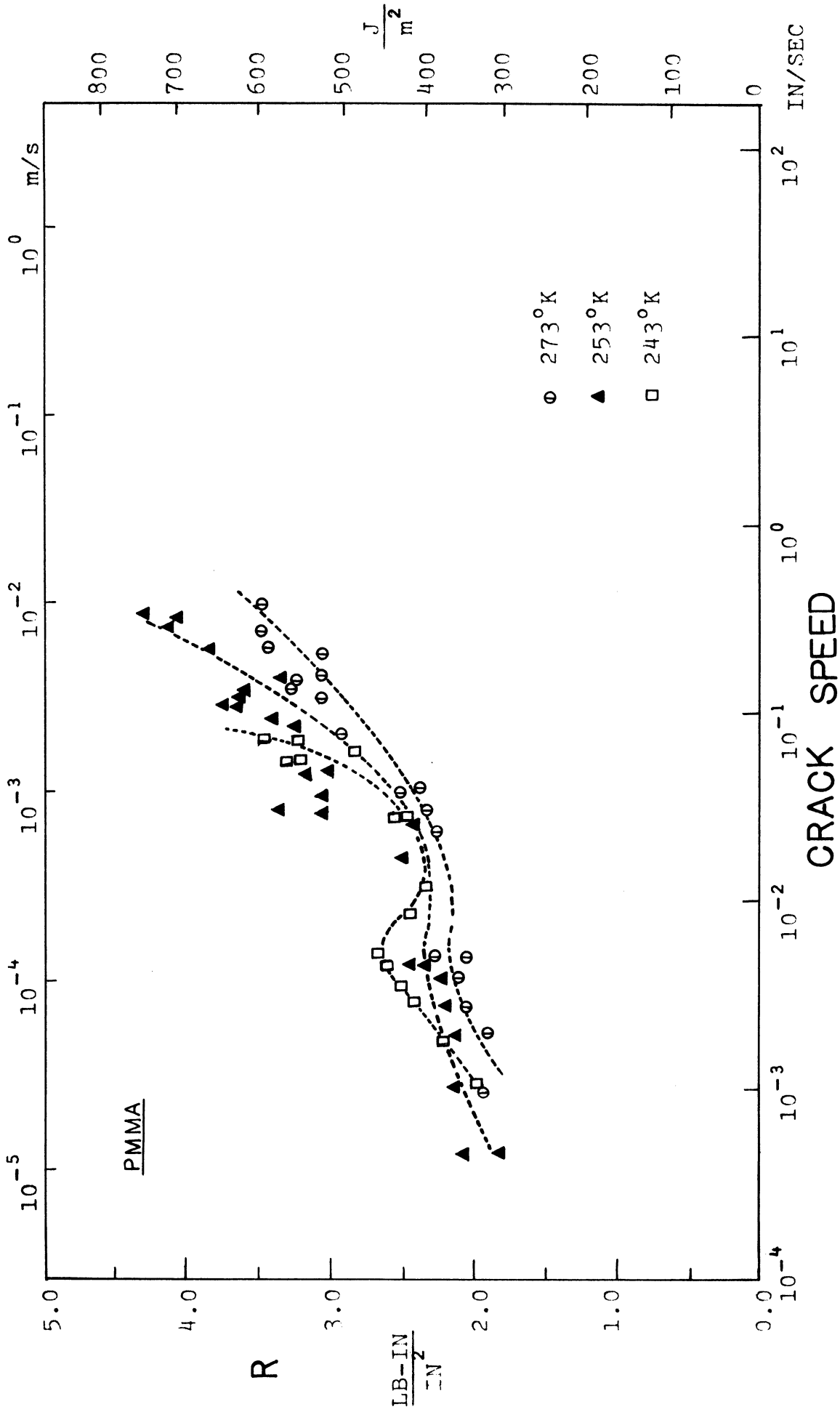
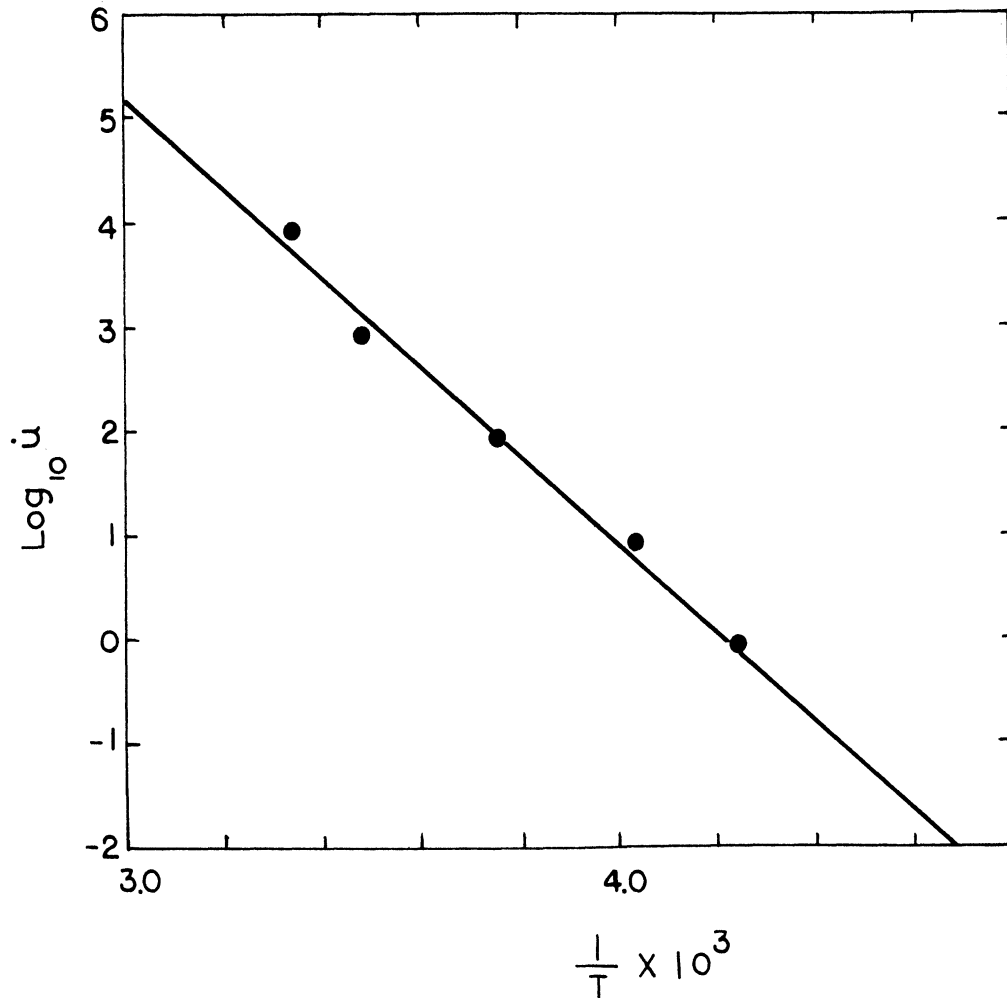


Figure 43. Fracture toughness results against crack speed at temperatures, 243°K, 253°K and 273°K



Using the Arrhenius Equation,

$$\dot{u} = A \exp\left(-\frac{\bar{U}}{kT}\right)$$

$$\log_e \dot{u} = \log_e A - \frac{\bar{U}}{kT}$$

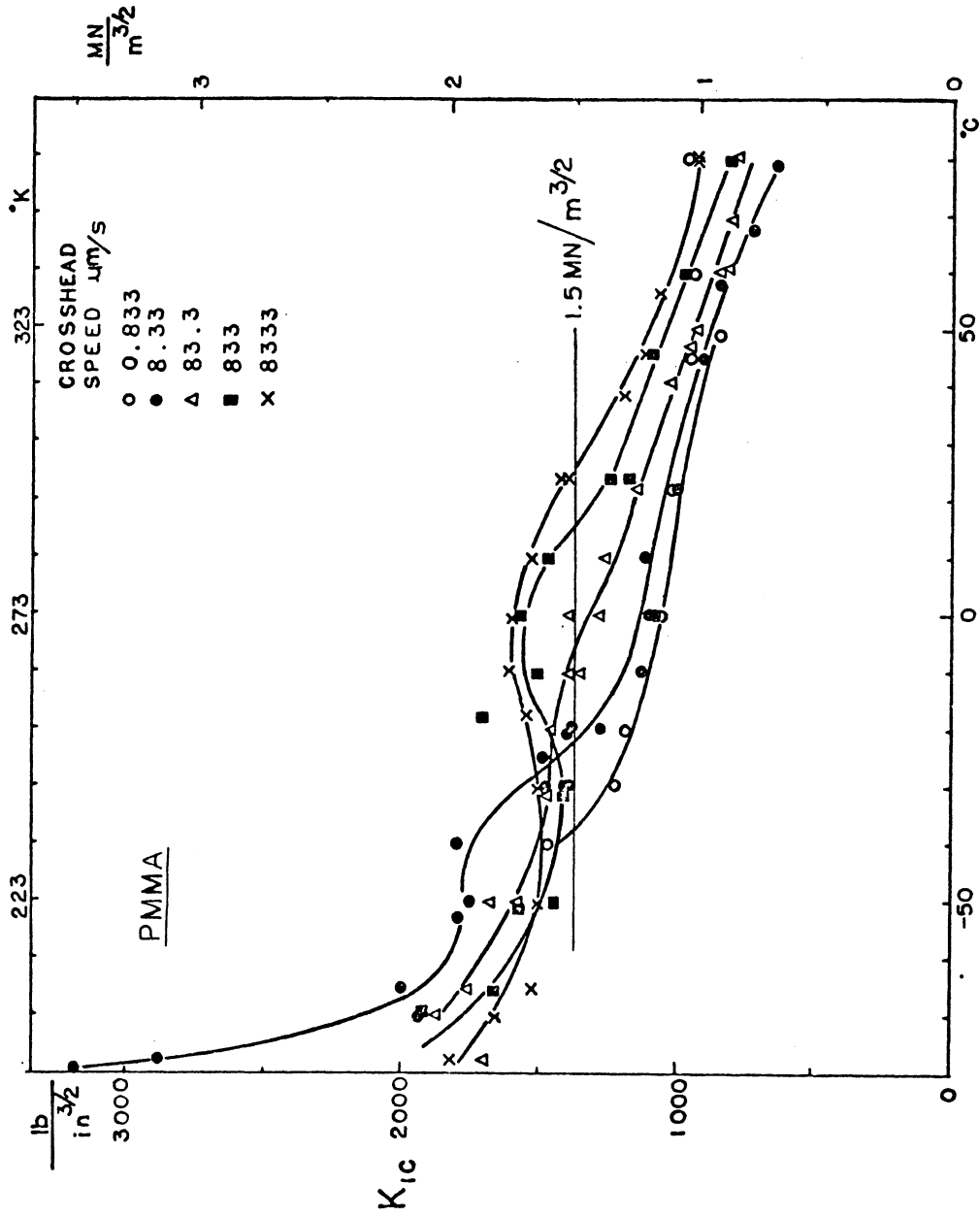
From the slope in the above plot,

$$-\frac{\bar{U}}{k} = -9.8 \times 10^3$$

Since $\bar{k} = 8.313 \text{ J/mole}^\circ\text{K} = 1.986 \text{ cal/mole}^\circ\text{K}$

$$\bar{U} = 81.2 \text{ kJ/mole} = 19.4 \text{ kcal/mole}$$

Figure 44. $\log_{10} \dot{u}$ vs. $1/T$ plot corresponding to $K_{IC} = 1.5 \text{ MN/m}^{\frac{3}{2}}$ as shown in Figure 45



TEMPERATURE

Figure 45. Data points for the plot in Figure 44 are picked at $K_{Ic} = 1.5 \text{ MN}/\text{m}^{3/2}$

from the K_{IC} data is in good agreement with one obtained from the R vs. crack speed data.

The fracture toughness vs. crack speed data below 283 °K are shown in Figure 43. It is clear that they do not follow the same family of curves predicted by equation (4.9). This sudden change in the fracture toughness (R) behavior below 283 °K seems to be consistent (at least qualitatively) with the K_{IC} results shown in Figure 26. K_{IC} values for all crosshead speeds (over four decades) show a steady increase as the temperature decreases until it reaches 273 °K when the K_{IC} at the highest crosshead speed (8330 $\mu\text{m/s}$) reaches a maxima. It was at this same temperature that the R vs. 'a' curve started to deviate from the family of curves predicted by equation (4.9). As the temperature decreased further, the K_{IC} curves corresponding to slower crosshead speeds reached either maxima or plateau. It seems that this behavior may be related to a transition of the molecular relaxation mechanisms involved in the fracture process. And the fact that no stable crack growth was possible below 243 °K at even the slowest crack speed (0.833 $\mu\text{m/s}$) might be a manifestation that a different molecular relaxation mechanism is involved below this temperature.

The present experimental results of both K_{IC} and R of PMMA seems to indicate that the growth of a stable crack is an activated process, the rate of which is dependent on both temperature and the fracture toughness. The activation energy

obtained from the kinetics of stable crack growth indicate that the basic molecular mechanism could be attributed to the β process, at least in the temperatures ranging from 283 °K to 353 °K. Present results support Boyer's (1968) explanation that the (stable) crack growth at room temperature is essentially a craze growth, which, in turn, is controlled by the β process. However, the distinct change in fracture behavior below 283 °K defies the generalization of fracture behavior in terms of a single molecular relaxation mechanism for the whole temperature range of the present experiments. Further investigation of the molecular involvement at the crack tip may lead to an explanation for the different fracture behavior of PMMA below 283 °K down to 203 °K.

IV.4.2 Polycarbonate : Effect of Plastic Enclave Size.

Due to the formation of a plastic yield zone at the crack tip of PC fracture specimens, Gurney's method of fracture toughness measurement is limited to the low temperature region at which plastic flow was restricted to a negligible portion of the total cross section.

Thus, in the case of PC, most of the source of toughness comes from the gross plastic flow around the crack tip rather than from craze formation and growth as in PMMA. Consequently, the fracture toughness of a PC specimen depends mainly on the amount of plastic flow at the crack tip. The amount of plastic flow decreased as the temperature decreased and also

as the crack speed increased. As the temperature decreased to 213 °K only negligible shear lips were present at both edges of a fracture surface and the application of Gurney's method for measuring R values at this low temperature is justified. The error gets bigger as the temperature is increased above 213 °K, due to increasing amount of plastic flow at the crack tip. When the temperature reaches 296 °K (room temperature) plastic flow has occurred throughout the whole cross section. Gurney's method was applied only up to 273 °K.

Since the change in the fracture toughness due to crack speed was small compared to the change due to temperature, the variation of fracture toughness is represented in Figure 46 by a range between the maximum and the minimum values observed at the temperature. The data points between 213 °K to 273 °K are obtained from Figure 41 and variations in R at each temperature are due to different crack speeds at each temperature. The data point at room temperature was obtained by dividing the total area under the load-displacement curve of a fracture test by the nominal area of crack surface generated. Mai (1973) has recently published the variation of R as function of crack speed at room temperature using the parallel cleavage specimen with side grooves. His result is also plotted in Figure 46 for comparison. A sharp drop (a decade decrease) in fracture toughness occurs between 296 °K to 273 °K, and as the temperature decreased further it decreased to an asymptotic value of about 2 kJ/m².

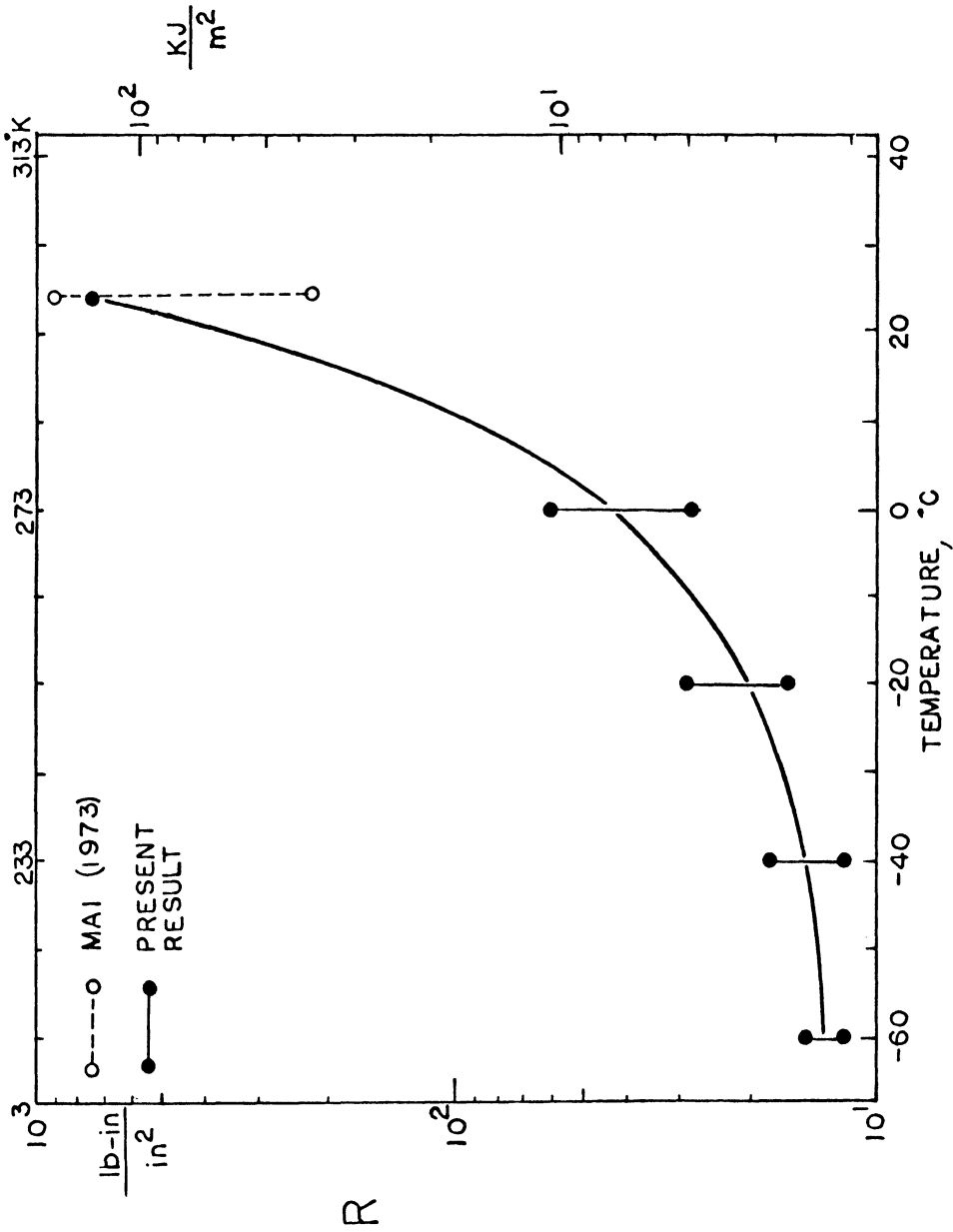


Figure 46. Fracture Toughness of PC as a function of temperature for various crack speeds, as shown by the vertical spread in values at each temperature. Below about 263 °K the larger toughness occurs at faster crack speeds, but at higher temperatures the fast cracks produce low toughnesses

Similar results were found (by Hull and Owen 1973) from the notch impact test results of PC.

IV.4.3 Equivalent strain rate and equivalent Young's modulus of a fracture specimen

Young's modulus plays an important role in fracture mechanics in determining various fracture parameters such as $K = \sqrt{ER}$, $\sigma_f = \sqrt{\frac{E\gamma}{\pi a}}$, and in making an experimental K-calibration as shown in IV.3.4. When a fracture test is made with a highly rate dependent material, like PMMA, the Young's modulus is not a constant but changes significantly with "equivalent strain rate" and temperature. In order to determine a proper modulus value for a given fracture test, an estimate of equivalent strain rate is necessary. However, the determination of an equivalent strain rate in fracture involves a complex mathematical difficulty due to the non-uniform stress distribution. Some approximate expressions have been reported for an equivalent strain rate associated with the material elements close to the crack tip. In the following sections, approximate equivalent strain rate expressions will be used to obtain the equivalent Young's modulus for a stationary crack, and the Young's modulus for a moving crack will be obtained independently from the experimental results of K_{IC} and R of PMMA. The two sets of Young's modulus (one from stationary crack and the other from moving crack) will be compared later.

IV.4.3.1 Analysis of the equivalent strain rate involved with fracture testing

Approximate analysis for the strain rate at a crack tip have been made by Irwin (1963) in his fracture study with metals and Williams (1972) later extended it further for applications on polymers.

From the expression for the stress around the crack tip given in equation (2.17),

$$\sigma = \frac{K}{\sqrt{2\pi r}} \quad \text{at} \quad \theta = 0$$

we obtain the expression for strain near the crack tip,

$$e = \frac{K(t)}{E(t)} \cdot (2\pi r)^{-\frac{1}{2}} \quad (4.10)$$

where both $K(t)$ and $E(t)$ are considered to be functions of time. Differentiating equation (4.10) with respect to time and using the relationship $\dot{a} = -\dot{r}$ (because the rate of change of crack length or crack speed, \dot{a} , is the same as the rate of change of distance between the crack tip and a fixed point away from the crack tip (along $\theta=0$), the expression for strain rate at the crack tip is (see Appendix II for derivation),

$$\dot{e} = e \left(\frac{\dot{K}}{K} - \frac{\dot{E}}{E} \right) + \pi e^3 \left(\frac{E}{K} \right)^2 \dot{a} \quad (4.11)$$

where the dot notation implies derivatives with respect to time. When the crack speed is zero, which is the case for loading on a stationary crack, equation (4.11) becomes,

$$\dot{e} = e \left(\frac{\dot{K}}{K} - \frac{\dot{E}}{E} \right) \quad (4.12)$$

Unless a very slow loading rate is applied, the change of modulus during a single fracture test can be neglected.

This assumption is justified because the slope of a loading path is a straight line before fracture starts (see Figure 27 and 28) for PMMA. For a stationary crack, $\dot{E} \rightarrow 0$, and

$$\dot{e} = e \frac{\dot{K}}{K} \quad (4.13)$$

Equation (4.13) can be expressed in terms of crosshead speed because,

$$\frac{\dot{K}}{K} = \frac{\dot{X}}{X} = \frac{k\dot{u}}{ku} = \frac{\dot{u}}{u} \quad (4.14)$$

where k is the stiffness of the fracture specimen. From equation (4.13) and (4.14), the equivalent strain rate expression for stationary crack becomes,

$$\dot{e} = \frac{e}{u} \cdot \dot{u} \quad (4.15)$$

Assuming that the significant portion of crack tip material reaches the yield strain at the initiation of fracture,

$$\dot{e} = \left(\frac{e_y}{u_c} \right) \cdot \dot{u} \quad (4.16)$$

where e_y is yield strain and u_c is the crack opening displacement measured at the loading pin at the time of crack initiation. Some arbitrariness cannot be avoided in choosing e_y value in equation (4.16). In the present study, e_y was chosen as the total strain corresponding to the 0.3% offset yield stress from the uniaxial tensile test. The e_y value at room temperature thus determined from the uniaxial tensile test was about 2%, which is reasonably close to, yet slightly higher than the critical strain level (1.3%) for crack initiation in PMMA at room temperature, reported by Kambour (1972). Since the crack initiates after the craze has formed and then a dominant craze develops into a crack, present choice of e_y seems to provide a reasonable representation of strain level at crack initiation. Thus, the equivalent Young's modulus of a fracture specimen, when the crack is stationary, may be obtained from known $E(\dot{\epsilon})$ data (from uniaxial tensile tests), using equation (4.16) for $\dot{\epsilon}$. This method of determining the equivalent Young's modulus was employed in section IV.2.4.

Equivalent strain rate associated with a moving crack is given by Williams as,

$$\dot{\epsilon} = \pi e^3 \left(\frac{E}{K}\right)^2 \dot{a} \quad (4.17)$$

which is obtained from equation (4.11) by neglecting the first term which he observed to be small compared to the second term unless the crack moves at negligibly slow speed.

The high strain rate associated with the moving crack applies only to the elements near the immediate vicinity of a moving crack tip, whereas the majority of elements in a fracture specimen undergo substantially low strain level at substantially low strain rates. Williams obtained the equivalent modulus based on the strain rate obtained from equation (4.17). Since his result has not been supported with experimental evidence, validity of such practice, i.e., finding the equivalent modulus of a fracture specimen based on the strain rate involved at the moving crack tip, has not been tested yet. This will be tested here by comparing the equivalent Young's modulus from an independent method with the results given by Williams. An alternative method of evaluating the equivalent Young's modulus of a moving crack is available: Since K and R can be simultaneously obtained from the load-displacement curve of a moving crack, the equivalent modulus, E , can be directly calculated from $E=K^2/R$ without using equation (4.17). Experimental determination of the equivalent modulus for both stationary and moving cracks is given in the following section.

IV.4.3.2 Experimental determination of the equivalent Young's modulus for a stationary crack and a moving crack

IV.4.3.2.1 Stationary crack

The stiffness, k , of a fracture specimen may be expressed as a product of two variables, viz., the equivalent Young's modulus (which is rate and temperature dependent),

and a function Y which depends on the geometry and crack length of the specimen only.

$$k(t,T) = E(t,T) \cdot Y(a,W,B,H) \quad (4.18)$$

Since Y is a function depending on the geometry of the specimen only, any variation on stiffness due to change in loading rate and temperature will be directly proportional to the change in modulus,

$$\frac{k_2(t,T)}{k_1(t,T)} = \frac{E_2(t,T) \cdot Y(a,W,B,H)}{E_1(t,T) \cdot Y(a,W,B,H)} = \frac{E_2(t,T)}{E_1(t,T)} \quad (4.19)$$

Consequently, if we know the equivalent modulus of the fracture specimen at a particular crosshead speed and temperature, the equivalent modulus at any other crosshead speed and temperature can be determined by using the proportional relationship in equation (4.19). Since the equivalent modulus determined in section IV.2.4, using equation (4.16), was found to be satisfactory, this modulus value ($E=3.24 \text{ GN/m}^2$ at $u=8.33 \text{ } \mu\text{m/s}$) will be used as a reference value in determining the equivalent modulus involved with other crosshead speeds.

Thus, the stiffness of the fracture specimen (see Figure 16 for geometry) was measured for each test temperature and crosshead speed from the initial slope of the load displacement curve (before the crack starts to propagate). By comparing each stiffness value with the reference stiff-

ness value (of the specimen at 8.33 $\mu\text{m/s}$ and at 296 $^{\circ}\text{K}$), a proper modulus value can be assigned to each specimen using the proportional relationship between k and E in equation(4.19). The stiffness, k_1 , of the fracture specimen (with $a=50.8$ mm) measured at the test condition, $\dot{u}=8.33$ $\mu\text{m/s}$ and $T=296$ $^{\circ}\text{K}$ is;

$$k_1 = 479 \text{ N/m (2740 lb/in)}$$

and the equivalent rate calculated from equation (4.16) is (see section IV.2.4),

$$e_1 = 3.28 \times 10^{-4} \text{ s}^{-1}$$

The corresponding equivalent Young's modulus found from the uniaxial tensile test by interpolation is,

$$E_1 = 3.24 \text{ GN/m}^2$$

The equivalent Young's modulus at some other testing condition, E_x , is determined by the stiffness, k_x , measured from the load displacement curve by,

$$\frac{E_x}{E_1} = \frac{k_x}{k_1}$$

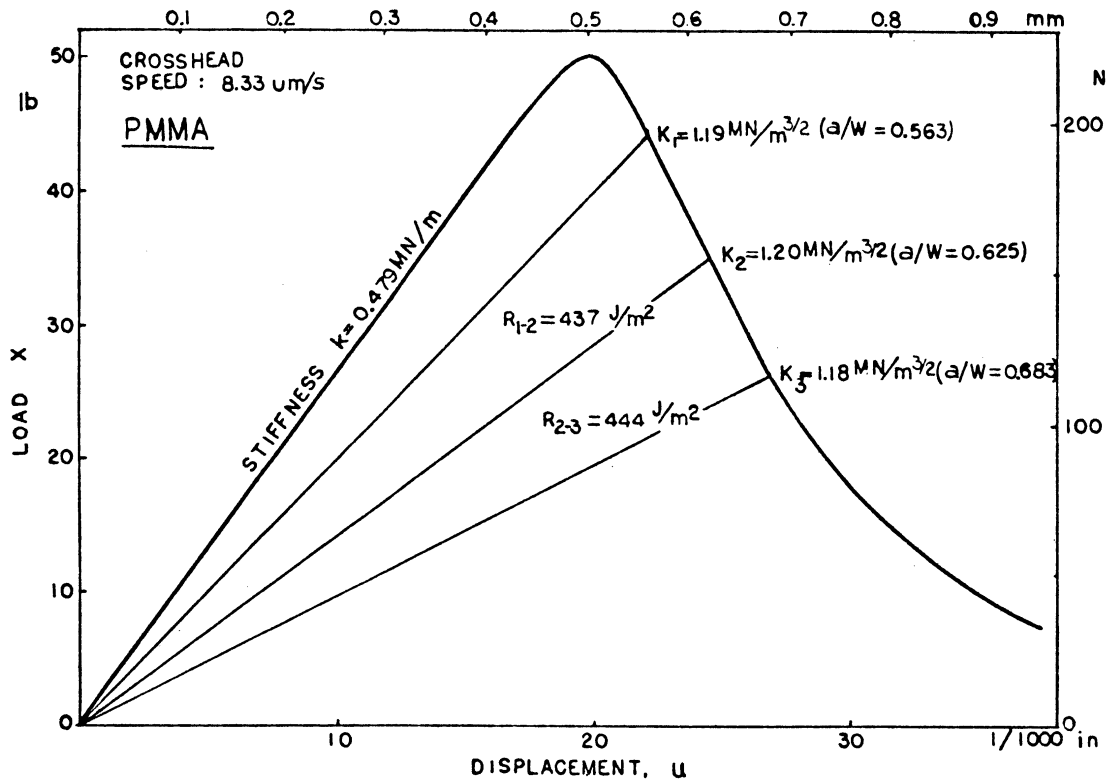
$$E_x = \frac{E_1}{k_1} k_x = 6.76 \times 10^6 k_x \quad (4.20)$$

where E_x is in N/m^2 and k_x is in N/m . Because there was some

minor variation of thickness values among the specimens, each k_x value is taken as the normalized value from the actual thickness value to that of $B=6.35$ mm. An example of calculating an equivalent modulus of a specimen with stationary crack is given in Figure 47a. Figure 48 shows the equivalent Young's modulus calculated from the initial stiffness, k , of the fracture specimen ($a/W=0.5$) at various temperatures and crosshead speeds. Data points for each temperature were represented by a smooth curve that was drawn approximately through the median of data points. These equivalent modulus values for stationary crack cases will be compared later with those values for moving cracks.

IV.4.3.2.2 Moving crack

The equivalent Young's modulus value for a moving crack was calculated directly from the present experimental data of K and R using the relationship $E=K^2/R$ (see equation (2.18)). R values were obtained from the sector areas in the $X-u$ curve (see Figure 3) and the corresponding K values (for the moving crack) have been determined by using the current load, X , in the K -calibration expression associated with the current crack length (see Table 3 and equation (4.21)). K values were determined at three crack length locations, viz: $a/W=0.563$, $a/W=0.625$, $a/W=0.688$. These crack lengths were chosen because the silver paint circuit grids were on these locations and the fairly dependable K -calibration ex-



- a). Determination of equivalent Young's modulus for a stationary crack:

From the initial slope of X-u curve,

$$k_x = 0.479 \text{ MN/m}$$

Applying equation (4.20)

$$E_x = 6.76 \times 10^3 k_x = 3.24 \text{ GN/m}^2$$

- b). Determination of equivalent Young's modulus for a moving crack:

Crack Location	1-2:	$\bar{K}_{1-2} = (K_1 + K_2)/2 = 1.195 \text{ MN/m}^{\frac{3}{2}}$
		$E_{1-2} = (\bar{K}_{1-2})^2 / R_{1-2} = 3.27 \text{ GN/m}^2$
		$\dot{a}_{1-2} = 0.88 \times 10^{-3} \text{ m/s}$
Crack Location	2-3:	$\bar{K}_{2-3} = (K_2 + K_3)/2 = 1.19 \text{ MN/m}^{\frac{3}{2}}$
		$E_{2-3} = (\bar{K}_{2-3})^2 / R_{2-3} = 3.2 \text{ GN/m}^2$
		$\dot{a}_{2-3} = 0.81 \times 10^{-3} \text{ m/s}$

Figure 47. Example of calculating equivalent Young's modulus for a stationary and a moving crack

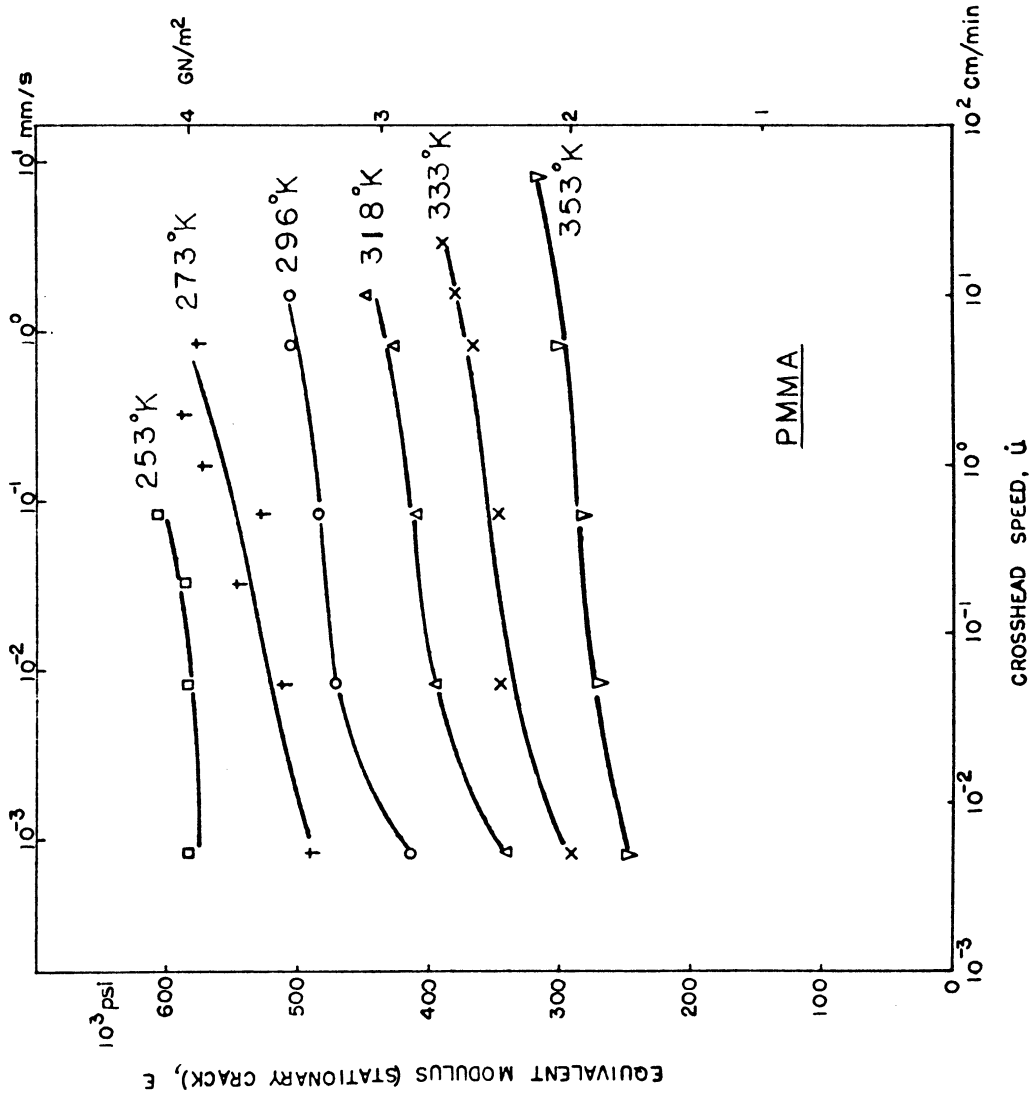


Figure 48. Equivalent Young's modulus for the stationary crack

pressions were available for these regions. Since the R values measured at the intervals, $a/W=0.563$ to 0.625 , $a/W=0.625$ to 0.688 are also available from the same load-displacement curve, the modulus values at these crack lengths and associated crack speeds can be calculated from the $E=K^2/R$ relationship. An example of calculating the equivalent modulus from a load displacement curve is given in Figure 47b. K_1 , K_2 , and K_3 are the stress intensity factors at the crack locations $a/W=0.563$, 0.625 and 0.688 , respectively. These were determined from the K-calibration results in Figure 24, by interpolation:

$$\frac{KBW^{\frac{1}{2}}}{X} = \begin{cases} 12 & \text{for } a/W=0.563 \\ 15.2 & \text{for } a/W=0.625 \\ 20 & \text{for } a/W=0.688 \end{cases} \quad (4.21)$$

Thus, K_1 , K_2 and K_3 shown in Figure 47, are calculated from equation (4.21) to be 1.19, 1.20 and 1.18 MN/m². Taking the average value of K_1 and K_2 and the associated fracture toughness value R_1 into equation (2.18), the equivalent Young's modulus for this interval is calculated to be $E_{1-2} = 3.27$ GN/m². Following the same procedure, E_{2-3} is obtained to be 3.20 GN/m². Since the crack speed for each interval is known, it is possible to plot E as a function of crack speed. The equivalent modulus values for moving cracks are plotted in Figure 49 as a function of crack speed under

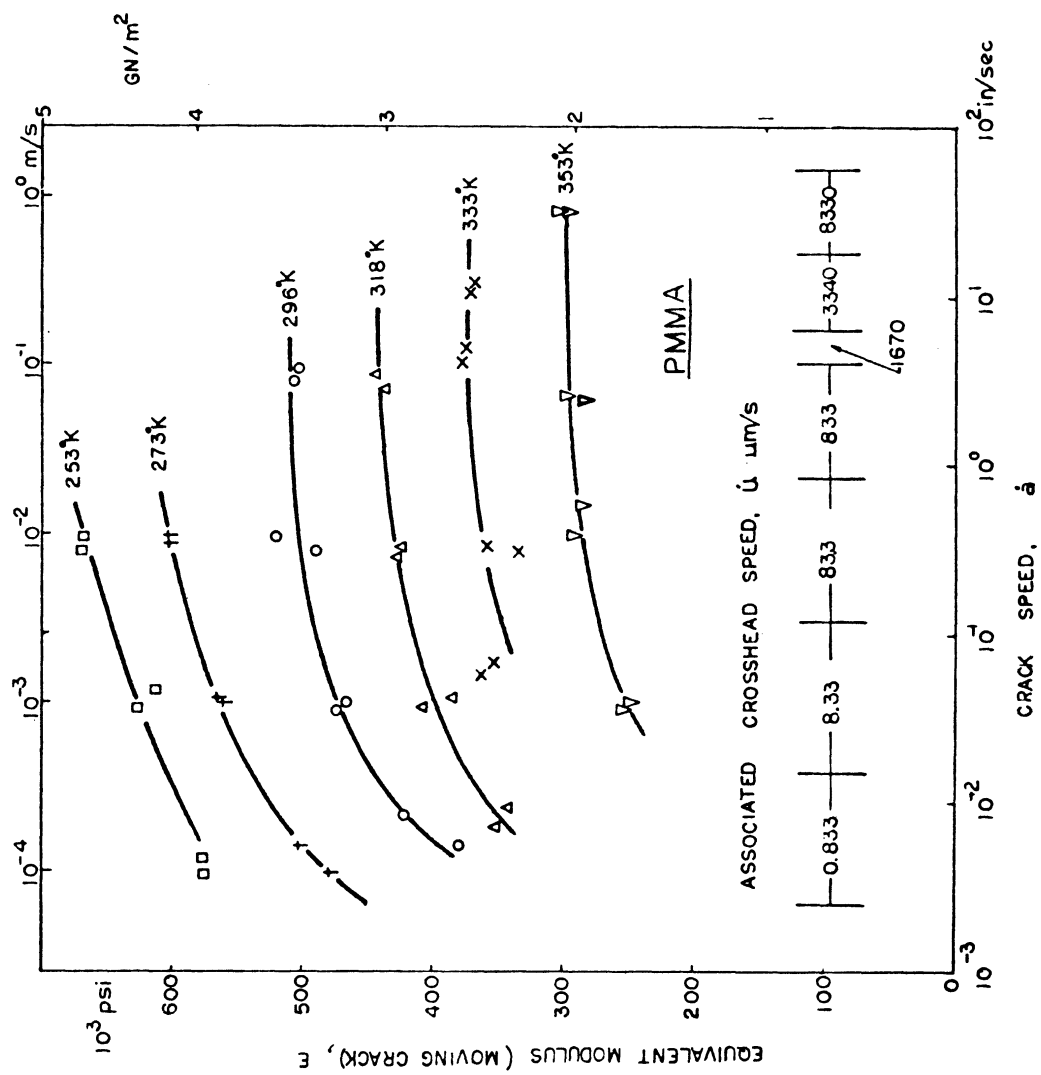


Figure 49. Equivalent Young's modulus for the moving crack

various test temperatures. Each neighboring pair of data points was obtained from a single fracture test with an associated crosshead speed (see Figure 47), with higher crack speed being associated with higher crosshead speed. Thus each pair of data points is associated with each decade of crosshead speed. Generally, the equivalent Young's modulus values increase more rapidly in a lower crack speed region (10^{-4} to 10^{-3} m/s), and level off to a slow rate of increase as the crack speed increases further.

IV.4.3.3 Comparison of equivalent Young's modulus for a stationary crack and a moving crack

The equivalent Young's modulus of a PMMA fracture specimen may change from one measured when the crack is stationary to one measured when the crack is moving (see Figure 47a and b). This change in modulus value is expected because the equivalent strain rate at the crack tip is considered to be substantially lower for a stationary crack compared to one for a moving crack (Williams 1972). Williams predicted the equivalent modulus value based on the strain rate at the crack tip of a moving crack, without any experimental evidence. In the previous two sections, the experimental modulus values of fracture specimens were obtained from an independent method without resort to the strain rate analysis by Williams.

A pair of equivalent modulus values of a moving crack

can be compared with the equivalent modulus value of a stationary crack obtained during the same test (i.e. with a particular crosshead speed) by comparing the results from Figures 48 and 49. It can be noted that in the temperature range of 296 °K to 353 °K, the equivalent modulus of a fracture specimen remains essentially the same, before and after the crack starts. This is quite surprising because the strain rate experienced at the stationary crack tip is considered to be substantially lower than that at the moving crack tip (Williams 1972), with the associated equivalent modulus value expected to be substantially higher for the moving crack. The present experimental results are quite different from the expected values based on the strain rate estimation given by Williams. In Figure 50, Williams' calculated results of equivalent modulus of a moving crack is compared with the present experimental results, both at room temperature. The calculated results by Williams are not only substantially higher than the present experimental results, but also they show a higher crack speed dependency. It is clear that the equivalent modulus value of a fracture specimen would be overestimated if it is determined by using the strain rate value at the crack tip as a representative strain rate for a fracture specimen as a whole.

Significant differences of two equivalent moduli (before and after the crack initiation) are observed in the lower temperature range, i.e., 273 °K and 253 °K in Figures

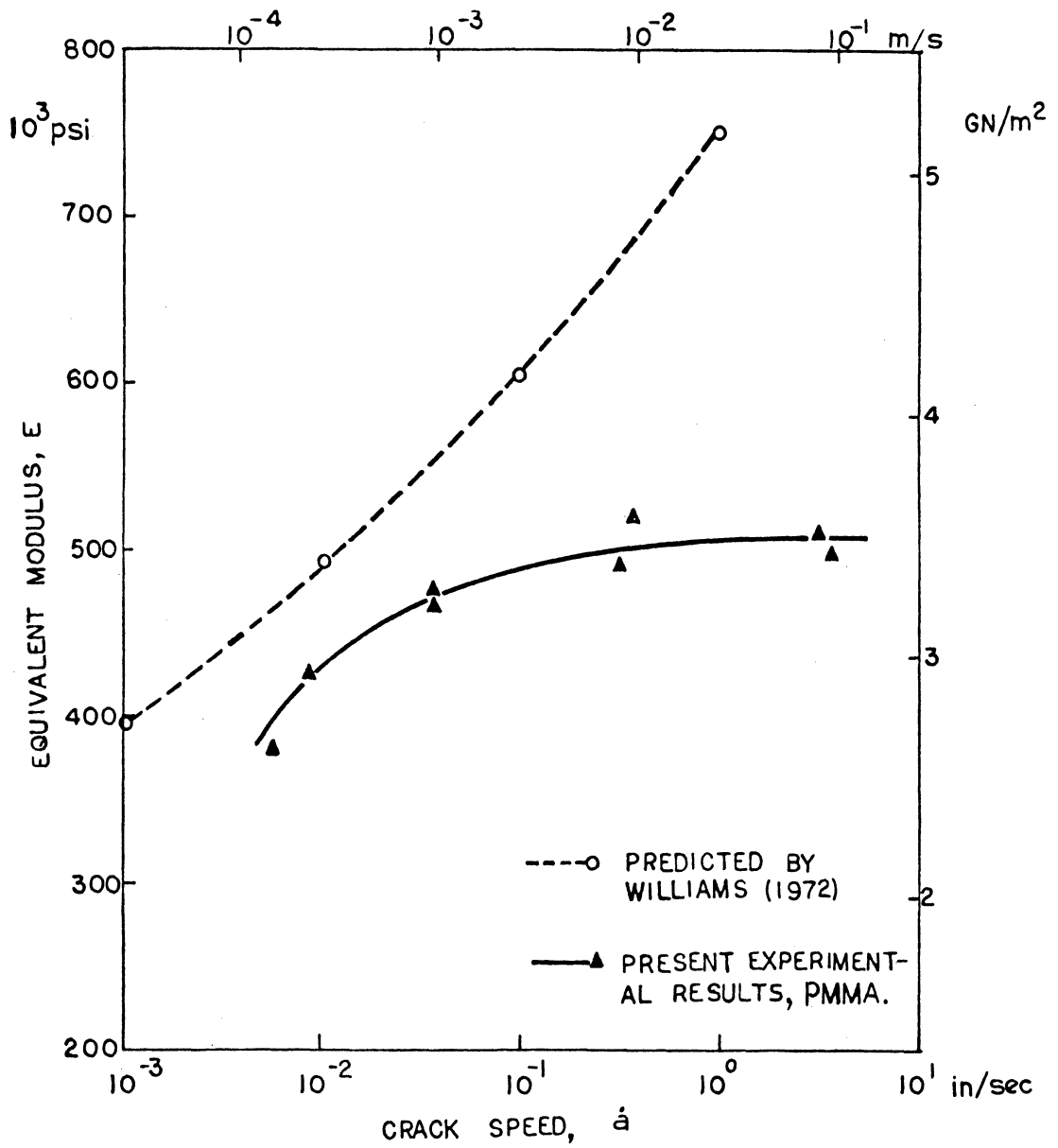


Figure 50. Comparison of equivalent Young's moduli from present experiments vs. predicted values by Williams (1972)

48 and 49. In this lower temperature range, the two modulus values are essentially the same when the crosshead speed and the associated crack speed are small. But as the crosshead speed increases the modulus values during crack propagation (moving crack) are consistently higher than those measured during the initial loading period (stationary crack). This difference in the equivalent modulus values during a single test might be affecting the crack stability (Gurney and Mai 1972), making it difficult for stable crack propagation in this lower temperature range (described in section IV.3.1.2). The crack stability parameter can be evaluated from the actual stiffness data measured during the actual fracture tests. The effect of change in equivalent modulus during a single fracture test on the stability of crack propagation is left here for a further study.

CHAPTER V
FRACTURE SURFACES OF PMMA AND PC

V.1 PMMA

Figures 51 through 54 show the fracture surfaces of PMMA at various temperatures and crosshead speeds. Fracture surfaces in each figure are those tested at one crosshead speed: 8.33 $\mu\text{m/s}$, 83.3 $\mu\text{m/s}$, 833 $\mu\text{m/s}$ and 8.33 mm/s , respectively. The fracture surfaces were gold-coated to provide better reflection from the otherwise transparent PMMA fracture surfaces. Heavy coating caused a glare from the fracture surfaces, but a light coating of the surface (half transparent) was sufficient to observe all the features of the fracture surfaces. Sometimes the coated gold film disintegrated under the influence of heat from the prolonged operation of the "coater". As an example, the fracture surface corresponding to 833 $\mu\text{m/s}$ speed at 353 $^{\circ}\text{K}$ (see Figure 53), looks rough due to such a broken appearance of an otherwise smooth fracture surface.

The smooth, featureless region marked as "U" corresponds to an unstable crack extension (a sudden load drop at a constant displacement in the load displacement curve of a fracture test). This unstable crack extension is arrested at each location where a distinct line appears on the fracture surfaces. The following crack extension after the arrest may be followed by either a stable crack or another unstable crack extension, depending on the temperature and

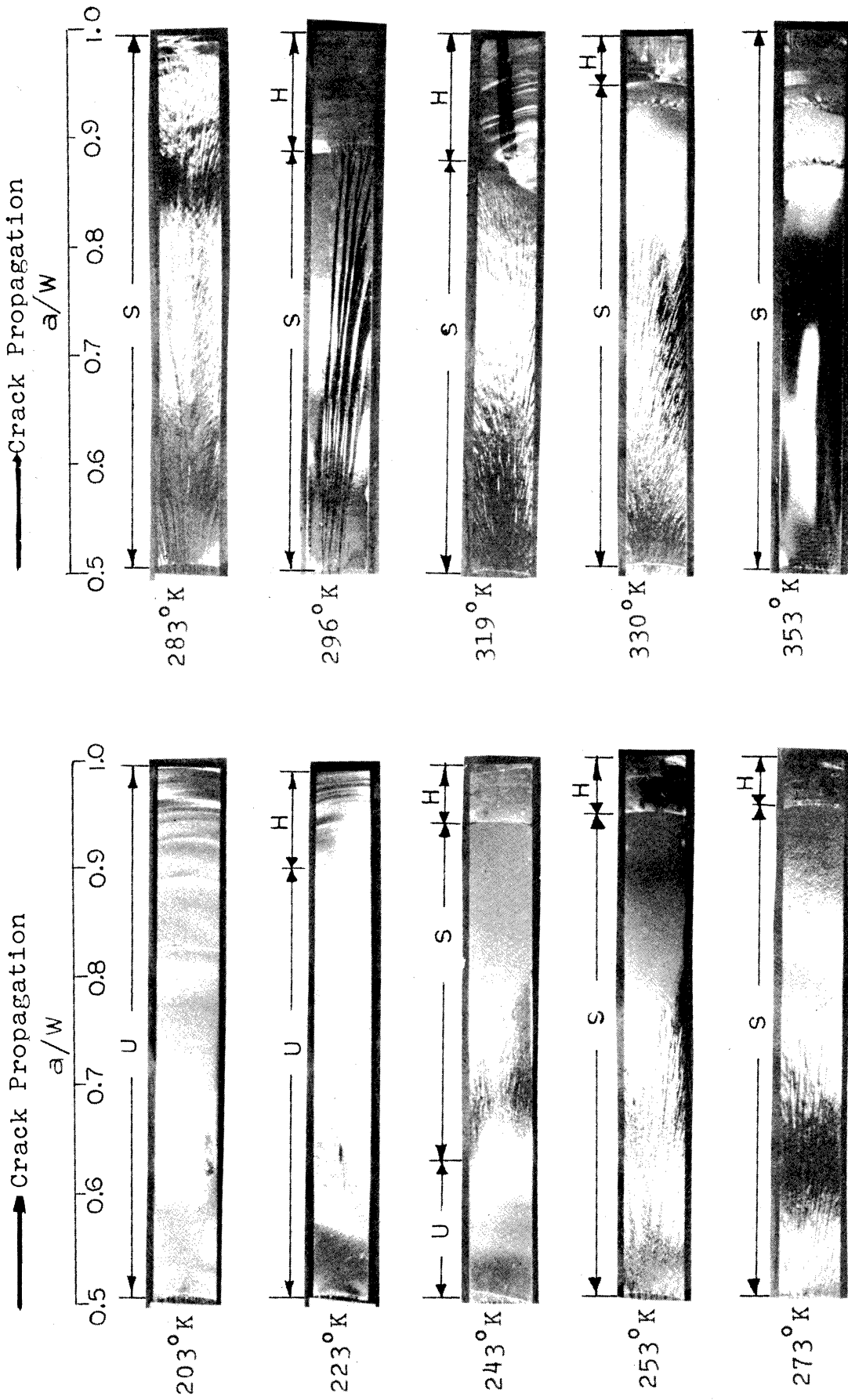


Figure 51. Fracture surfaces of PMMA tested at the crosshead speed of 8.33 $\mu\text{m/s}$

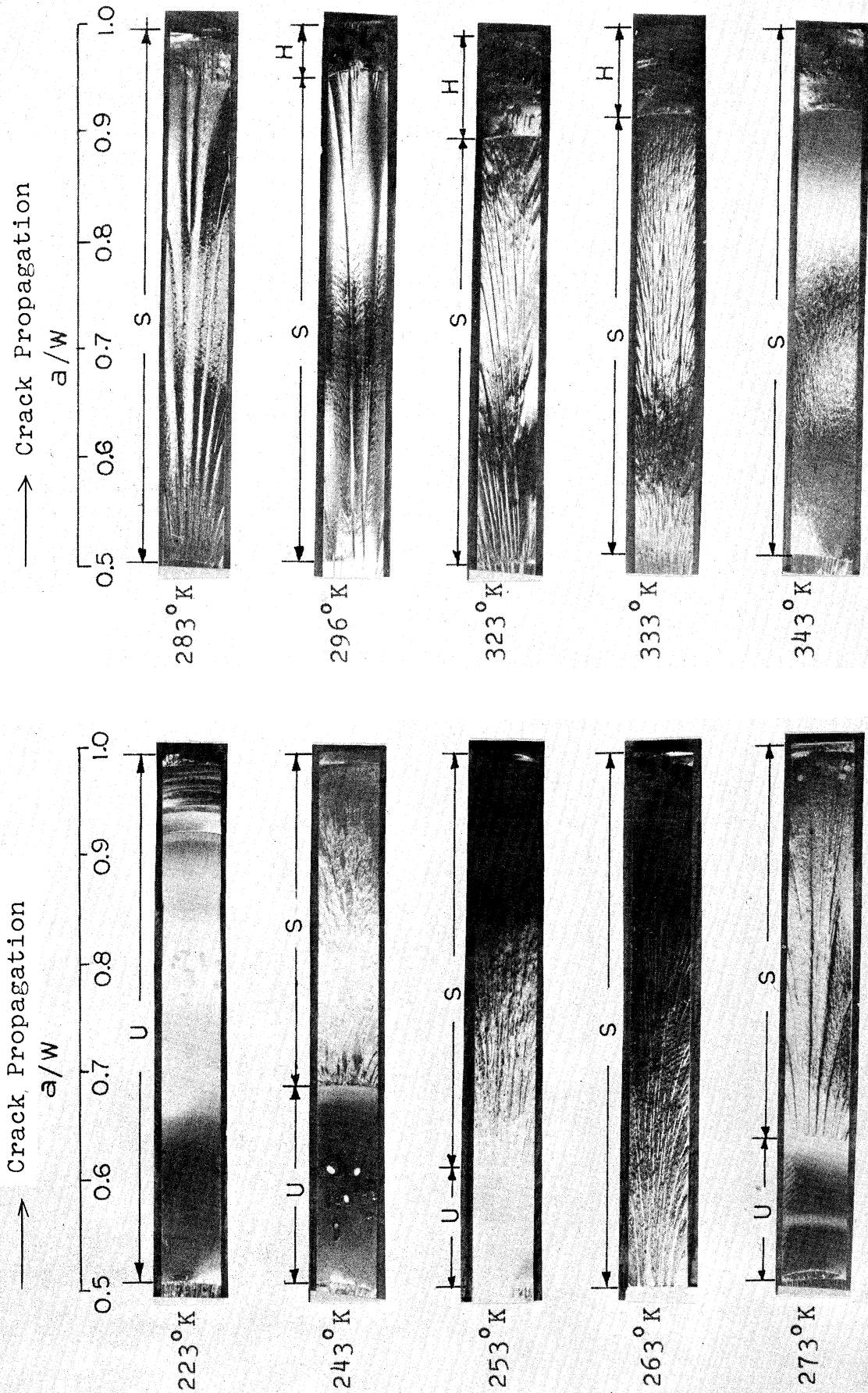


Figure 52. Fracture surfaces of PMMA tested at the crosshead speed of 83.3 $\mu\text{m/s}$

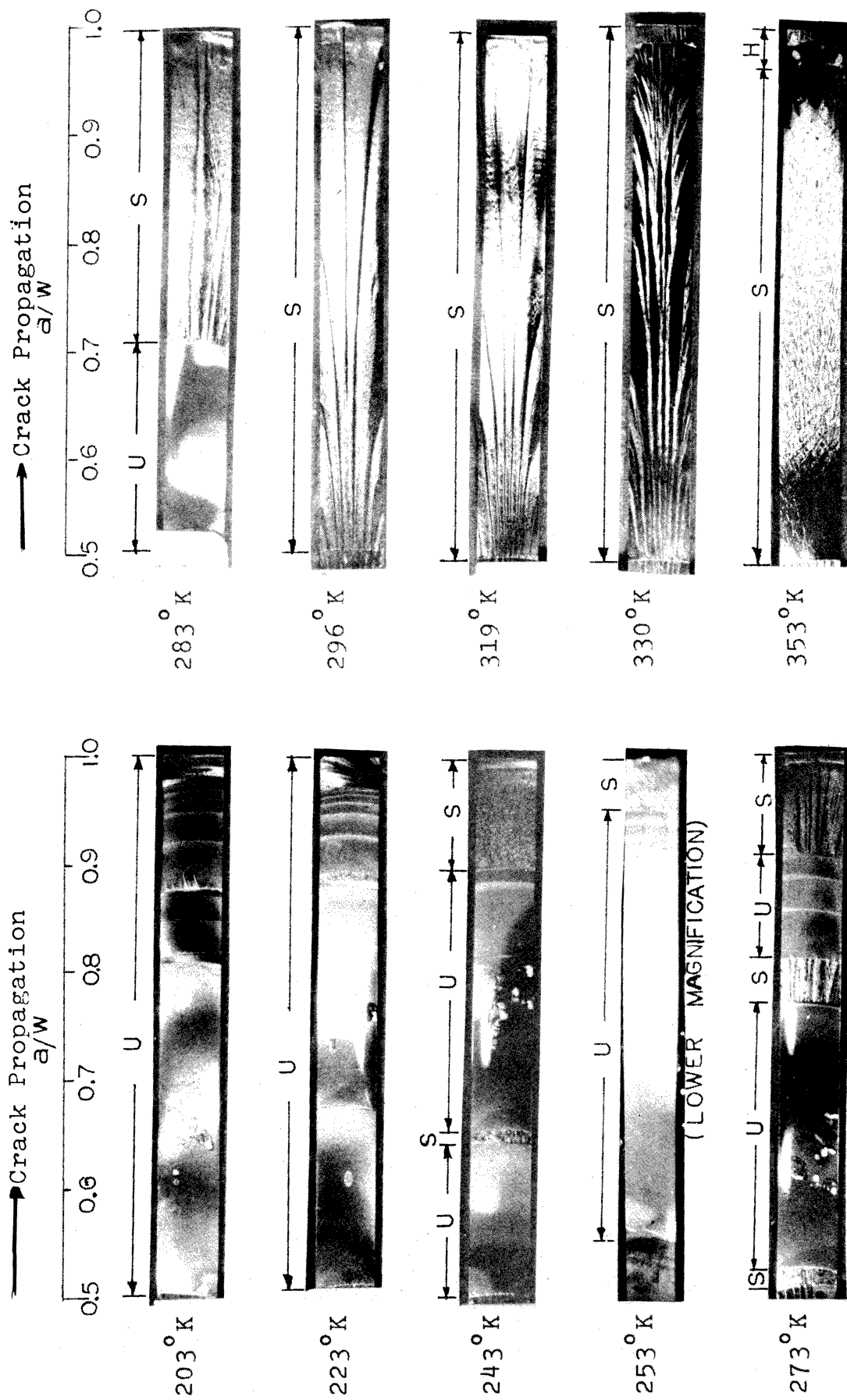


Figure 53. Fracture surfaces of PMMA tested at the crosshead speed of 833 $\mu\text{m/s}$

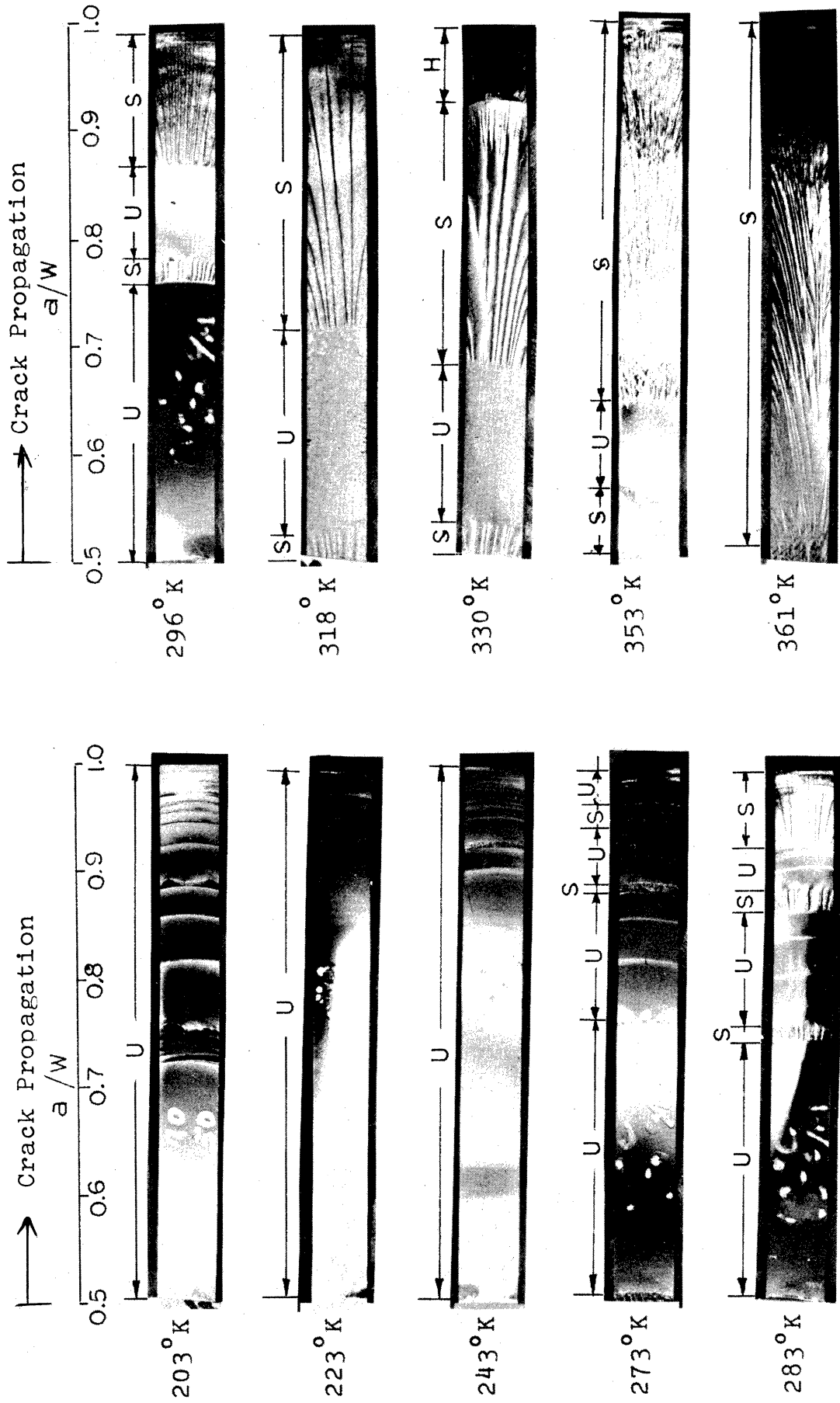


Figure 54. Fracture surfaces of PMMA tested at the crosshead speed of 8.33 mm/s

the crosshead speed applied. Generally, fracture at lower temperature and higher crosshead speed showed higher tendency for consecutive unstable crack extensions. As the temperature increases, the extent of unstable crack propagation region diminishes and the stable crack follows this unstable region. The stable crack propagation region is marked as "S" in the figures. Sometimes the fracture tests were interrupted before the crack reached the end of the specimen. The region marked "H" corresponds to the fracture surface generated by parting the specimen by hand after the test was interrupted.

Figure 55 shows the approximate demarcation line between stable and unstable regions as a function of crosshead speed and temperature. For example, if a fracture test was made (with a specimen having the geometry shown in Figure 16) at 273 °K using the crosshead speed of 833 $\mu\text{m/s}$ (5 cm/min.), the crack will be initially unstable until it is arrested at $a/W=0.8$; it then follow stable crack propagation. Figure 55 can provide an approximate guide for the choice of crosshead speed and initial crack length to obtain stable crack propagation at a given temperature (Note that Figure 55 is based on the natural, sharp cracks. If blunt cracks are used, an unstable crack may start even in the region where stable crack propagation is predicted in Figure 55).

The crack speeds associated with each fracture surface can be obtained from Figure 56, where crack velocities are plotted as a function of crack length for each

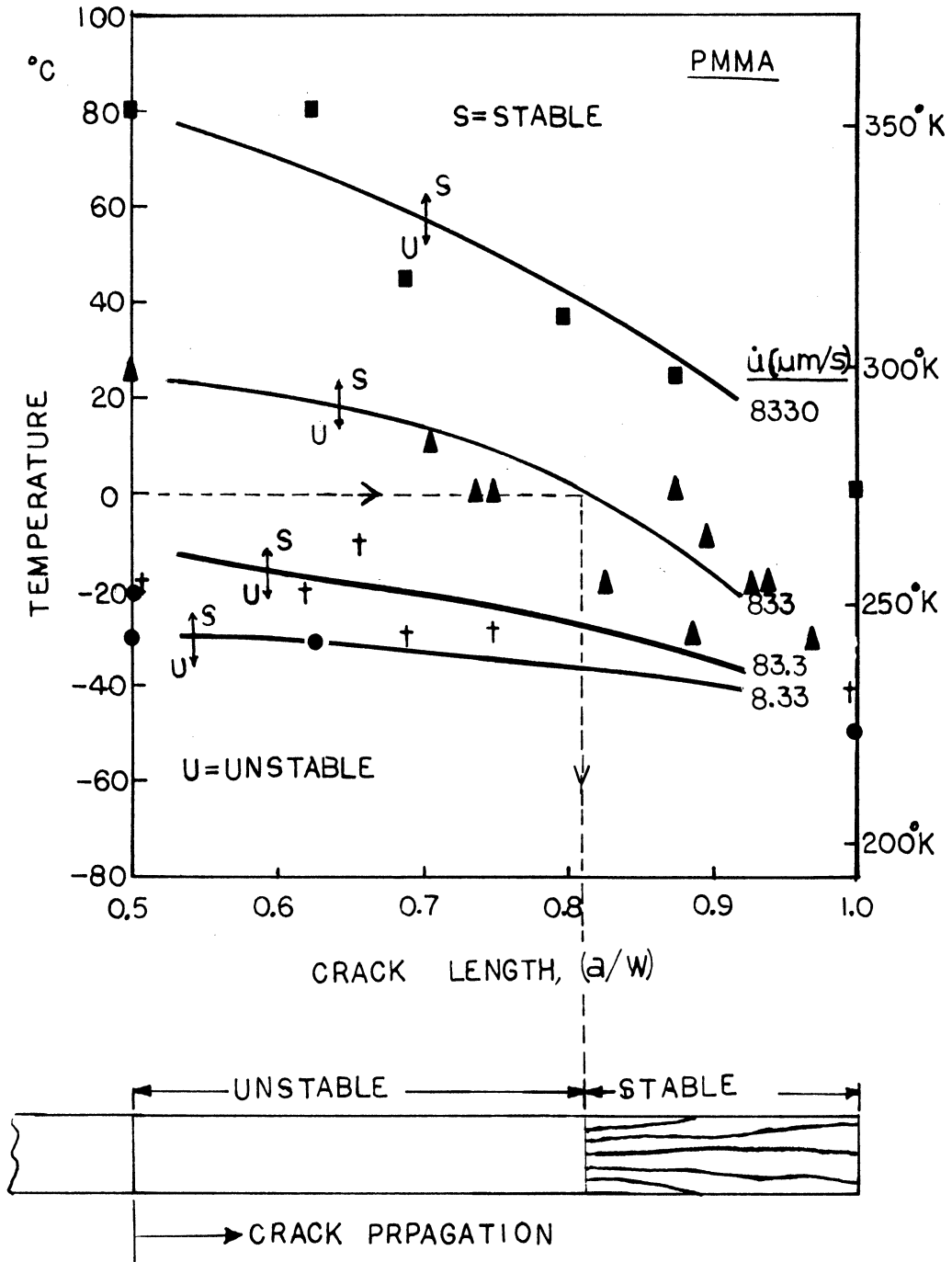


Figure 55. Approximate demarcation between unstable and stable crack growth as a function of temperature, crosshead speed and crack length. Dotted lines relate to example discussed on the previous page

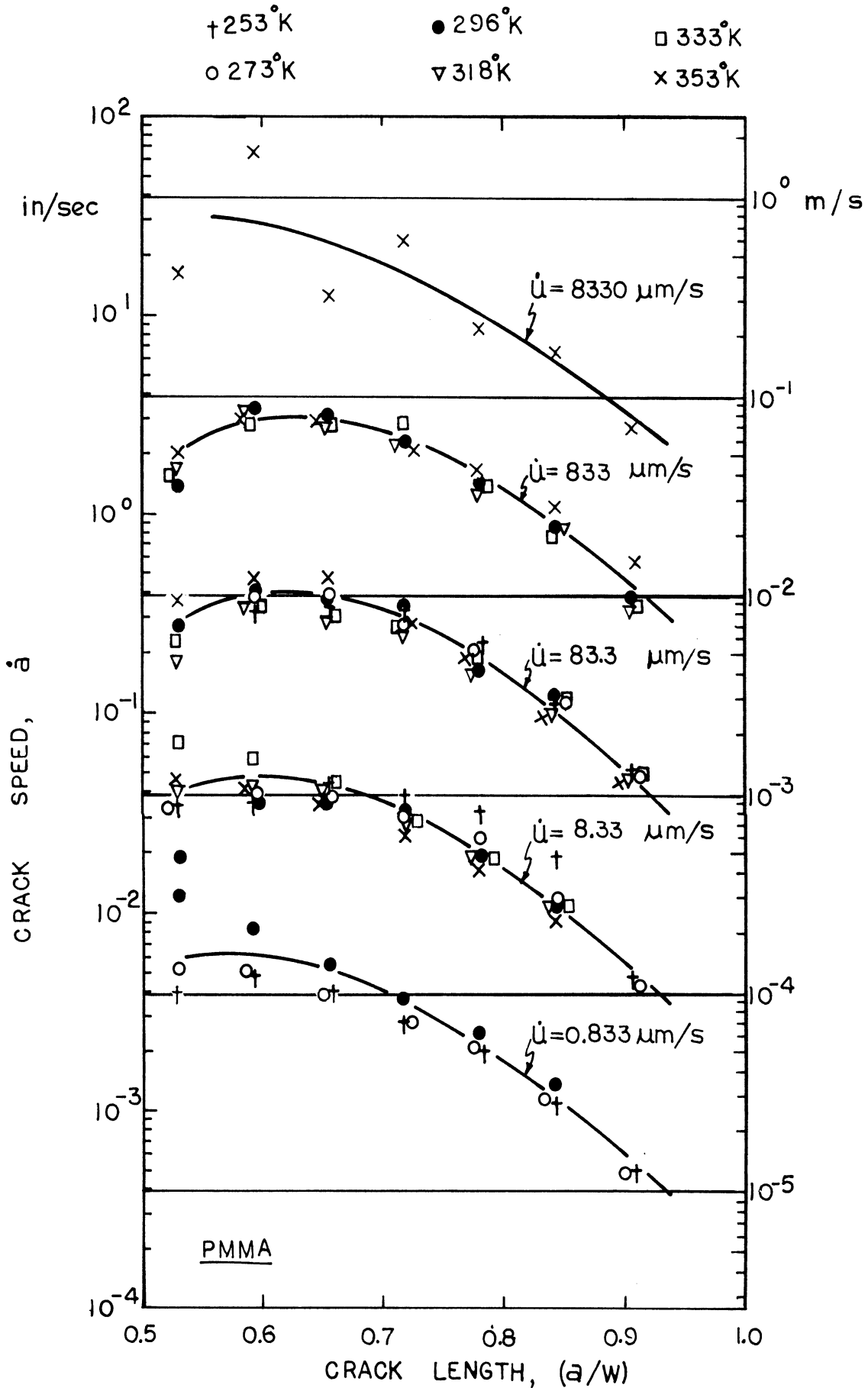


Figure 56. Crack speed vs. crack length for various crosshead speeds used

crosshead speed used. The crack speeds represented in Figure 56 apply to the stable crack propagation region only. The crack speeds for the unstable regions were not measured except for one which is shown in the previous chapter (see Figure 38). The influence of temperature on the crack speed is insignificant compared to that of crosshead speed and crack length, thus, a single line was drawn to represent the crack speed as a function of crack length for each crosshead speed applied.

The general characteristics of PMMA fracture surfaces are that they are smooth at very low crack speeds and they become rougher at increasing crack speeds. When the crack speed increases further, fracture mode suddenly changes to a high speed, unstable propagation. The threshold crack speed for initiation of this unstable crack propagation varies with temperature, as described in section IV.4.1.1. (Also see Figures 29 through 37). The fracture surfaces associated with the unstable crack propagation show very smooth surfaces, again. (Present observation is limited to the crack speed up to 230 m/s which is the fastest crack speed measured at room temperature. Cotterell (1965) reported that the fracture surface of PMMA become very rough when the crack speed exceeds 540 m/s).

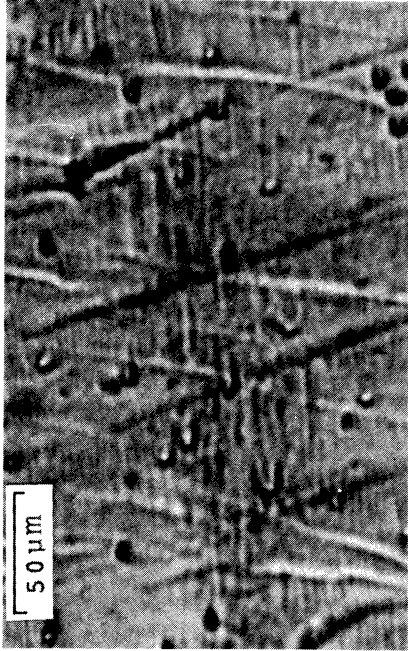
For example, the fracture surfaces of PMMA obtained at room temperature (see Figure 34) show flat and smooth surfaces in the crack speed range around $\dot{a}=10 \mu\text{m/s}$. As the crack speed increases they become rougher, making several

rib markings along the crack propagation direction. Further increases in crack speed above ~ 100 mm/s, causes unstable crack propagation and the surfaces corresponding to this unstable crack propagation region become flat again. The two types of flat fractures, i.e. one generated at very slow crack speed and one generated at very high crack speed, can be distinguished under the microscope. Fracture surfaces shown in Figure 57 have been obtained from both extremes of crack speed ranges, i.e. very slow and stable and very fast and unstable regions at the temperature marked in each figure. All of the fracture surfaces in Figure 57 look smooth to the naked eye, but when they are viewed through the microscope (at 70X) the smooth (flat) surfaces of high speed, unstable fracture show conic markings. Those obtained at very slow, stable crack speed do not. Fracture surfaces at very slow crack speed show several lines which lie across the propagation direction and also some dimple marks scattered around the fracture surface. More detailed discussions are given in the following sections.

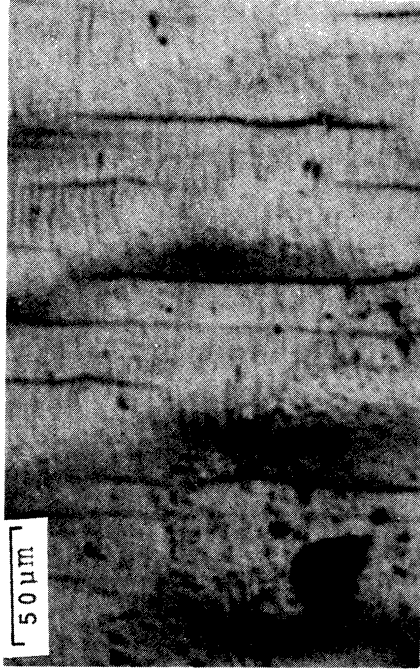
5.1.1 Fracture surfaces in the unstable crack propagation region

The conic markings on the fracture surfaces of unstable crack propagation are formed from the interaction between the primary crack front and the secondary cracks generated ahead of the crack front. A schematic representation of the primary crack front is given in Figure 58. The nucleus of the secondary crack, P, lies at a distance from

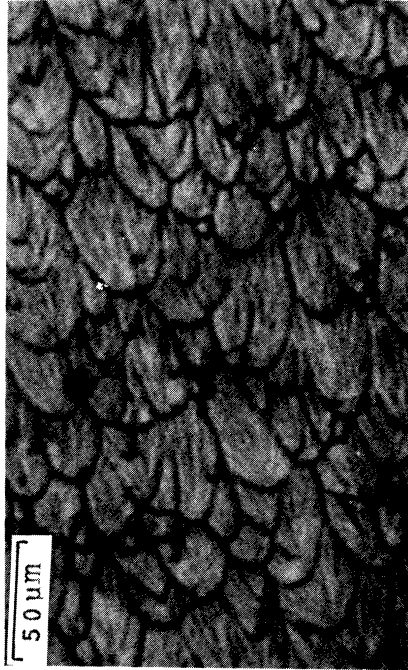
Crack Propagation →



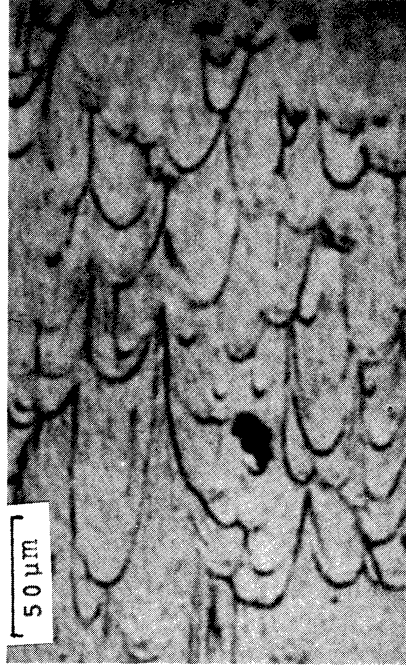
Slow, Stable Cracking
at 273 °K



Slow, Stable Cracking
at 296 °K



Fast, Unstable Cracking $\frac{1}{2}$
at 273 °K ($K_{IC}=1.75 \text{ MN/m}^{\frac{3}{2}}$)



Fast, Unstable Cracking $\frac{1}{2}$
at 296 °K ($K_{IC}=1.52 \text{ MN/m}^{\frac{3}{2}}$)

Figure 57. Difference in microscopic features of slow stable fracture and fast unstable fracture at 273 °K and 296 °K for PMMA

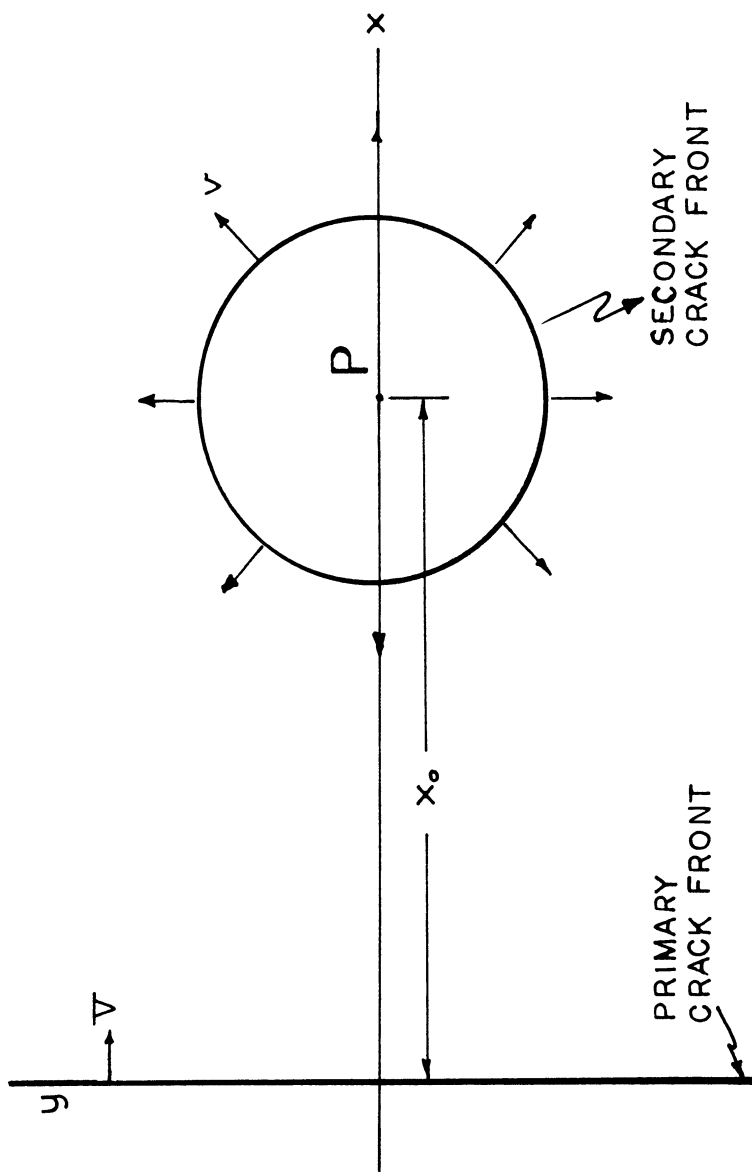


Figure 58. Schematic diagram showing the primary crack front and secondary crack front

the primary crack front. The primary crack moves at speed V , while the secondary crack radiates in the x - y plane at the speed, v . The locus of the intersection of two crack fronts can be found from (Andrews 1968);

$$x = Vt \quad (5.1)$$

$$(x - x_0)^2 + y^2 = (vt)^2 \quad (5.2)$$

which reduces to

$$x^2 \left\{ \left(\frac{v^2}{V^2} \right) - 1 \right\} - y^2 = x_0 (x_0 - 2x) \quad (5.3)$$

By introducing the crack speed ratio $n=v/V$ into equation (5.3),

$$x^2 (n^2 - 1) - y^2 = x_0 (x_0 - 2x) \quad (5.4)$$

This is the equation of a conic, which reduces to a parabola when $n=1$, an ellipse when $n<1$, and a hyperbola when $n>1$. A detailed discussion is given in Appendix III.

$n=1$: Parabola

$$x = \frac{1}{2x_0} y^2 + \frac{x_0}{2} \quad (5.5)$$

$n<1$: Ellipse

$$\frac{\left(x - \frac{x_0}{1-n^2}\right)^2}{\left(\frac{nx_0}{1-n^2}\right)^2} + \frac{y^2}{\left(\frac{nx}{\sqrt{1-n^2}}\right)^2} = 1 \quad (5.6)$$

$n > 1$: Hyperbola

$$\frac{\left(x + \frac{x_0}{n^2-1}\right)^2}{\left(\frac{nx}{n^2-1}\right)^2} - \frac{y^2}{\left(\frac{nx_0}{\sqrt{n^2-1}}\right)^2} = 1 \quad (5.7)$$

The general term, "conic marking", will be used hereafter to describe parabolic, elliptical and hyperbolic markings on the fracture surface.

The conic markings evident in the early part of the unstable propagation region gradually disappear as the crack advances further away from the initial crack tip until the crack is arrested. Figure 59 shows the changing features of the fracture surface as the unstable crack advances in a "jerky" manner. Initial conic markings (a) gradually change to a more granular shape (b) and granular feature dominates up to the arrest point. When the unstable crack starts again at the arrest point, densely populated conic markings (c) appear again. The granular feature appears consistently just ahead of every arrest point on most of the fracture surfaces of unstable propagation.

It is noted that the density of the initial conic markings is dependent on the initial K_{IC} level and the in-

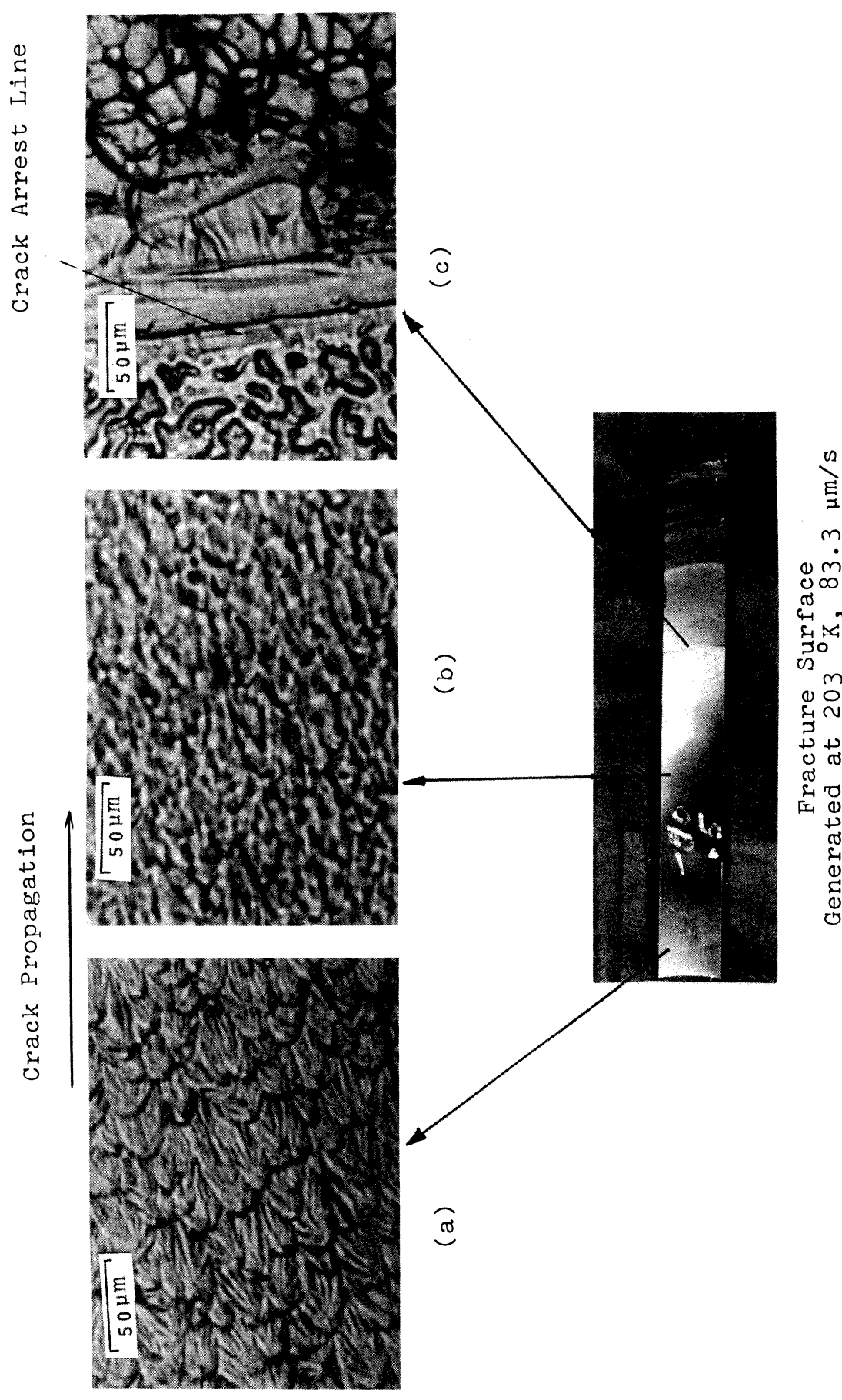


Figure 59. Microscopic view (70X) of an unstable fracture surface of PMMA at various locations

initial K_{IC} depends on temperature, crosshead speed and crack tip geometry (sharp or blunt). Figure 60 shows the conic markings near the initial cracks started at different levels of K_{IC} values. It is evident from the pictures that the density of conic markings is higher for the fracture surfaces started at higher K_{IC} level. Note that K_{IC} decreases from Figure 60a through 60d in sequence. Similar correlations between the density of conic markings vs. fracture toughness has been reported by Cotterell (1968). Cotterell postulated that the secondary crack starts at the voids in the craze material, which is composed of 50~60% polymer by volume and voids in the remaining volume (Kambour 1972). Cotterell observed that the thickness of craze may increase with increasing fracture toughness and this increase in craze material provides more nucleation sites for secondary cracks, resulting in higher density of conic markings. However, optical and electron microscopic study of fracture surface by Lednický and Pelzbauer (1972) showed that the individual cavities in the foci of the conic markings had the diameter of $\sim 1 \mu\text{m}$, which is substantially larger than the diameter of an individual void in a craze material. Based on this observation they explained that the secondary fractures are initiated in the craze from the cavities (of about $\sim 1 \mu\text{m}$ in diameter) produced by a mutual joining of small holes (100 to 200 \AA) present in the polymeric material. Based on above theory of secondary crack formation, the change in conic markings density can be explained as: the crack speed increases with increasing

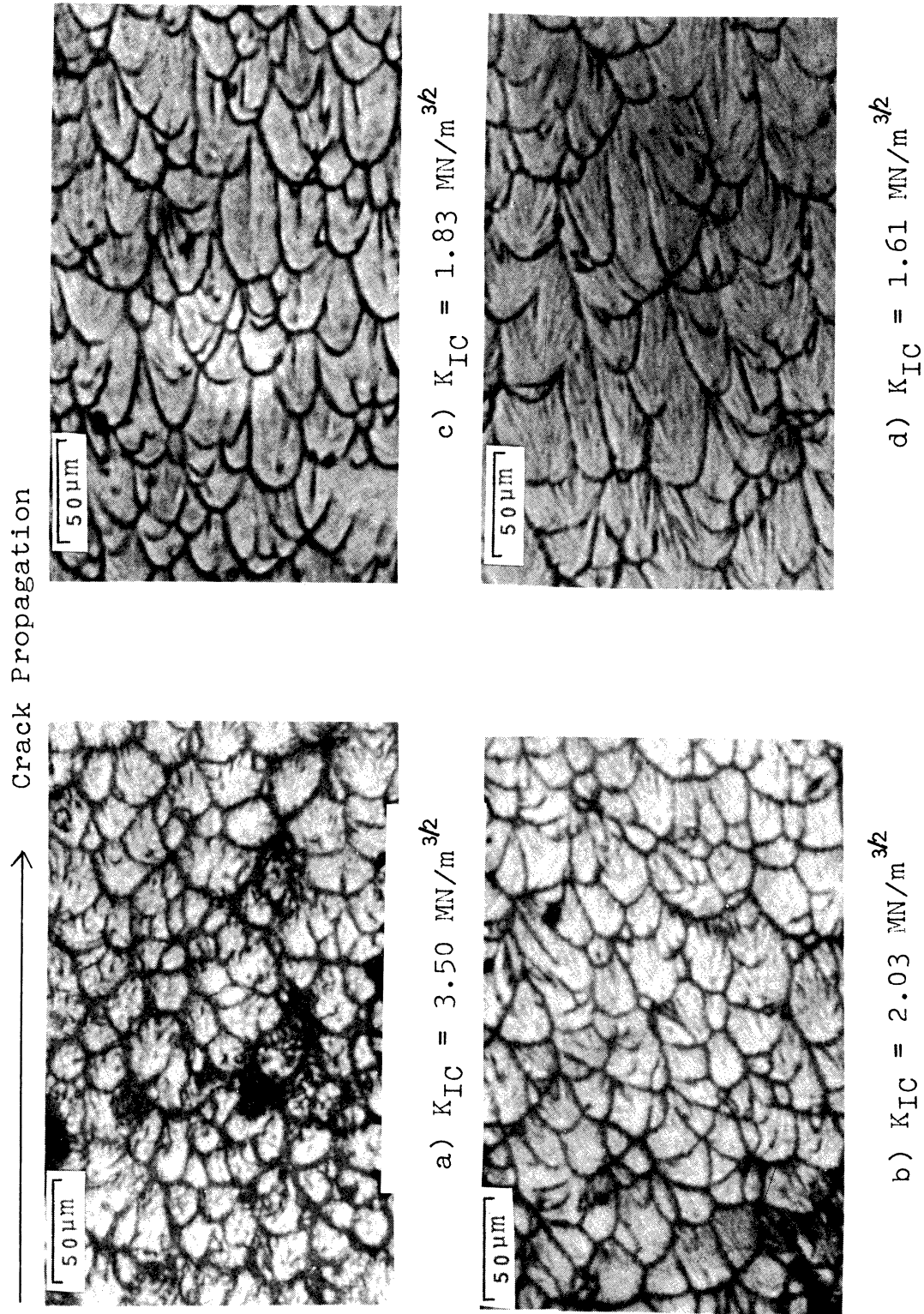
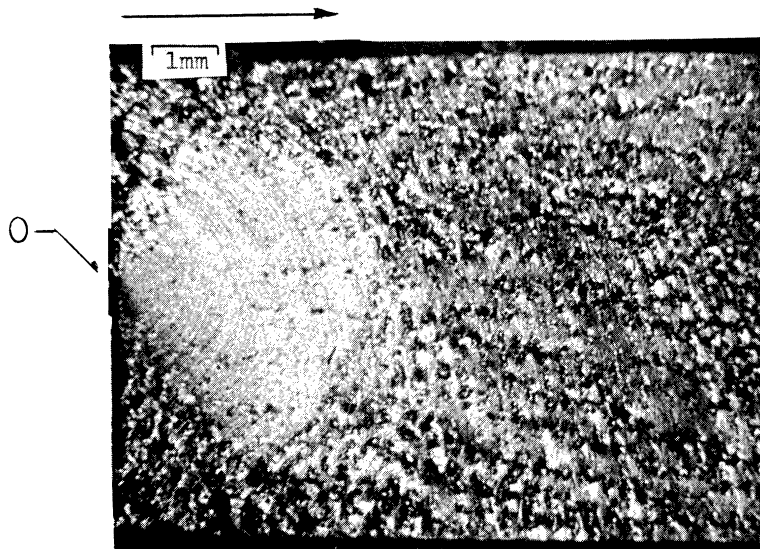


Figure 60. Variation of conic marking density and the associated K_{IC} values for PMMA

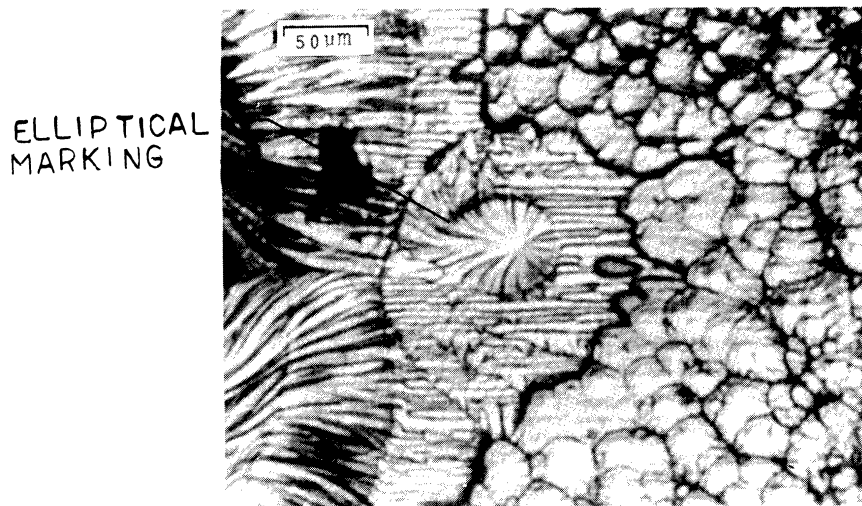
K_{IC} level (Cotterell 1968) and this increased crack speed provides only a limited time for the holes in the craze material to coalesce. Thus the total number of the effective secondary fracture nuclei increase with higher K_{IC} , leaving higher density of conic markings on the fracture surfaces. Another ramification of the Lednicky and Pelzbauer's theory of secondary crack formation is that the cavity size at the foci of the conic markings will vary as a function of K_{IC} level (or crack speed), because this cavity diameter is determined by the number of voids successfully coalesced during the crack propagation. This measurement of cavity diameter as a function of K_{IC} value may provide a means of testing the validity of Lednicky and Pelzbauer's explanation of secondary crack formations.

The fracture surface corresponding to a particular crosshead speed shows some interesting features. Figure 61 shows various aspects of the fracture surfaces resulting from pulling the specimen at $8.33 \mu\text{m/s}$ at 193°K . Fracture started at a point, 0, near the middle of the initial crack front where the highest stress is expected (Figure 61a). Figure 61b shows the magnified view (70X) of the fracture origin in Figure 61a and Figure 61c shows a magnified view (1000X) of some of the conic markings around the crack origin.

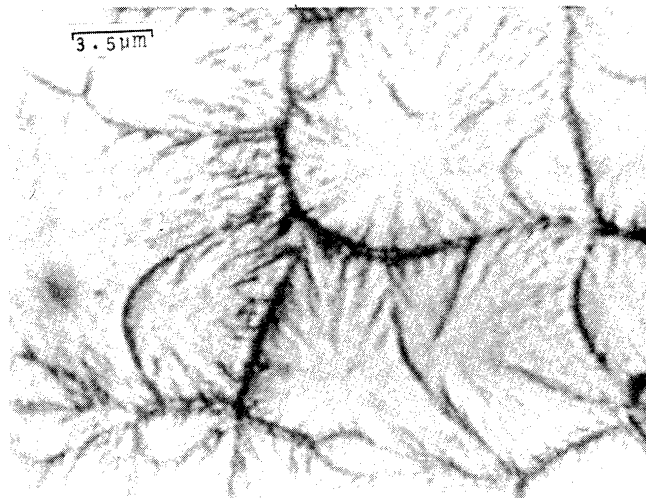
An elliptical marking is visible near the fracture origin in Figure 61b. This is the situation arising when the secondary crack speed is less than the primary crack speed ($n < 1$), resulting in an elliptical marking described by



(a)



(b)

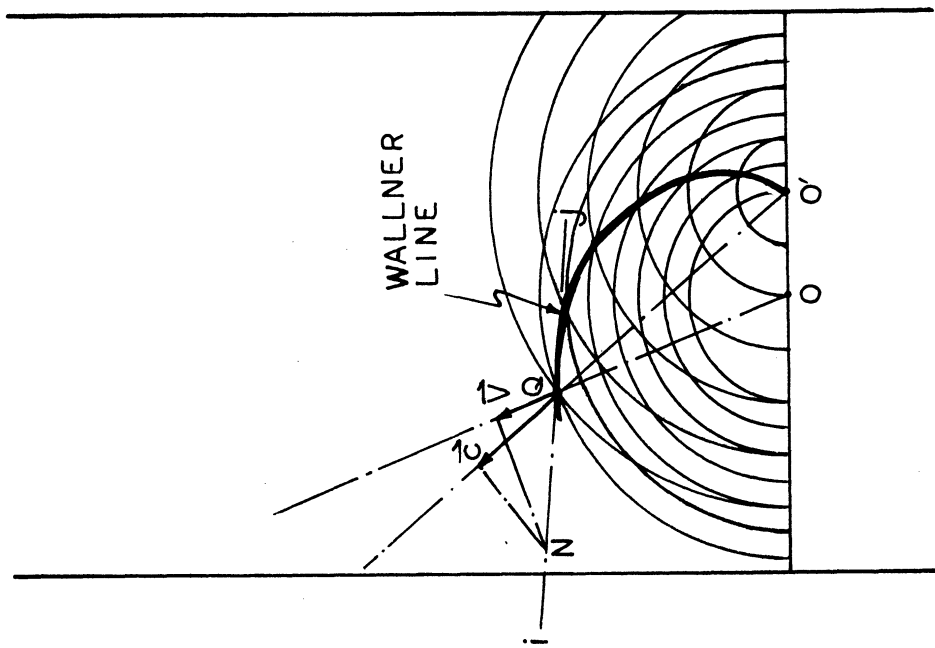


(c)

Figure 61. Fracture surface of PMMA fractured at 193 °K

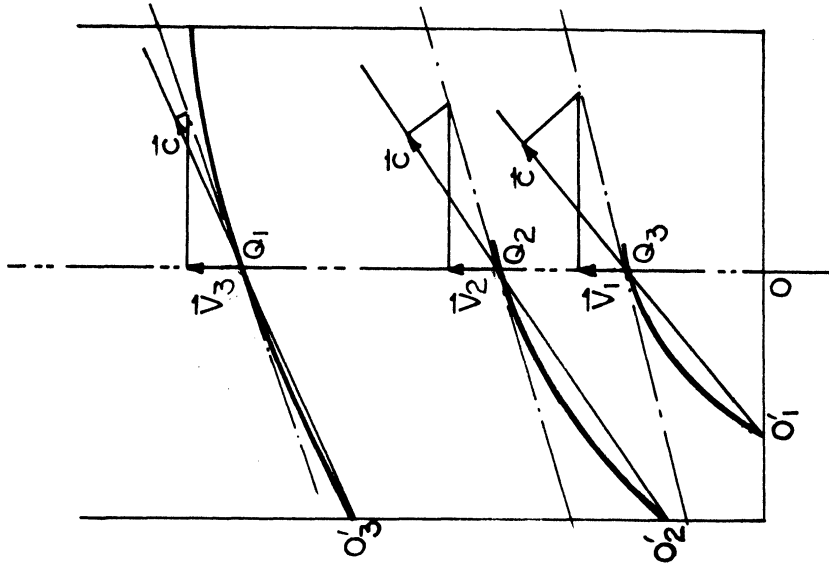
equation (5.6). The secondary crack origin lies at the right hand side with respect to the center of the ellipse. The location of the secondary crack nucleus suggests that the primary crack started from the right hand side of the ellipse, rather than from the left hand side where the main crack front lies. This can be analyzed from the equation of an ellipse as given in equation (5.6). The location of the center of the ellipse, from equation (5.7), is $x = \frac{x_0}{1-n^2}$ and $y=0$ (see Appendix III). x_0 is the distance between the secondary crack nucleus and the primary crack front as shown in Figure 57. Since $n < 1$ (from the fact that the loci is an ellipse), the center of the ellipse will be located at the opposite side of the primary crack front with respect to the secondary crack nucleus (because $\frac{x_0}{1-n^2} > x_0$). Figure A.3.2 in Appendix III shows the schematic diagram describing the situation. Since the ellipse in Figure 61b has its center at the left side of the secondary nucleus, it follows that the "primary" crack must have started at the right side of this ellipse. It then moved towards the left where it interacted with the secondary crack front, thereby forming an elliptical trace.

As the crack propagated from the origin, it formed "Wallner" lines which are evident in Figure 61a. The Wallner lines are formed from the interaction of the main crack front with those elastic waves released at the interface of the crack front and the outer boundary surface. Figure 62a illustrates the formation of Wallner lines (Wallner 1939). Fracture at



(a)

- O: CRACK ORIGIN
- O': SECOND FLAW WHERE ELASTIC WAVE WAS EMITTED
- Q: A POINT ON A WALLNER LINE
- \vec{t}_j : TANGENT TO WALLNER LINE AT Q
- \vec{c} : TRANSVERSE ELASTIC WAVE VELOCITY
- \vec{V} : CRACK SPEED



$|\vec{V}_1|=0.3|\vec{c}|, |\vec{V}_2|=0.3|\vec{c}|, |\vec{V}_3|=0.4|\vec{c}|.$

(b)

Figure 62. Formation of a Wallner line and estimated crack speed from the Wallner lines

first originated at the mid-point, O , of the original crack front. The crack then propagates radially (centered at O) with speed $|\vec{v}|$. As the propagating crack front meets with a second flaw on the boundary, a transverse elastic wave is generated at this point O' . This newly generated elastic wave will also propagate radially (centered at O') with the characteristic wave velocity $|\vec{c}|$. This wave will intercept the main crack front continuously as it moves forward. The disturbance at the intercept deflects the plane of the fracture surface. This surface undulation becomes visible as Wallner lines, shown as a heavy-lined curve $O'Q$ in Figure 62a. From the trace of Wallner lines one can construct the vector diagram describing the ratio between the crack speed and the elastic stress wave velocity (Smekal 1950). A tangent to a Wallner line at point Q , is shown as $i-j$ while OQ , $O'Q$ are the radial lines from the origin of crack and the origin of the elastic wave. If a line segment QN on the line $i-j$ is projected on the extrapolated lines of OQ and $O'Q$, respectively, it produces velocity vectors representing the directions and relative magnitude of crack speed to the elastic wave velocity. Figure 62b shows the vector diagram from the Wallner lines in Figure 61a. The elastic transverse wave velocity in PMMA at 193°K is ~ 1.5 km/s, thus the crack velocity associated with the fracture surface is estimated to be ~ 500 m/s.

The fan-shaped smooth region in Figure 61a shows a contrast with the remaining rough regions. Similar phe-

nomena were observed by Shand (1954) on the fracture surface of a rectangular glass bar broken in bending. Shand gave a qualitative explanation for the formation of such a distinct mark. As shown in Figure 63, the crack front at first advances radially making a half circle crack front. As the circular crack front increases its diameter the effective stress intensity factor along the centerline is reduced while the stress intensity factor away from the centerline increases due to the redistribution of stress caused by a reduced stress state along the centerline. This increase in stress intensity at both sides of circular crack causes the crack speed in this front region to accelerate at such a fast speed as to cause rough surfaces. Since the crack speed at the sides of the circular crack front is faster than at the middle of the circular crack front, the shape of the crack front changes from a circular shape to a flatter shape as shown in Figure 63. Dashed lines \widehat{de} and \widehat{ij} represent the circular crack front if the crack moves at uniform velocity. Solid lines \widehat{DE} and \widehat{IJ} represent the actual crack front shape. Line s-s' is an approximate dividing line between the low crack speeds which leave a smooth fracture surface and the high crack speed which leave a rough fracture surface. As the crack propagates far into the end region of the fracture specimen, the crack speed decreases and the fracture surface in this region becomes smooth again. The rough region in the same figure was viewed under an SEM; results are shown in Figure 64 a and b. The fracture surface

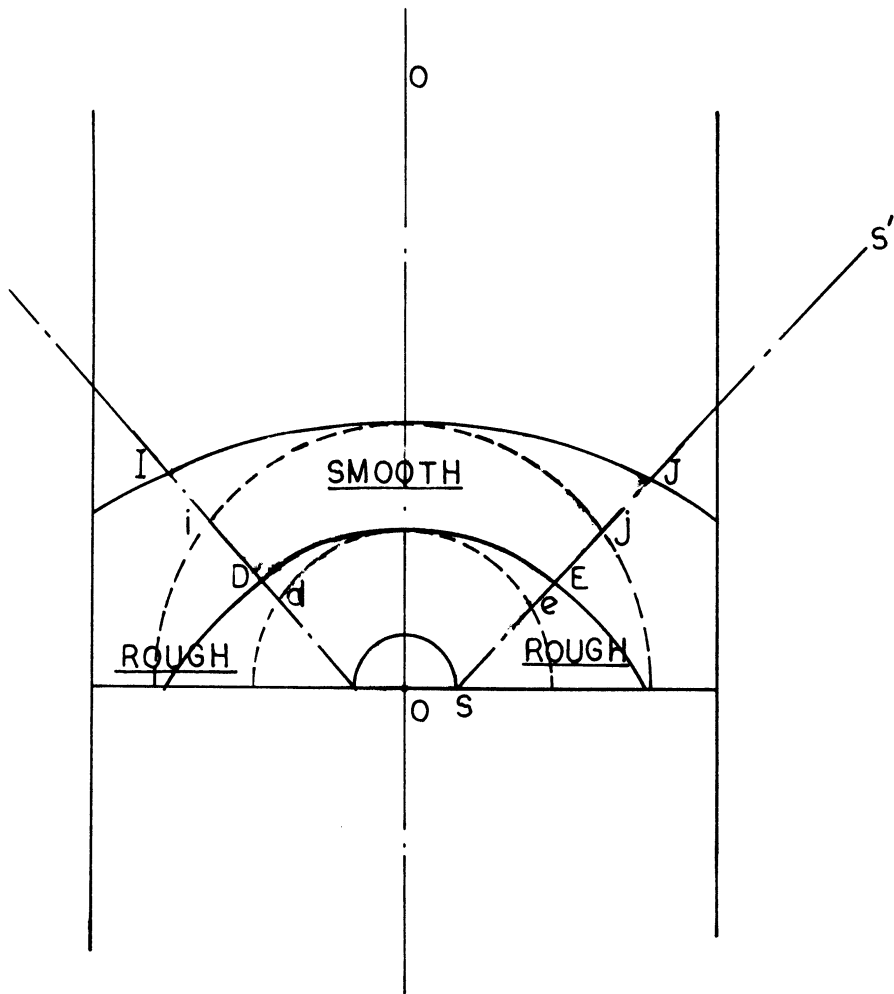
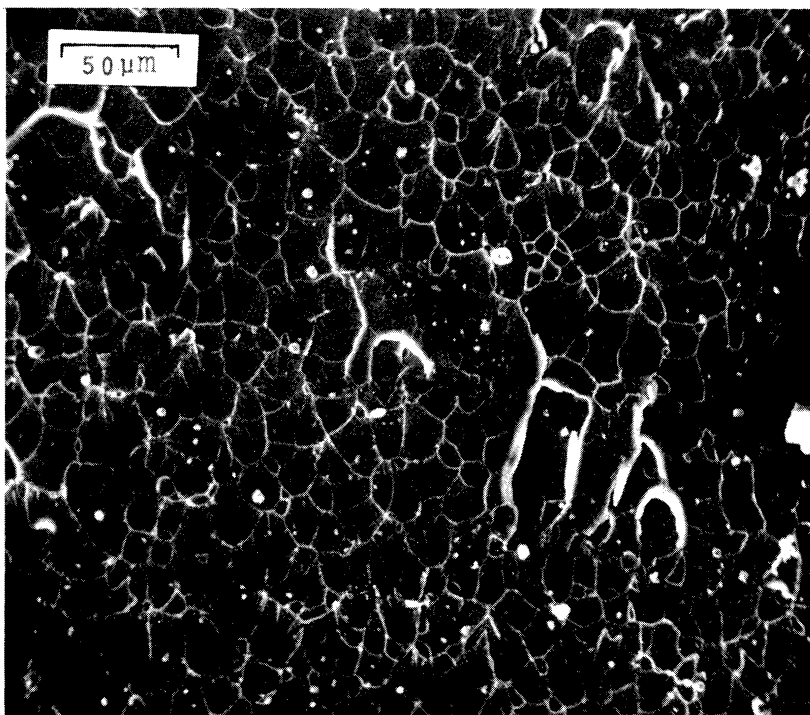
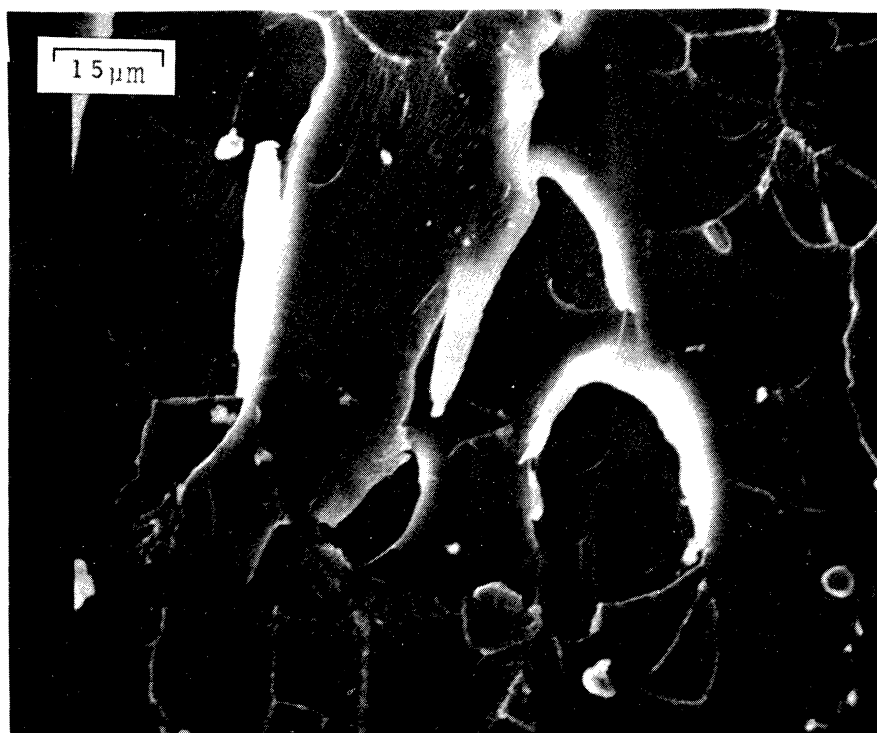


Figure 63. Qualitative explanation for a fan-shaped smooth region and rough surface outside the fan-shaped region, in Figure 61a



(a)



(b)

Figure 64. Rough region in Figure 61a viewed under SEM

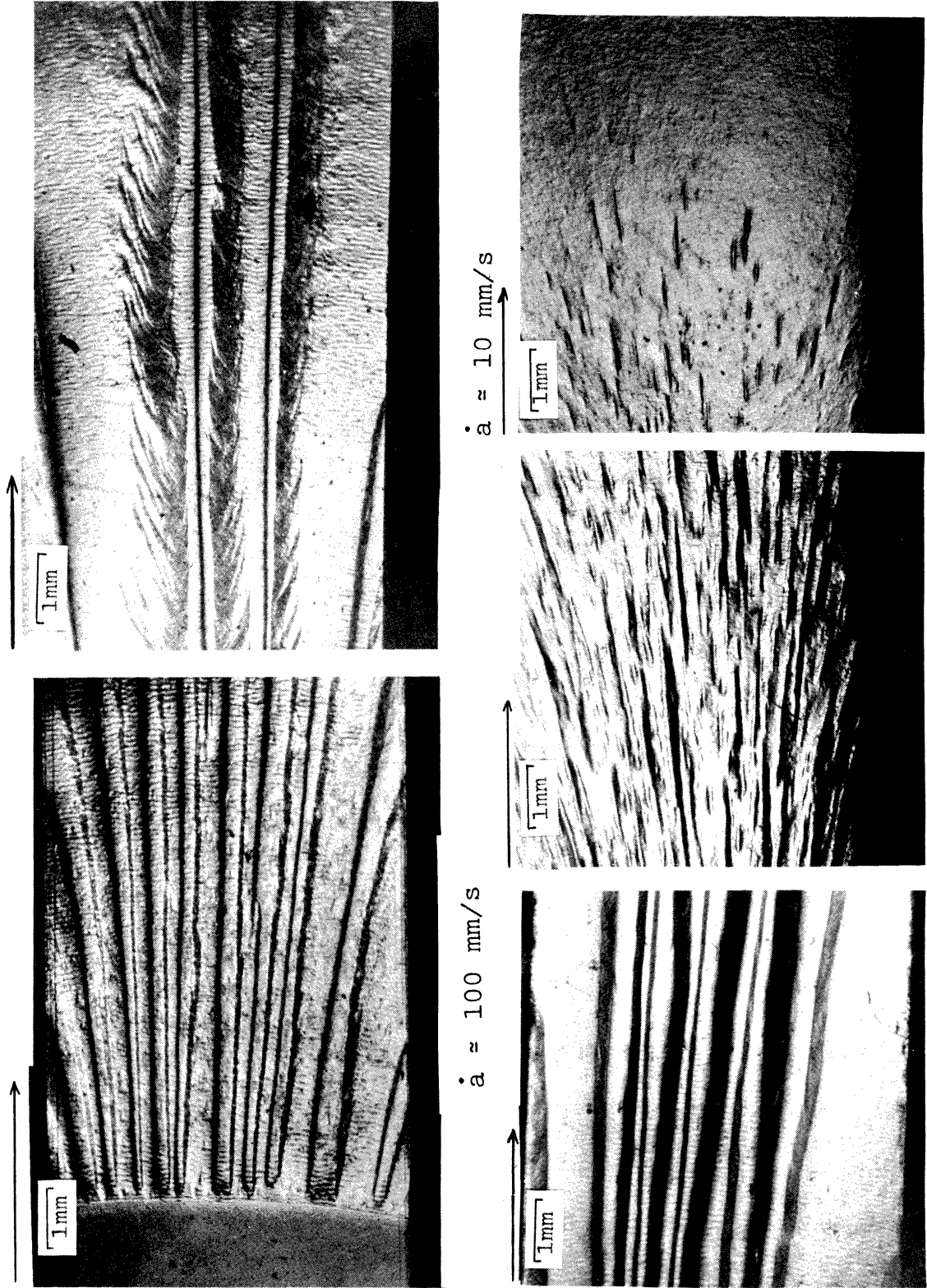
in the rough region shows part of the sub-surface exposed where some conic markings are also visible.

5.1.2 Fracture surfaces in the stable crack propagation region

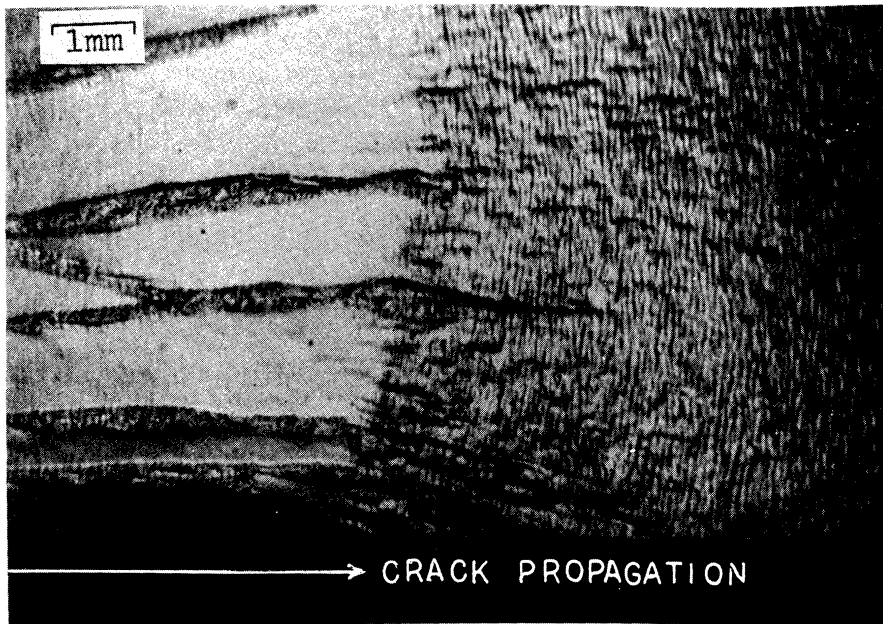
The fracture surfaces associated with stable crack propagation are shown in Figures 29 through 37. They are shown as a function of crack speed at each temperature tested. The lower crack speed at each temperature produced very smooth surfaces, while the fast but still stable region of crack speed at each temperature, produced rough surfaces with several rib-like markings running parallel to the crack propagation direction. These rib markings are coarse in the high speed region and they change to numerous needle-like markings as the crack speed decreases until they become flat with a smooth feature at the lower end of crack speed. Figure 65 shows typical characteristic features of stable fracture surfaces as a function of crack speed at room temperature.

The sudden decrease in fracture toughness above the crack speed of $\sim 100 \mu\text{m/s}$ at 243°K corresponds to the sudden change in the fracture pattern, shown in Figure 66a. A similar drop in fracture toughness above the crack speed of $\sim 0.5 \text{ m/s}$ at 353°K is also evident from the sudden change of features in the fracture surface shown in Figure 66b.

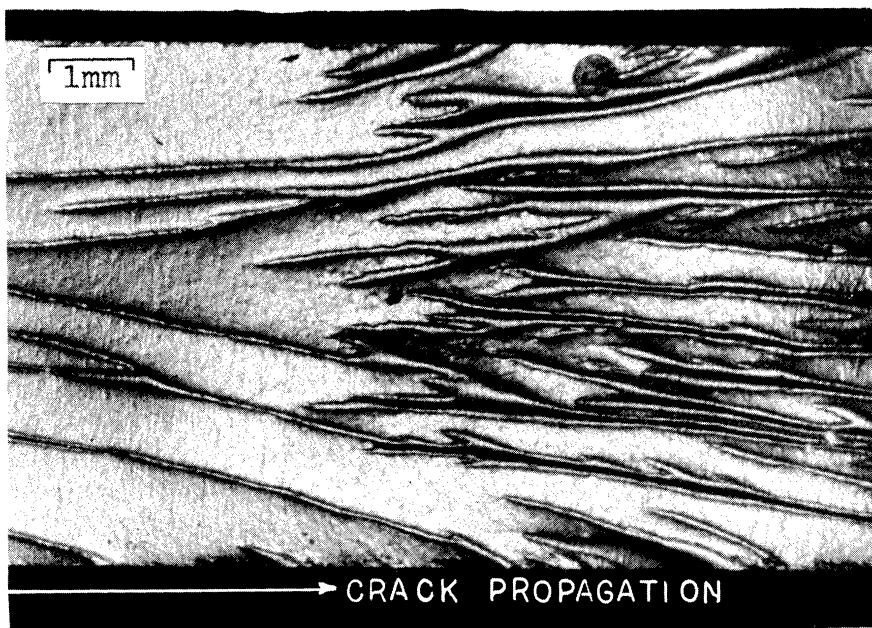
The fracture markings from the stable crack growth also seem to show the involvement of voids. Voids in the



$\dot{a} \approx 1 \text{ mm/s}$ $\dot{a} \approx 100 \text{ } \mu\text{m/s}$ $\dot{a} \approx 10 \text{ } \mu\text{m/s}$
Figure 65. Fracture surfaces from stable cracking at 296 °K for PMMA



(a)



(b)

Figure 66. Abrupt change in PMMA fracture surface associated with the sudden change in fracture toughness at a) 243°K and b) 353°K

craze material coalesce as a function of the fracture toughness (Cotterell 1968, Lednicky and Pelzbauer 1972). In the low crack speed region, the associated fracture toughness has such a low value that only a few cavities are formed and they show up as dimple marks on the fracture surfaces (Figure 57). As the crack speed increases, the associated fracture toughness also increases and more voids will coalesce, making needle-like features. Further increase in crack speed, with an increase in fracture toughness, promotes more coalescence of voids, thereby changing the needle-like features into coarser, rib-like markings. These coarse rib markings suddenly change to a flat, featureless surface as the fracture mode changes from stable to unstable propagation.

The observation of fracture surface provides some qualitative explanations regarding the fracture processes in PMMA. The fracture surfaces of stable fracture do not show any conic markings that are present in unstable fracture surfaces. Since the formation of conic markings are the consequence of secondary crack propagation ahead of crack front, the above distinction indicates that the unstable fracture is associated with the onset of secondary crack propagation in front of the main crack front. And this onset of secondary crack propagation seems to start only when the fracture toughness value has exceeded a threshold level; the fracture toughness value at the onset of unstable crack propagation was $\sim 600 \text{ J/m}^2$ for most of the temperatures involved in the present study (see section IV.4.1.1).

An incidental observation of various fracture patterns, made by a film of petroleum jelly sandwiched between two transparent PMMA plates, deserves a comment at this point. When this sandwiched film was broken by parting the two PMMA plates slowly, it showed patterns very similar to the needle-like markings on the fracture surface of a PMMA specimen associated with stable crack propagation. However, if the PMMA plates were separated by impact loading, they showed features like the densely populated conic markings, such as those observed on the PMMA fracture surfaces associated with unstable fracture at a high stress intensity factor. Similar observations were made by Hays and Feiten (1964) who showed evolution of cavity formation in a thin viscous film between two parallel plates as the two plates are separated at high velocity. Their high speed camera shows that at the early stage only a few cavities form and they grow in a "fern-like" shape, which is similar to the "needle-like" feature on the PMMA fracture surfaces. As the separation of the two plates proceeds at high speed, more cavities are formed and they grow to meet each other, forming features similar to the conic markings on the fast, unstable fracture surfaces of PMMA. Since the craze material ahead of a crack tip may be considered as a viscous film with high viscosity, these incidental observations pose a possibility of using such a viscous film in making a model involved with the fracture process of glassy polymers. This subject is left for a future study.

V.2 PC

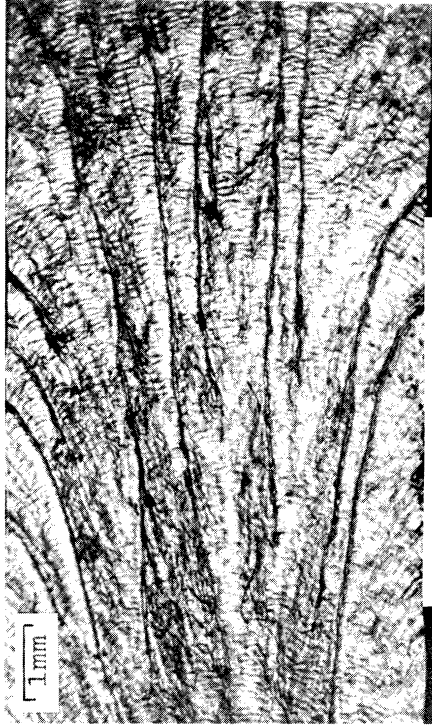
The fracture surfaces of PC for stable crack propagation are shown in Figure 67. They are the regions where the crack passed at about the same crack speed (2.5 mm/s) at different temperatures. The arrow indicates the crack propagation direction. The dark regions on both sides of each fracture surface are the shear-lips formed by plastic flow. The extent of this shear lip is suppressed with decreasing temperature and the fracture surface at 213 °K shows practically no shear lips and as the temperature increases the shear lip size increases. The size of shear lips does not increase significantly between 213 °K to 273 °K. However, when the temperature increased from 273 °K to 296 °K, plastic flow occurred throughout the whole section of the thickness, as shown in Figure 68a. The thumbnail mark at the initial region corresponds to the pop-in mark on a load-displacement curve. Gurney's method of finding fracture toughness, R , by means of sector area in load displacement is not applicable any more. This dramatic change in plastic shear-lip size between the temperature 273 °K and 296 °K correlates with the sharp drop in fracture toughness in the same temperature region (see Figure 50).

Conic markings are also visible on the unstable fracture surface of PC. Figure 68b shows such conic marking on the unstable fracture surface of PC sheet.

Crack propagation direction for all pictures



(a) $T = 273 \text{ }^\circ\text{K}$



(c) $T = 233 \text{ }^\circ\text{K}$

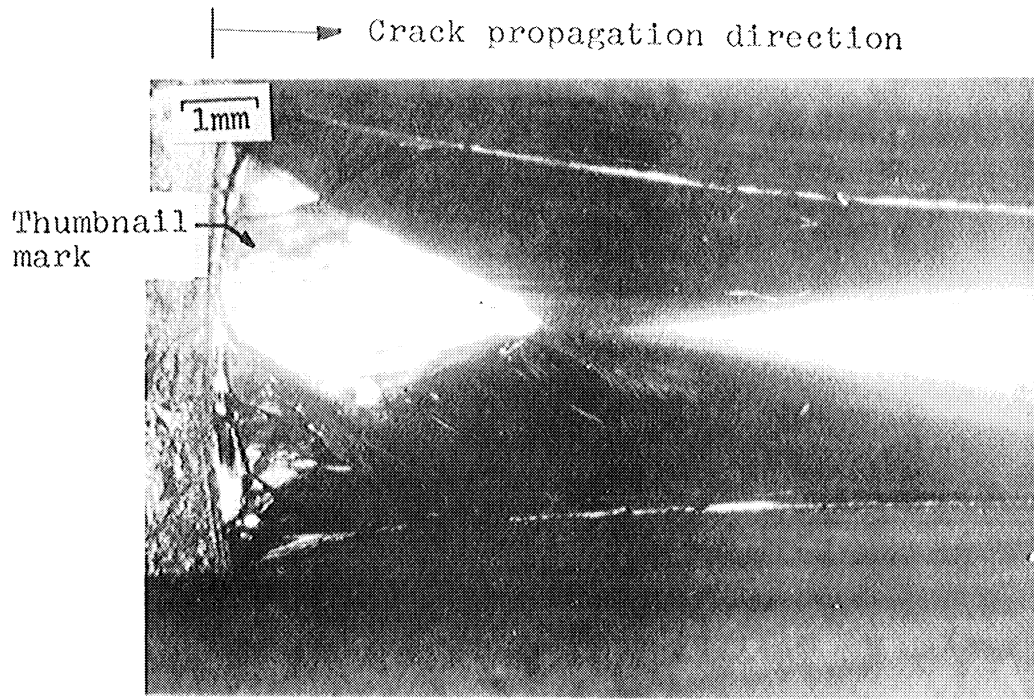


(b) $T = 253 \text{ }^\circ\text{K}$

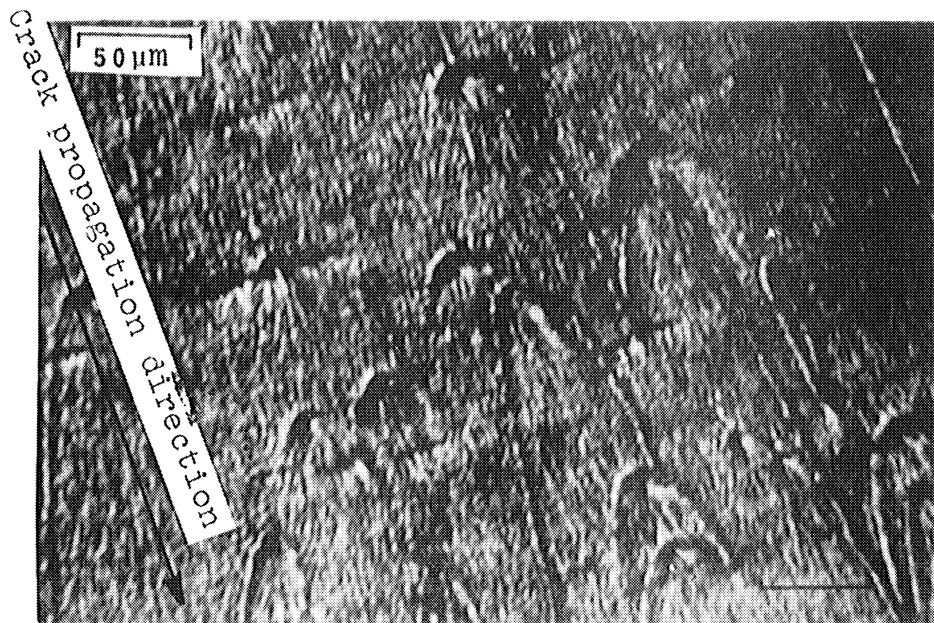


(d) $T = 213 \text{ }^\circ\text{K}$

Figure 67. Fracture surfaces of PC obtained from stable cracking at various temperatures



(a) Stable cracking at 296 °K



(b) Unstable cracking at 296 °K

Figure 68. Stable cracking (a) and unstable (b) of PC at 296 °K

CHAPTER VI

CONCLUSIONS AND RECOMMENDATION FOR FUTHER STUDY

VI.1 Conclusions

1. The relationship $a=A_1 \exp\left(\frac{\bar{U}-\lambda R}{kT}\right)$, given in equation (4.8) provided an excellent fit of the fracture toughness (R) data of PMMA obtained from stable crack propagation experiments in the temperature region 283 °K to 353 °K. The activation energy obtained from the curve fit of the data came close to that of β -relaxation process of this material. If the β process provides the necessary molecular motion for craze formation (Boyer 1968), stable crack growth in this temperature range may be viewed as a continuous formation of craze material at the leading edge of the crack tip and breaking of this crazed material at the trailing edge of the crack tip. The rate involved during this process is determined by the fracture toughness, R, and temperature according to the relationship given in equation(4.8).

However, the fact that equation(4.8) is not applicable in the temperature region below 283 °K, suggests that the β mechanism may be suppressed in this temperature region. K_{IC} vs. temperature curves also show signs of a transition as the temperature is decreased below 283 °K. Some stable cracking was achieved at low crosshead speeds below 283 °K, but at temperatures below 243 °K no stable crack propagation was achieved even at the slowest crosshead speed (0.833 $\mu\text{m/s}$)

These changes in fracture behavior of PMMA lead one to

suspect that a different molecular mechanism is involved in the fracture process in the two temperature ranges, i.e. above 283 °K and below 283 °K.

2. The variation of fracture toughness, R , of PC is related with the size of the plastic shear lips on both sides of the crack front. Increase in crack speed reduces the size of the plastic shear lips and thus decreases the fracture toughness. However, a small but noticeable increase in fracture toughness is observed with increasing crack speed at temperatures below 213 °K. At such low temperatures, the crack tip plastic zone is almost eliminated, thus allowing the determination of 'valid' fracture data. In particular, equation (4.8) could be applied to the results obtained below 213 °K. Thus, the fracture toughness of PC is dependent more on the plastic flow on both sides of the crack tip than on craze formation and subsequent rupture of the crazed layer as was the case with PMMA. The dependence of fracture toughness of PC on the crack speed was less pronounced compared to the effect of temperature. Nearly a ten fold decrease in fracture toughness of PC occurred as the temperature decreased from 296 °K to 273 °K. Similar transitions in K_{IC} results occurred at 263 °K for the crosshead speed of 83.3 $\mu\text{m/s}$ and 273 °K for the crosshead speed of 8.33 mm/s.

3. The equivalent strain rate expression in equation (4.16) can be used in determining the equivalent rate dependent Young's modulus of a fracture specimen with a stationary crack. This technique was successfully used in the

K-calibration procedure of the rate dependent material, PMMA.

4. The equivalent Young's modulus of a fracture specimen with a moving crack can be estimated by using the relationship $E=K^2/R$, where K and R are obtained experimentally at the same crack speed. The equivalent modulus values based on the strain rate at the moving crack tip (Williams 1972) were substantially higher than the present results.

5. Various features on the stable fracture surfaces of PMMA can be characterized by the crack speeds and test temperatures, while the features on unstable fracture surfaces are characterized by the K_{IC} level.

VI.2 Recommendations for Future Study

1. Further study on the fracture behavior of PMMA at temperatures below 283 °K is recommended on two accounts:

a) The stable crack growth becomes limited at the temperatures below 283 °K and no stable crack growth was achievable below 233 °K.

b) Variation of fracture toughness in this temperature region did not follow the same family of curves as predicted by equation (4.8).

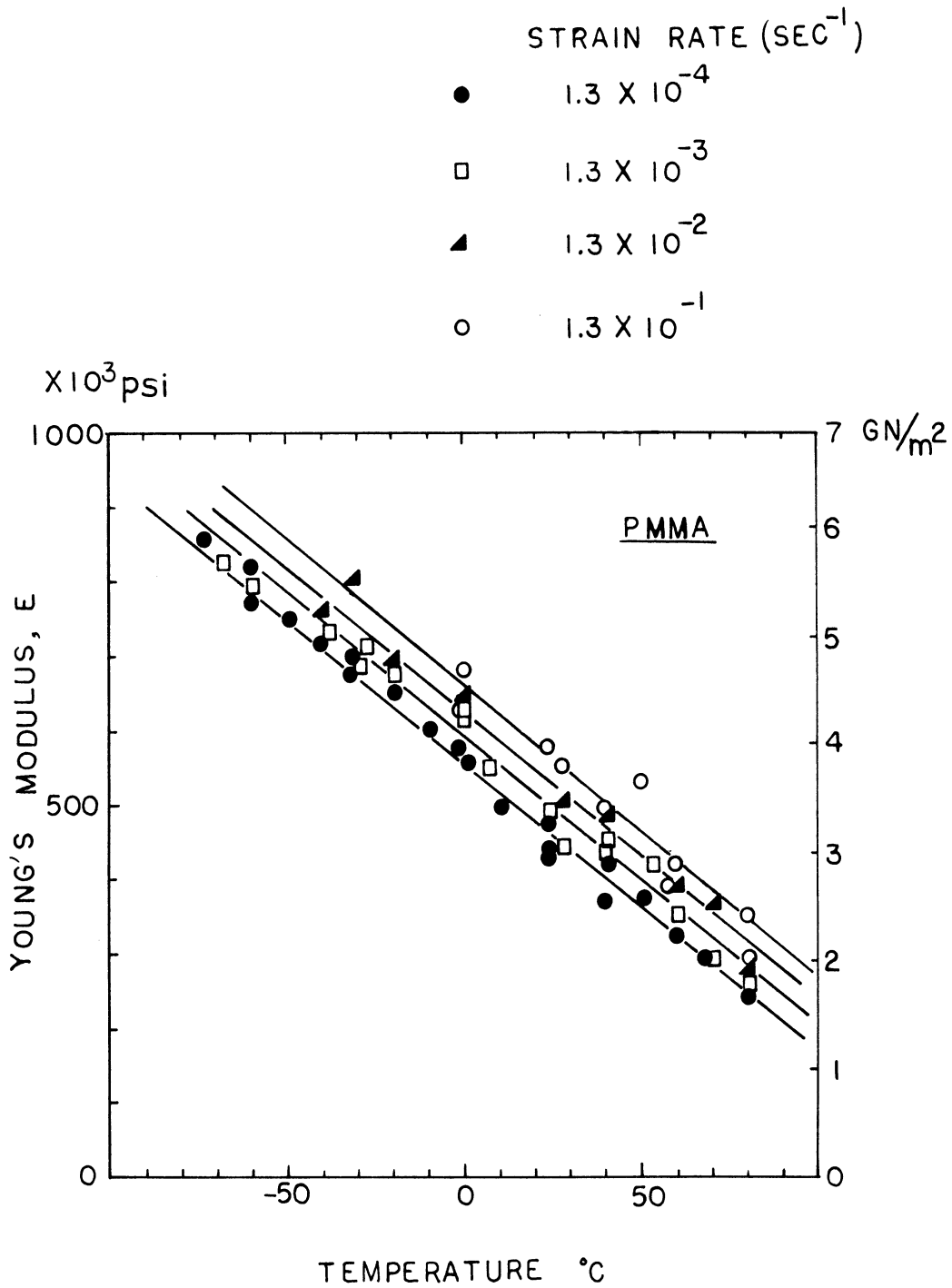
Stability of crack growth in this temperature region can be studied further by applying the stability parameter reported by Gurney and Mai (1972).

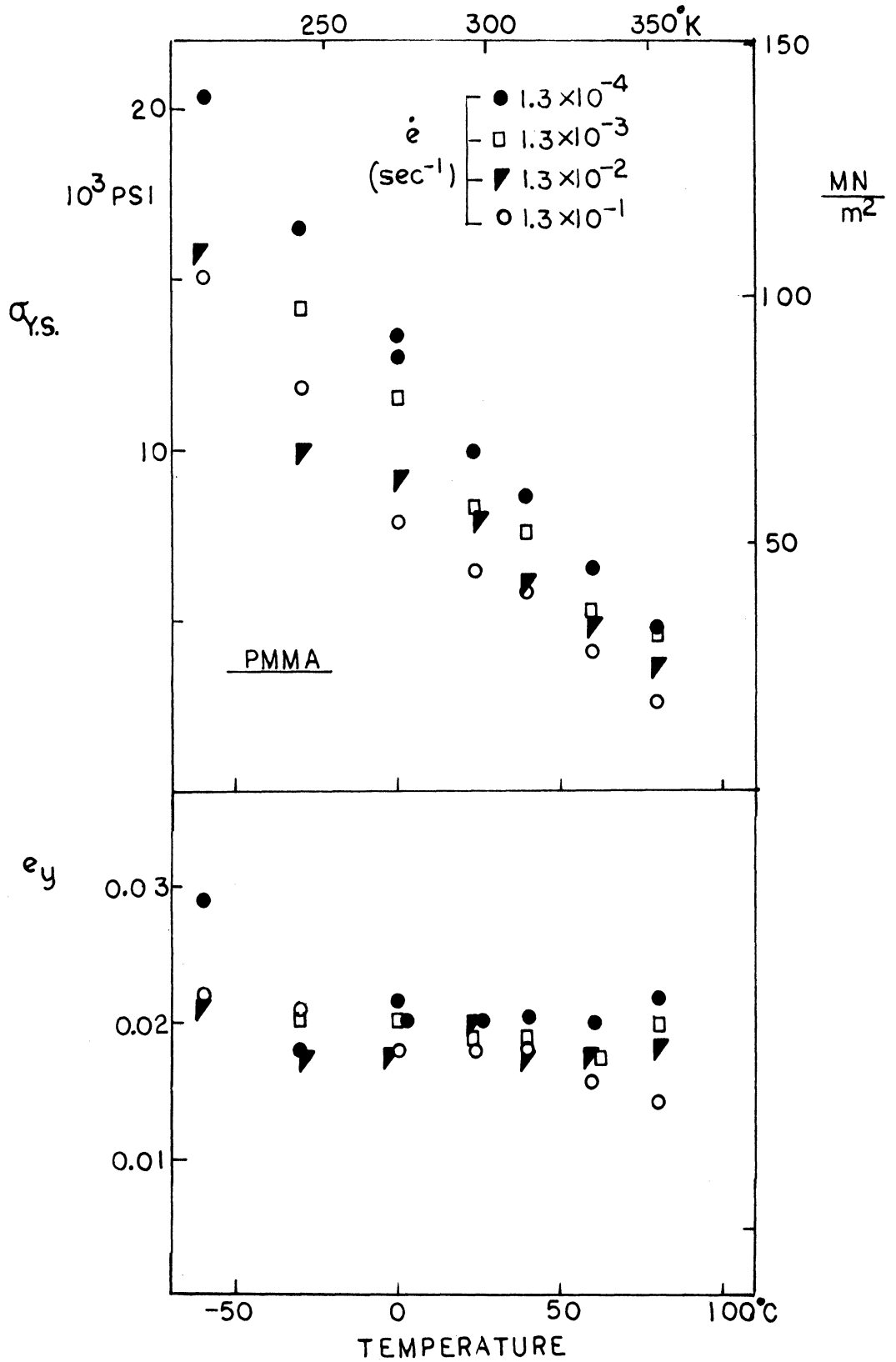
2. Fracture surfaces of unstable fracture showed parabolic and hyperbolic markings; these are absent in the fracture surfaces of stable fracture. Since these markings are associated with the secondary fracture fronts growing independently at the speed comparable to or larger than the primary crack speed ($n \geq 1$), unstable fracture may be studied in terms of kinetics involved with nucleation and growth of voids.

A microscopic and macroscopic study of the rupturing process of a thin film of varying viscosity sandwiched between two transparent rigid plates may provide a means of making models for void formation and growth in the craze material at the crack tip.

APPENDIX I

TEMPERATURE AND STRAIN RATE DEPENDENT
TENSILE PROPERTIES OF PMMA





APPENDIX II

DERIVATION OF THE STRAIN RATE
EXPRESSION GIVEN IN EQUATION (4.11)

The expression for strain near the crack tip is given by equation (4.10) as,

$$e = \frac{K(t)}{E(t)} \cdot (2\pi r)^{-\frac{1}{2}} \quad (4.10)$$

By differentiation equation (4.10) with respect to time,

$$\dot{e} = \frac{\dot{K}E - E\dot{K}}{E^2} (2\pi r)^{-\frac{1}{2}} - \frac{K}{2E} (2\pi r)^{-\frac{3}{2}} (2\pi \dot{r}) \quad (A.2.1)$$

where dot symbols are used to represent the differentiation with respect to time. The rate of change of distance from a fixed point ahead of a crack tip is the same as the crack speed, with opposite sign, i.e. $\dot{r} = -\dot{a}$. Thus substituting \dot{r} by $-\dot{a}$,

$$\dot{e} = \frac{\dot{K}E - E\dot{K}}{E^2} (2\pi r)^{-\frac{1}{2}} + \frac{K}{2E} (2\pi r)^{-\frac{3}{2}} (2\pi \dot{a}) \quad (A.2.2)$$

From equation (4.10), $(2\pi r)^{-\frac{1}{2}} = \frac{eE}{K}$. Substituting $\frac{eE}{K}$ for $(2\pi r)^{-\frac{1}{2}}$ in equation (A.2.2),

$$\dot{e} = \left(\frac{\dot{K}}{E} - \frac{E\dot{K}}{E^2} \right) \frac{eE}{K} + \frac{K}{2E} \frac{e^3 E^3}{K^3} (2\pi \dot{a}) \quad (A.2.3)$$

Rearranging the above equation, we get the result in equation (4.11).

$$\dot{e} = \left(\frac{\dot{K}}{K} - \frac{\dot{E}}{E} \right) \cdot e + \pi e^3 \left(\frac{E}{K} \right)^2 \dot{a} \quad (4.11)$$

APPENDIX III
FORMATION OF CONIC MARKINGS

The location of the primary crack at time t is (see figure 57),

$$x = Vt \quad (A.1)$$

and the secondary crack makes a circle of radius ut , with its center located at $P (x=x_0, y=0)$,

$$(x - x_0)^2 + y^2 = (ut)^2 \quad (A.2)$$

The equation of the locus of the intersection of two crack fronts can be found from equation (A.1) and (A.2) as described in the following derivations.

From equation (A.1),

$$t = x/V \quad (A.3)$$

Introducing equation (A.3) into equation (A.2),

$$(x - x_0)^2 + y^2 = (u/V)^2 x^2 \quad (A.4)$$

Equation (A.4) can be rewritten by introducing the crack speed ratio, n , which represents the ratio of the crack speeds of the secondary crack and the primary crack, i.e.

$$n = v/V,$$

$$(x - x_0)^2 + y^2 = n^2 x^2 \quad (A.5)$$

Depending on the magnitude of the crack speed ratio, n , equation (A.5) will describe a parabola, ellipse or hyperbola. Individual cases are discussed in the following derivations and they are plotted in Figures A.3.1 through A.3.3.

1) $n=1$: Parabola

If $n=1$, equation (A.5) reduces to

$$(x - x_0)^2 + y^2 = x^2$$

$$x^2 - 2x_0x + x_0^2 + y^2 = x^2$$

$$x = \frac{1}{2x_0} y^2 + \frac{x_0}{2} \quad (A.6)$$

2) $n < 1$: Ellipse

Equation (A.5) can be rearranged to a more familiar form of the equation of an ellipse as follows;

$$(x - x_0)^2 + y^2 = n^2 x^2$$

$$x^2 - 2xx_0 + x_0^2 + y^2 = n^2 x^2$$

$$x^2(1-n^2) - 2xx_0 + x_0^2 + y^2 = 0$$

$$(1-n^2) \left[x^2 - \frac{2xx_0}{(1-n^2)} + \left(\frac{x_0}{1-n^2} \right)^2 - \left(\frac{x_0}{1-n^2} \right)^2 \right] + x^2 + y^2 = 0$$

$$(1-n^2)\left(x - \frac{x_0}{1-n^2}\right)^2 + y^2 = \frac{x_0^2}{1-n^2} - x_0^2 = \frac{n^2}{1-n^2} x_0^2$$

Dividing both sides by $\frac{n^2}{1-n^2} x_0^2$,

$$\frac{\left(x - \frac{x_0}{1-n^2}\right)^2}{\frac{n^2}{(1-n^2)^2} x_0^2} + \frac{y^2}{\frac{n^2}{(1-n^2)^2} x_0^2} = 1$$

$$\frac{\left(x - \frac{x_0}{1-n^2}\right)^2}{\left(\frac{nx_0}{1-n}\right)^2} + \frac{y^2}{\left(\frac{nx_0}{\sqrt{1-n^2}}\right)^2} = 1 \quad (\text{A.7})$$

Equation (A.7) is an expression of an ellipse with major axis length of $\frac{nx_0}{1-n^2}$ and minor axis length of $\frac{nx}{\sqrt{1-n^2}}$, and the center of ellipse is located at $x = \frac{x_0}{1-n^2}$, $y=0$.

3) $n > 1$: Hyperbola

Following the same procedure as used in (2) above, equation (A.5) can be rearranged, as follows,

$$(x - x_0)^2 + y^2 = n^2 x^2$$

$$x^2 - 2x_0 x + x_0^2 + y^2 = n^2 x^2$$

$$x^2(n^2-1) + 2xx_0 - x_0^2 - y^2 = 0$$

$$(n^2-1)\left[x^2 + \frac{2xx_0}{n^2-1} + \left(\frac{x_0}{n^2-1}\right)^2 - \left(\frac{x_0}{n^2-1}\right)^2\right] - x_0^2 - y^2 = 0$$

$$(n^2-1)\left(x + \frac{x_0}{n^2-1}\right)^2 - y^2 = \frac{n^2}{n^2-1} x_0^2$$

Dividing both side by $\left(\frac{n^2}{n^2-1} x_0^2\right)$,

$$\frac{\left(x + \frac{x_0}{n^2-1}\right)^2}{\left(\frac{nx_0}{n^2-1}\right)^2} - \frac{y^2}{\left(\frac{nx_0}{\sqrt{n^2-1}}\right)^2} = 1 \quad (\text{A.8})$$

Equation (A.8) is the equation of an hyperbola.

The following figures illustrate various conic markings.

1) $n = 1$: PARABOLA

$$x = \frac{1}{2x_0} y^2 + \frac{x_0}{2}$$

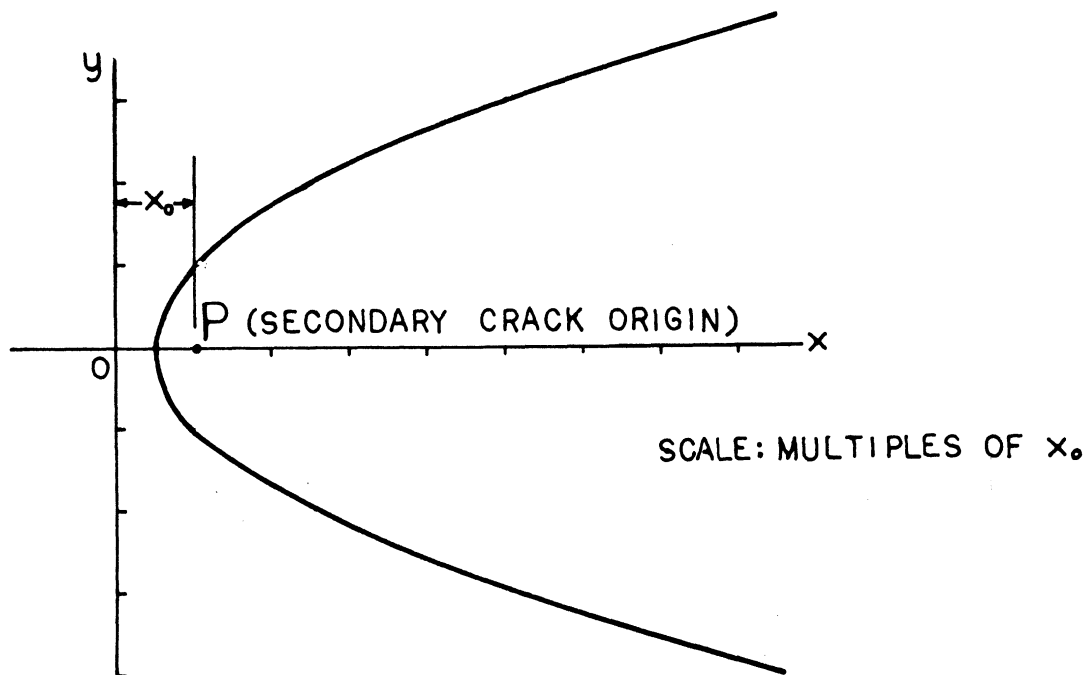
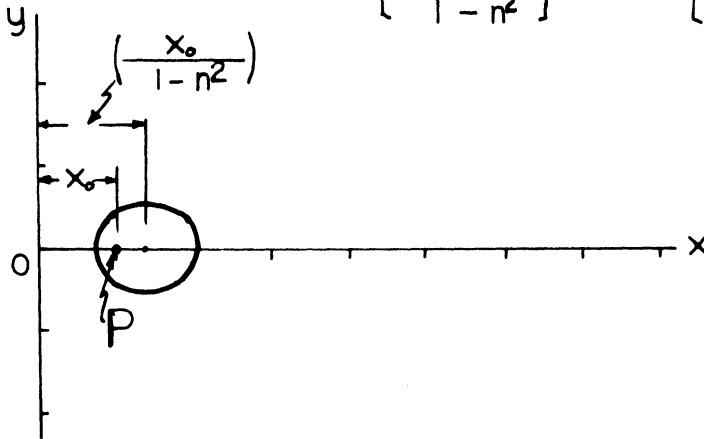


Figure A.3.1 Formation of a parabolic marking when $n=1$

2) $n < 1$: ELLIPSE †

$$\frac{\left[x - \frac{x_0}{1-n^2} \right]^2}{\left[\frac{n x_0}{1-n^2} \right]^2} + \frac{y^2}{\left[\frac{n x}{\sqrt{1-n^2}} \right]^2} = 1$$

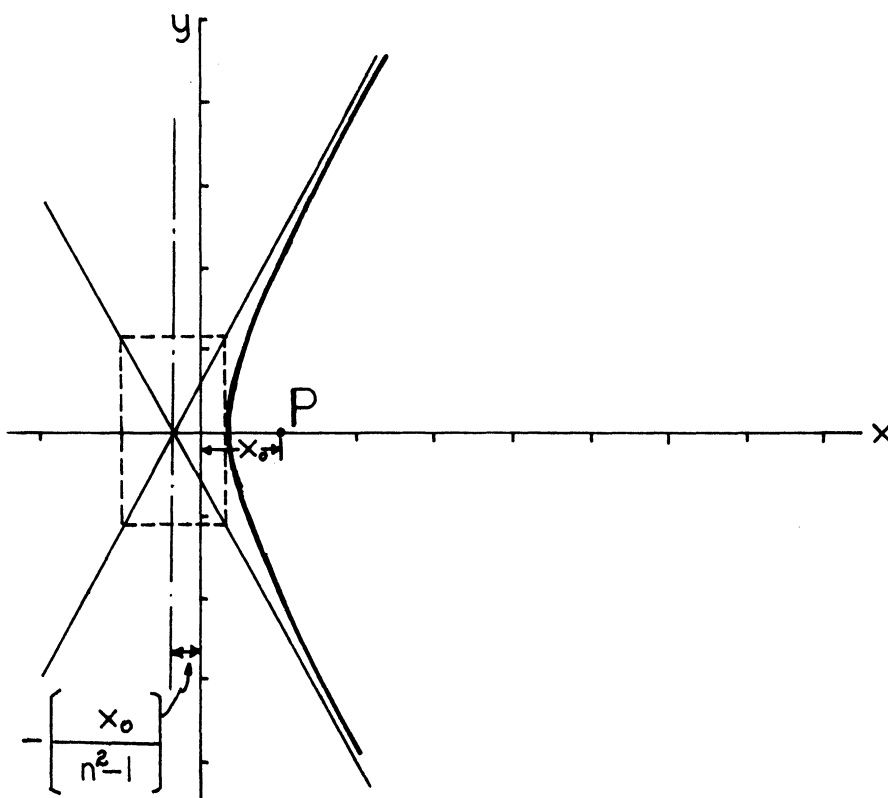


† DRAWING BASED ON $n=0.5$

Figure A.3.2 Formation of an elliptical marking when $n < 1$

3) $n > 1$: HYPERBOLA*

$$\frac{\left[x + \frac{x_0}{n^2-1} \right]^2}{\left[\frac{nx_0}{n^2-1} \right]^2} - \frac{y^2}{\left[\frac{nx_0}{\sqrt{n^2-1}} \right]^2} = 1$$



* DRAWING BASED ON $n=2$

Figure A.3.3 Formation of a hyperbolic marking when $n > 1$

REFERENCES

1. Andrews, E. H.(1968). 'Fracture in Polymer' American Elsevier, N.Y.
2. Atkins, A. G. and Caddell, R. M.(1973). To be published.
3. Beahan, P., Bevis, M. and Hull, D.(1971). Phil. Mag., 24, 1267.
4. Benbow, J. J. and Roesler, F. C.(1957). Proc. Phys. Soc. (London), B70, 201.
5. Benbow, J. J.(1961). Proc. Phys. Soc. (London), 78, 970.
6. Berry, J. P.(1961). J. Polymer Sci., 50, 107.
7. Berry, J. P.(1963a). J. Polymer Sci., A1, 993.
8. Berry, J. P.(1963b). J. Appl. Phys., 34(1), 62.
9. v.d. Boogart, A. and Turner, C. C.(1963). Trans. J. Plastic Inst., 31, 109.
10. Boyer, R. F.(1968). Polymer Eng. and Sci., 8(3), 161.
11. Broutman, L. J. and McGarry, F. J.(1965). J. Appl. Polymer Sci., 9, 589.
12. Broutman, L. J. and Kobayashi, T.(1971). AMMRC CR 71-14, Army Mater. Mech. Res. Ctr., Watertown, Mass.
13. Broutman, L. J.(1973). Private Communication.
14. Brown, W. F., Jr. and Srawley, J. E.(1966). ASTM STP No. 410.
15. Cotterell, B.(1965). J. Mater. Res., 4(4), 227.
16. Cotterell, B.(1968). Int. J. Fracture Mech., 4(3), 209.
17. Cotterell, B.(1970). Int. J. Fract. Mech. 6, 139.
18. Gent, A. N.(1970). J. Mater. Sci., 5, 925.
19. Griffith, A. A.(1921). Phil. Trans. Roy. Soc. (London), A221, 163.
20. Griffith, A. A.(1924). Proc. of the 1st Int. Congress on Appl. Mech. (Delft) , 55.

21. Gurney, C. and Hunt, J.(1967). Proc. Roy. Soc. (London), A229, 508.
22. Gurney, C. and Mai, Y. W.(1972). Eng. Fract. Mec. 4, 853.
23. Hardy, M. P. and Hudson, J. A.(1973). 'Closed Loop' Spring, 9, MTS Systems Corp.
24. Hays, D. F. and Feiten, J. B.(1964). In "Cavitation in real liquid", Davis, R. ed., 1964. Elsevier Co., N.Y.
25. Heijboer, J.(1968). J. Polymer Sci., C16, 3755.
26. Higuchi, M.(1966). Proc. First Int. Conf. Fracture, Sendai, Japan, 2, 1211.
27. Hull, D. and Owen, T. W.(1973). J. Polymer Sci. 11, 2039.
28. Inglis, C. E.(1913). Trans. Inst. Naval Architects (London), 55, 219.
29. Irwin, G. R.(1957). J. Appl. Mech. 24, 361.
30. Irwin, G. R.(1958). Fracture, Handbuch der Physik, Vol.6, S. Flugge ed., Springer-Verlag, p551.
31. Irwin, G. R.(1963). ASME Paper 63-WA-217.
32. Irwin, G. R.(1965). Quoted from Panel discussion in "Fracture Toughness testing", ASTM STP No. 381, 199.
33. Johnson, F. A., Radon, J. C.(1972). Eng. Mech., 4, 455.
34. Kambour, R. P.(1966). J. Polymer Sci., A2, 4, 349.
35. Kambour, R. P. and Holik, A. A. (1969a). Polymer Preprints, Am. Chem. Soc., Div. Polymer Chem., 10(2), 1182.
36. Kambour, R. P. and Holik, A. S.(1969b). J. Polymer Sci., A2, 7, 1393.
37. Kambour, R. P.(1970). Quoted from p69 in G. E. Report No. 70-C-104.
38. Kambour, R. P. and Russell, R. R.(1971). Polymer, 12, 237.
39. Kambour, R. P.(1972). G. E. Report No. 72 CRD 285, Oct. 1972, G. E. Schnectacy, N.Y.
40. Key, P. L., Katz, Y. and Parker, E. R.(1968). UCRL Report No. 17911, Berkeley, Calif.

41. Kuvshinskii, E. V. and Lebedev, G. A.(1962). Soviet Phys. and Solid State, 3, 1947.
42. Lednicky, F. and Pelzbauer, Z.(1972). J. Polymer Sci. C 38, 375.
43. Mai, Y. W.(1973). Int. J. Fracture, 9, 349.
44. Manjoine, J. C.(1965). J. Basic Eng., Trans. ASME, D87(2), 269.
45. Marshall, G. P., Culver, L. P. and Williams, J. G.(1969). Plastic and Polymers, 37(127), 75.
46. Marshall, G. P., Culver, L. E. and Williams, J. G.(1970). Proc. Roy. Soc. (London), A319, 165.
47. Marshall, G. P. and Williams, J. G.(1973). J. Appl. Polymer Sci., 17, 987.
48. Maxwell, B. and Rahm, L. F.(1949). Industrial Eng. Chem., 41, 1988.
49. Newman, J. C., Jr.(1973). Personal communication.
50. Orowan, E.(1950). Proc. Symp. on Fatigue and Fracture of Metals., 139, Wiley, N.Y.
51. Paris, P. C. and Sih, G. C.(1965). ASTM STP, No. 381, 30.
52. Rabinowitz, S. and Beardmore, P.(1972). CRC Crit. Reviews in Macromol. Sci. Jan. 1972, Chem. Rubber Co. Press, Clev. Ohio.
53. Radon, J. C.(1971). Material Prufung., 13(8), 253.
54. Radon, J. C.(1972). Polymer Eng. Sci., 12, 425.
55. Ree, T. and Eyring, H.(1957). J. Appl. Phys., 26, 985.
56. Regel, V. R.(1956). J. Tech. Phys. (USSR), 26, 359.
57. Ripling, E. J., Mostovoy, S. and Crosley, P. B.(1967). J. Mater., 2(3), 661.
58. Sauer, J. A., Marin, J. and Hsiao, L. C.(1949). J. Appl. Phys. 20, 507.
59. Sauer, J. A. and Hsiao, C. C.(1953). ASME Trans., 75, 895.
60. Sato, Y.(1966). Kobunshi Kagaku, 23, 69.
61. Shand, E. B.(1954). J. Am. Cer. Soc., 37(12), 563.

62. Smekal, A.(1950). Glastechn. Ber., 23(2), 57.
63. Spurr, O. K., Jr., and Niegisch, W. D.(1962). J. Appl. Polymer Sci., 6, 585.
64. Srawley, J. E. and Gross, B.(1966). NASA Report No. TN D-3295.
65. Srawley, J. E. and Gross, B.(1967). NASA Report No. TN D-3820.
66. Srawley, J. E. and Gross, B.(1972). Eng. Fract. Mech., 4, 587.
67. Srawley, J. E., Busby, R. T., Fisher, D. M. and Jones, M. H.(1973). A draft of a chapter for SAE Monograph "Experimental Techniques in Fracture Mechanics", ed. Kobayashi. Courtesy of W. F. Brown.
68. Sternstein, S. S. and Ongchin, L.(1969). Polymer Preprints., Am. Chem. Soc., Div. Polymer Chem., 10(2), 1117.
69. Svensson, N. L.(1961). Proc. Phys. Soc. (London), 77, 876.
70. Vincent, D. I. and Gotham, K. V.(1966). Nature, 210, 1254.
71. Wallner, H.(1939). Z. Physik, 114, 368.
72. Westergaard, H. M.(1939). J. Appl. Mech., 61, A49.
73. Williams, J. G., Radon, J. C. and Turner, C. E.(1968). Polymer Eng. and Sci., 8, 130.
74. Williams, J. G.(1972). Int. J. Fract. Mech. 8(4), 1972.
75. Zhurkov, S. N.(1965). Int. J. Fract. Mech. 1, 311.

UNIVERSITY OF MICHIGAN



3 9015 03466 5813